Development of a Detailed Finite Element Model of the BIPED and Verification of Fidelity in Two Cases of Blunt Impact

by

Robert J. Chauvet

A thesis submitted in partial fulfillment of the requirements for the degree of

Master of Science

Department of Mechanical Engineering
University of Alberta

Abstract

Physical surrogates of the human head are commonly used to model cranial impacts and assess head injuries. The Brain Injury Protection Evaluation Device (BIPED mk2) is a head form that contains a brain simulant, fluid layer, connective membranes, a skull, and a skin layer and can measure kinematics, intracranial pressures, and strains. Finite element (FE) models can play a significant role in the development of new head form digital design iterations that better mimic the biological response of the head during impact by allowing researchers to modify material properties and geometries without fully redesigning and manufacturing the head form. This requires digitizing precise geometry, developing accurate material models and implementing realistic boundary conditions within the model. This study aims to create a digital model of the BIPED, perform a comparison of the model using supplied experimental data for both node displacement and pressure, complete a sensitivity study that ascertains whether the location of experimentally instrumented locations affected model outputs, and determine the effectiveness of experimental pressure sensors at capturing the coup and contrecoup phenomenon.

The model was developed in ABAQUS based on Computer-Aided Design (CAD) geometry supplied by Defense Research and Development Canada (DRDC). Two different types of BIPED experimental test data were simulated with the developed finite element model: displacement tests and pressure tests. Pressure and displacement time series responses were compared to the experimental data using CORrelation and Analysis (CORA).

The CORA values for the pressure comparison indicate an excellent correlation (>0.7) at the front sensor, while the back sensor was not considered just below a good correlation (<0.5). CORA ratings for the x (anterior-posterior) and z (superior-inferior) displacements of the 18 nodes tested resulted in a 0.554 average value, indicating a good correlation to the experimental data (> 0.5).

Model simulations and helmeted experimental impacts were used to understand the sensitivity of the pressure sensor locations within the BIPED. Kinematics from helmeted drop tower experiments were input into the model to determine the sensitivity of the simulation output location. One element removed (approximately 5 mm) in the x (anterior-posterior), y (medial-lateral), and z (superior-inferior) directions were compared to the center element (sensor location). A directional bias was observed in the direction parallel to impact, with the average percent difference from the center element being 11.7%. Nodal percent differences were then compared for the displacement tests in the x and z directions. This resulted in a 14.6%, unbiased, percent difference. These large sensitivities indicate that pressure and displacements in a finite element model brain are highly dependant on location.

The helmeted impacts were used to determine the effectiveness of the pressure sensor locations at correctly identifying the coup and contrecoup pressures. This was done by extracting the pressure gradient along the line of impact and comparing the values that the sensor locations read. It was determined that the sensors successfully characterised the coup and contrecoup pressure for impacts along its line of action but failed to do so for off-line impacts.

Based upon CORA scores, this study demonstrates successful development of a digital twin FE model for the BIPED head surrogate and comparison against experimental pressure and nodal displacement data with both kinematic and force inputs. Additionally, this study underlines the importance of knowing the correct location of the physical sensors while choosing output locations in finite element simulations. Lastly, this thesis helps identify that the locations chosen for pressure sensors in physical surrogate models adequately represented the coup and contrecoup pressures.

Preface

This thesis is an original work by Robert Chauvet. The project was motivated by a collaboration between four organizations. Simon Ouellet at Defence Research and Development Canada provided details on the BIPED mk2 head form design and a partnership in funding with the NSERC Alliance grant, Jennifer Rovt and Oren Petel from Carleton University provided expertise and data from the BIPED displacement experiments, Aaron Bryce and Katherine Barrett from the University of Victoria provided data and expertise about the pressure experiments, and lastly Ashton Martin of the University of Alberta provided data and expertise on the experimental approach on the BIPED headform. This was all done under the supervision of Chris Dennison and Lindsey Westover of the University of Victoria and Alberta respectively. The research project did not require ethics approval from the University of Alberta. This work does not necessarily represent the opinions of Defense Research and Development Canada (DRDC) or Department of National Defense (DND).

This work has been presented at two conferences, referenced below:

> R. Chauvet, A. Martin, J. Rovt, O. Petel, L. Westover, S. Ouellet, and C. Dennison, "Output Location Sensitivity Analysis for Head Impact FEA Models in Pressure and Displacement Using the BIPED Headform," in *IRCOBI Europe Conference*, 2023.
>
> R. Chauvet, A. Martin L. Westover, S. Ouellet, and C. Dennison, "Brain Injury Prevention Evaluation Device Finite Element Simulation*,"* in *Alberta Biomedical Engineering Conference*, 2022.

This work includes two papers that will be published following the release of this thesis:

> The first is a summary of chapters 3-5, focusing on the novel techniques used to validate of the BIPED. The analysis and writing were done by myself, while Jennifer Rovt, and Ashton Martin provide the experimental data to run in the simulation. Oren Petel, Simon Ouellet, Lindsey Westover, and Chris Dennison provide supervision and guidance on the project.
>
> The second is a summary of chapter 6, focusing on the effect of sensor placement in pressure experiments. The experimental data collection, analysis, and writing were done by myself, while Aaron Brice and Katherine Barrett provide help with the experimental data collection that was to be run in the simulation. Simon Ouellet, Lindsey Westover, and Chris Dennison provide supervision and guidance on the project.

Acknowledgements

I am thankful for the endless guidance and support form my two supervisors, Dr. Lindsey Westover and Dr. Chris Dennison. They have both pushed me to uphold a standard of excellence in academia, while motivating me to start, and then continue on the path of research. A master's degree has a certain level of hecticity, that I was adeptly guided through by both of them.

I am also grateful for the support of both the labs at the University of Alberta and Victoria, the people made the work all the more enjoyable. A special thanks to the DRDC group, who originated the BIPED, the University of Victoria Lab for supplying the BIPED for experimentation, and Carleton University lab groups for the expertise that you gave. The contributions of all these groups made the project possible, thank you.

Contents

List of Tables

List of Figures

Chapter 1. Introduction

1.1 Motivation

Traumatic Brain Injuries (TBI) have a significant impact on an individual's health. These injuries can entail consequences that surpass physical damage and stray into cognitive and behavioural changes. [1] TBI can be caused by blunt impacts, blasts, or whiplash, and can cause changes to the normal brain function. In turn, this change in brain function decreases the individual's ability to live a full and normal life. TBI is a global issue. In Canada, TBI accounts for 9% of all hospitalizations, while the Center for Disease Control and Prevention found that in 2013 in the United States, TBI resulted in 2.8 million visits to the emergency room, hospitalizations, and deaths. [2] [3] This statistic does not account for all of the TBI that goes unreported, is not severe enough for a hospital stay, or is treated at other facilities. Some activities result in a higher rate of TBI, including sports, vehicle accidents and military settings. In these settings, all severities of TBI can benefit from personal protective equipment, such as helmets and seatbelts. Improving protection equipment can result in a lower rate of TBI in these higher risk activities. [4]

One way to improve helmet design, is to gain a more complete understanding of the physiological properties that induce a TBI. Helmet standards typically rely on assessing a helmet's ability to reduce impact severity as indicated by kinematic measures. This is done using a rigid head form, that only represents the shape and weight of a real head. [5] This approach does not capture the anatomical components of the head and the actual damage that may occur in the brain. It has been shown that injury metrics can be based upon stress and strain values inside of the brain, in addition to the rigid body kinematics of the head.[6] Assessing stress and strain can be done with cadaver tissue, but it poses a multitude of problems with respect to cost, availability, and repeatability. Anthropomorphic test devices (or surrogates) aim to solve these issues. [7] They represent the physical head and its anatomical structure with synthetic materials, standardized geometry, and precise manufacturing approaches.

One such head surrogate is the Brain Injury Protection Evaluation Device (BIPED mk2), developed by Defense Research and Development Canada (DRDC) to initially study blast wave propagation inside of the human head. [7] It has recently been used for the analysis of blunt impact injury, and further refinement of the head form has taken place.[8] It consists of a brain, a fluid layer, connective membranes, a skull, and skin, made out of synthetic materials. The full head model can be instrumented for various measurement scenarios. In all cases, the global head kinematics are measured with a six degree of freedom accelerometer attached to the base of the skull. For pressure tests, the instrumentation includes two Kulite pressure sensors (front and back of a sagittal slice) that are cast inside of the brain material. Strain studies are done with a BIPED instrumented with radio opaque markers on a parasagittal slice of brain 15 mm from center and tracked using a high-speed x-ray system. The overall goal is to better access injury mechanics using these instrumented heads in both pressure and strain. As the BIPED was originally developed and tested for blast scenarios, more research is needed to assess the bio-fidelity of this model in blunt impact scenarios. [8]

One method to improve the design process and gather more data is to create a digital twin of the BIPED head. A finite element model that can represent the physical model would provide valuable information to the designer. Potential design alterations would be easier to implement and test in the finite element model before being manufactured physically. This would speed up the design process and allow for parametric tests to be performed that could not occur experimentally. Another advantage of finite element models is the ability to get a complete view of stress and strain fields, as measurements in physical models are limited to instrumented sites.[9] These instruments are expensive and only give information at the specific implementation site. Finite element models can give full field of view analysis for impacts. This can help determine optimal locations for instrumentation in the physical models. [10] In the future, this model could also be used as a complementary piece to the physical model. Impacts could be simulated in-silico prior to lab experiments that involve intricate impact conditions.

The use of finite element models can be a key factor in improving physical head model designs. In order to utilize these simulated models, understanding of material properties, constraints, and boundary conditions must be accounted for. When this is achieved, the finite element model can be used to explore the sensitivity and placement of instrumentation sites.

1.2 Objectives

The objective of this research is to create a digital twin of the anthropomorphic BIPED head model. Once the finite element model is created, impacts will be simulated to evaluate the model performance in measuring both pressure and displacement of the brain in comparison to experimental impacts. The partially validated model will be used to investigate the effect of instrument location in the physical BIPED model. Afterwards, a sensitivity analysis will be done with finite element model simulations of a helmeted drop tower experiment. The specific objectives of the project are listed below:

1. Develop a finite element model of the BIPED head form from the manufacturing CAD models.
2. Compare the model in nodal displacement and pressure with the use of supplied experimental data.
3. Explore the impact of pressure sensor placement during impacts. This will include both a sensitivity analysis of the sensor location as well as characterizing the ideal sensor placement during a helmet testing certification.

1.3 Thesis Organization

This thesis is organized into chapters as follows:

Chapter 2 provides a brief overview of past work done in both the experiment and finite element studies of head injuries and describes the relevant literature to support the present work.

Chapter 3 describes the model development undertaken with the BIPED head form, including the material models, meshing, and assembly.

Chapter 4 provides the experimental setup, results and discussion from the pressure validation simulations run on the BIPED model.

Chapter 5 provides the experimental setup, results and discussion from the displacement validation simulations run on the BIPED model.

Chapter 6 describes the experimental design, setup, simulation, results and discussion for the sensor sensitivity analysis.

Chapter 7 provides the conclusions, limitations and suggested future work for the project.

Chapter 2. Literature Review

2.1 Head Injury

Head injuries are defined as injuries that occur in the skull, brain and other soft tissues in the vicinity of the head. When discussing the head, we can think of it being comprised of the outer skin layer (or scalp), skull, brain, and subarachnoid space and membranes. The subarachnoid space includes the fluidic cerebrospinal fluid (CSF) layer. A sample cross section of the head, with the main features, is shown in Figure 2-1. [11]

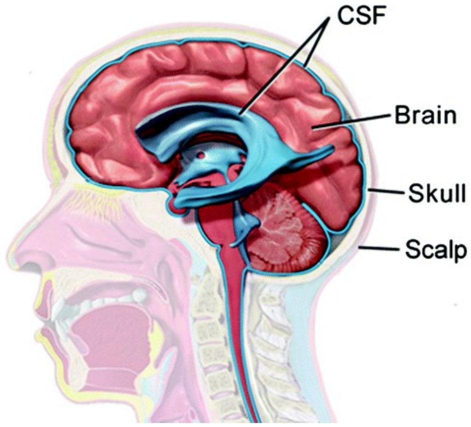

Figure 2-1 Cross Section of the Head [11]
Adapted with permission from Springer Nature

The specific head injuries discussed in this thesis refer to damage to the brain tissue. These injuries are referred to as traumatic brain injuries (TBI), which can be defined as an injury that affects the function of the brain. [12] While TBI can occur from numerous different scenarios, in general blast waves and rigid impacts are the two etiological mechanisms researched. Most impacts researched can be described as long duration impacts (greater than 5 ms). [13] Furthermore TBI can be broken down into two primary categories: focal and diffuse injuries. Focal injuries result from direct loading to the head in the form of an object striking the head or the head striking an object. The injury is confined to a specific location and causes localised damage. [14] Helmets and other protective gear aim to prevent focal injuries by increasing the area over which the impact occurs, and thus reducing the severity of the impact. The second injury type is a diffuse injury. These injuries affect a much larger portion of the head and are caused by changes in head kinematics. This can mean that diffuse injures do not need an impact to occur. Most of the diffuse injuries are caused by a swift head rotation, which causes shear forces to accumulate in the brain. Typically, diffuse injuries cause concussion-like symptoms and account for the majority of neurological disability, while focal injuries hold a 40% mortality rate. [15]

Estimating the type and severity of a head injury mechanically is difficult. The first attempt to characterise this was through the Wayne state head injury tolerance curve. [16] This metric used the linear accelerations of the head and the duration of the impact to determine the survivability of the impact. This curve (Figure 2-2, [16]) was developed using extensive animal and cadaver studies focusing on impacts causing skull fracture. Any combination of impact duration and acceleration above the curve would be classified as fatal. This chart is important, as it was the first attempt to classify head injury. What this curve fails to describe is if a head injury (but not fatal injury) happens if the impact is in the survivable zone of the curve.

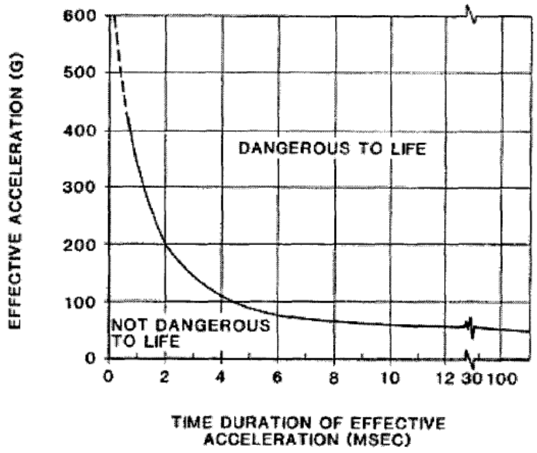

Figure 2-2 Wayne State Injury Tolerance Curve [16]

Adapted from U.S. Army Aeromedical Research Laboratory

Further refinements to the Wayne state head injury tolerance curve took place in the following years. Wayne state also pioneered a function to represent their data titled the HIC (Head Injury Criterion). [17] This metric assigns a score to the impact based on the accelerations and impact duration. Helmet manufacturers then used this metric to assess the protective qualities of their devices. A lower acceleration, longer duration impact (meaning a lower HIC score) occurring at the head would mean that the helmets helped reduce the effect of injury.

Over the years, other components have been added to these injury metrics, most importantly rotational velocity. This was included in the BRIC (Brain Rotational Injury Criterion), as it was found that rotational kinematics had a larger effect than linear accelerations on mild diffuse injuries. [18] Cadaver work to assess real brain metrics of stress and strain have also been reported. Most notably, pressures in the brain were experimentally determined by Nahum et al. [9] , and brain displacements by Hardy et al. [20] Intracranial pressures are in general proportional to trauma severity, while strain provides information on the severity of an injury that global kinematics cannot achieve. [5], [6] These two landmark studies are principal reports of the pressure and displacement response of actual cadaver brain tissue in head impact loading. As such, they are highly cited and commonly used references for all other head impact work using physical surrogate or computational models. This characterisation of the actual damage to the brain tissue instead of a global head kinematic was a very important step in understanding head injuries, especially ones causing mild TBI.

Finite element models have now continued this work by showing a more complete field of view of the brain during injury. It has also allowed new injury measures to evolve such as the maximum principle strain and the cumulative strain damage. [20] These metrics can be calculated in models and correlated to injury severity. This has led to more physical tissue parameters being present in helmet impact standards.

2.2 Head FE models

A large number of finite element head models have been developed in prior studies.[9], [20]–[23] The motivation for such models is that they give a full view of the head, unlike having experimentally instrumented cadavers, which only output measurement data at specific predetermined locations.[9] Also, cadavers are expensive, difficult to obtain, and if they can be procured, then they typically represent an aged adult population. Finite element models circumvent these issues but present a new array of challenges. Simulated models are only as good as the inputs provided. Part geometries, material models, meshing, constraints, and model inputs must provide a good representation of the physical system to produce meaningful results. In modelling, the goal is to represent the physical head as accurately as possible with the concession that approximations are necessary. As such, models have become more developed over the years, and slight improvements are made each time.

The benefits of finite element models are numerous. First, they provide the ability to characterise non-instrumented locations of the human head. [9] Instrumentation is localized in experimentally feasible locations, where sensors can be injected or cast into the brain or placed on the skull surface. Simulations can extract these same parameters at any location in the model. This allows for a greater understanding of the mechanics of biological tissue during impact. Models can also provide output parameters that cannot be feasibly implemented in the physical model. Examples of this include output parameters in small components such as the falx membrane, which are too thin to be instrumented properly. Secondly, the simulations can be used to work in-silico prior to experimentation. This allows researchers to efficiently gain an understanding of a specific impact mechanism, and its results prior to undergoing complex experimentation. Rough parameters for impact severity that are determined in the simulation can help shape the experimental testing protocols.

2.3 Model Validation

This section outlines the steps past head models have taken to compare their simulations against experimental data. The model that set the standard for validation technique was the GHMBC model. [21] Mao et al. compared against both a pressure experimental set as well as a nodal displacement data set with a highly detailed FE model. Previous to this, the SIMON model compared against this same data set, but with a much-simplified model aimed at fast computation. [20]. Now, simulated heads such as the YEAHM use the validation techniques developed by GHBMC. [22]

2.3.1 Boundary Conditions

Model inputs for head impact simulations are typically one of two things. The first being a kinematic input, where six degree of freedom acceleration values are input to a skull at center of mass location. The center of mass location is used since this is approximately the same location on every FE model after modellers scale the geometry to match the mass of the simulated head to the experimental head. This provides the movement of the head over time and accounts for rotation of the head and the influence of the neck in experimentally acquired data. The second approach to simulating a head impact is to use a kinetic input. This would involve selecting nodes on the skin layer and applying an impact force. An example set of data that could be input into a model to simulate a head impact is shown in Figure 2-3. The left one is from the Nahum et al. study and shows the applied force from the liner impactor measured with a force transducer during an experimental impact. [9] This time-series force could be used a kinetic input in an FE simulation of a head impact. Conversely, the right image in Figure 2-4 is from the Hardy et al. experiments and shows the linear accelerations and angular speeds measured. [19] These six degree of freedom time-series data curves could be used as kinematic input values in an FE simulation of head impacts. For force input boundary conditions, influence from the neck is not taken into account. This input is justified by citing sources saying that the rotational component the neck induces is very low and can be neglected in short duration impact events. A plot justifying this from the initial Nahum study is shown in Figure 2-4. [9]

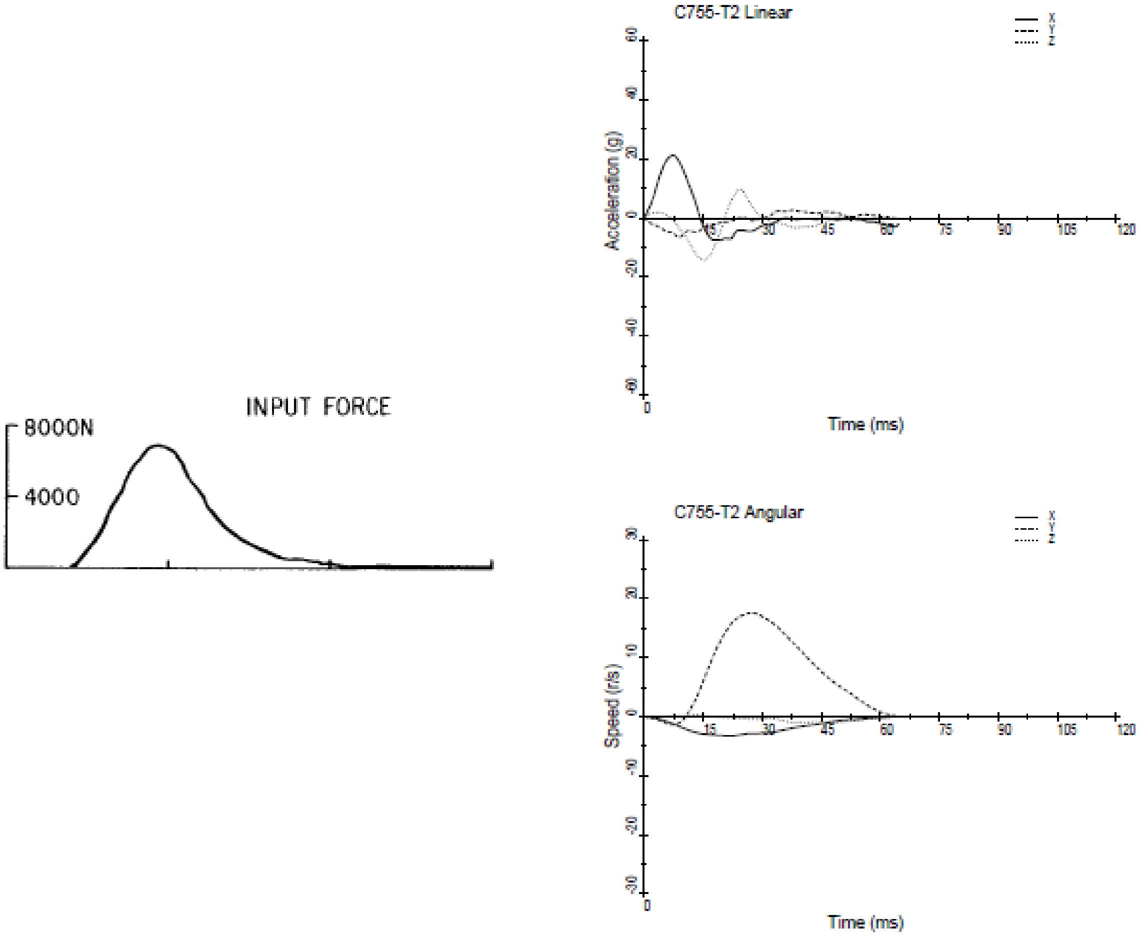

Kinetic (Force vs Time)[9]

Kinematic (Linear Acceleration/Rotational Velocity vs Time) [19]

Figure 2-3 Experimental Boundary Conditions

Adapted with permission from SAE International

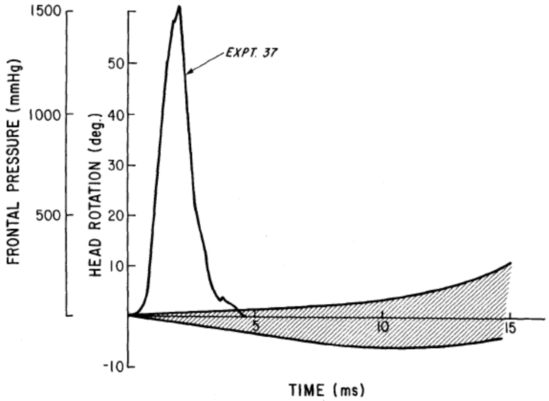

Fig. 2 - Head rotation related to the frontal pressure impact event

Black Line: Pressure Response Grey Area: Degrees of Head Rotation
Figure 2-4 Head Rotation and Pressure Plot [9]
Adapted with permission from SAE International

2.3.2 Pressure Validation

Increased pressure in neural tissue has long been associated with increased neural and capillary necrosis. [24] This is the reason that many head injury metrics rely on the hydrostatic pressure in the brain as one of their markers. For this reason, finite element models are often compared to cadaveric pressure experiments. [9], [20]–[23]

The first experimental dataset that is commonly used to validate FE head models the Nahum pressure data. [9] Nahum et al. used a seated cadaver with the head tilted at 45 degrees and generated impacts using a linear impactor. Pressure transducers were places in the intracranial space of the head at the frontal, parietal and occipital lobes. These transducers tracked pressure for the duration of the impact. A force transducer on the impactor also recorded the impact force, and an accelerometer mounted to the top of the skull measured the kinematics of the head.

Experiment 37 from Nahum et al. [9] shows the impact force, acceleration, and pressure time-series data during an a singular impact event (replicated in Figure 2-7). This data is commonly used to validate pressure output from FE models of similar head impacts. [9], [20]–[23] Key findings from Nahum et al. [9] demonstrated a positive peak (coup) in the frontal pressure and a contrecoup pressure at the rear. The contrecoup is a negative pressure at the rear occurring at the same time as the frontal positive peak. Pressure results can be seen in Figure 2-5. [9]

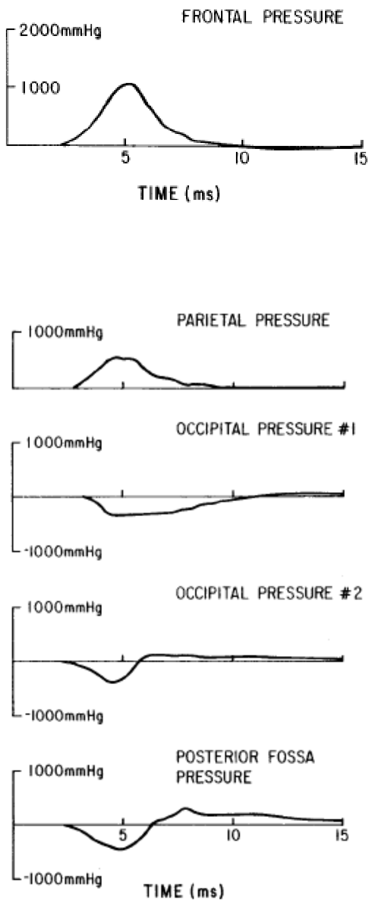

Figure 2-5 Nahum Experimental Results (Pressure vs Time) [9]

Adapted with permission from SAE International

In finite element validation studies, the goal is to match the phase, magnitude and shape of the pressure time histories. In many studies, the finite element models are in good agreement with the cadaver experiments as seen in Figure 2-6. [23]

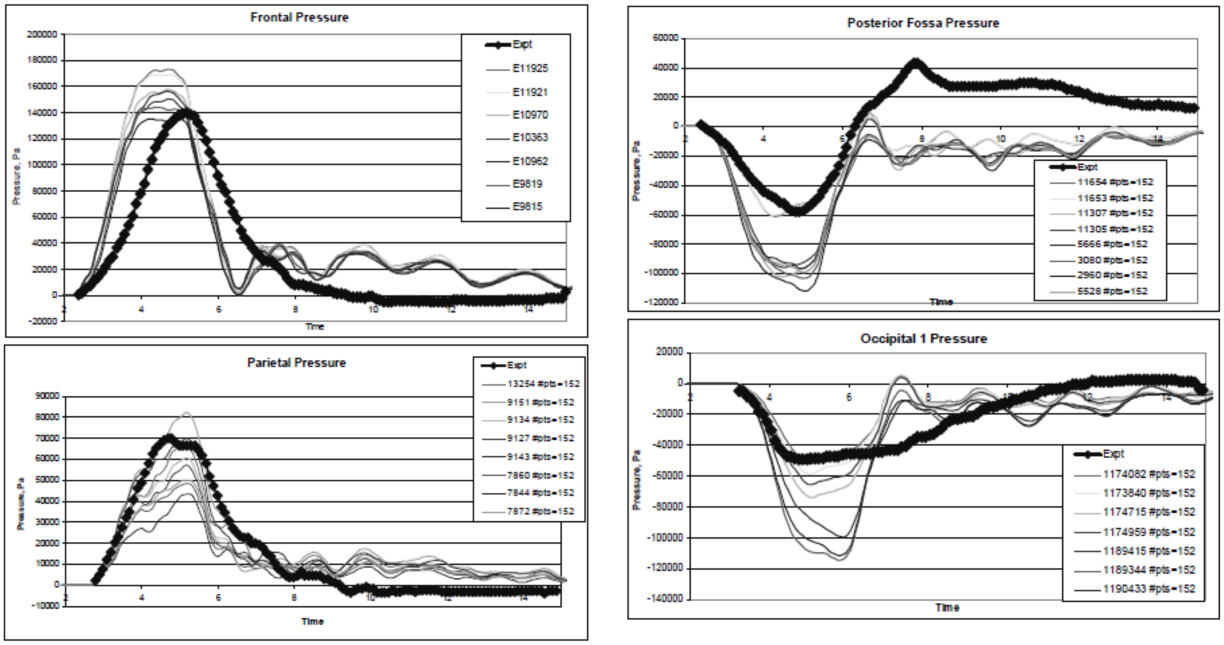

Grey: Model Prediction **Black**: Experimental Measurement

Figure 2-6 Comparison of FEA to Nahum Data [23]

A second cadaveric data set that can be used in validation is the Trosseille data. [25] It is typically used in conjunction with the Nahum set to obtain more data points in the pressure validation. The Trosseille data includes the full acceleration components as inputs that can be applied at the head center of mass. This gives modelers another option, in addition to the singular force or acceleration input from the Nahum data set.

2.3.3 *Displacement Validation*

Strain is associated with initial white matter injuries in the brain. [24] In order to measure strain, the displacements of brain tissue must be observed and recorded. Strain can be then extracted from the displacement data to analyze potential damage criteria for head injuries.

Displacement is used to validate the finite element models via the Hardy displacement studies.[19] Hardy et al. analyzed the displacement of Neural Density Targets (NDT) markers embedded in cadaver brain tissue along a parasagittal plane. Displacements were extracted using a high-speed x-ray system.

The displacements follow a rotation pattern in the head. On a frontal impact, this would entail a counter-clockwise rotation of the brain with respect to the skull. Results from the displacement are split into x (anterior- posterior) and z coordinate (superior-inferior) directions. In the displacement plots this results in sinusoidal like patterns in the x and z directions for each NDT marker. This is clear in the Hardy results shown in Figure 2-7. [19]

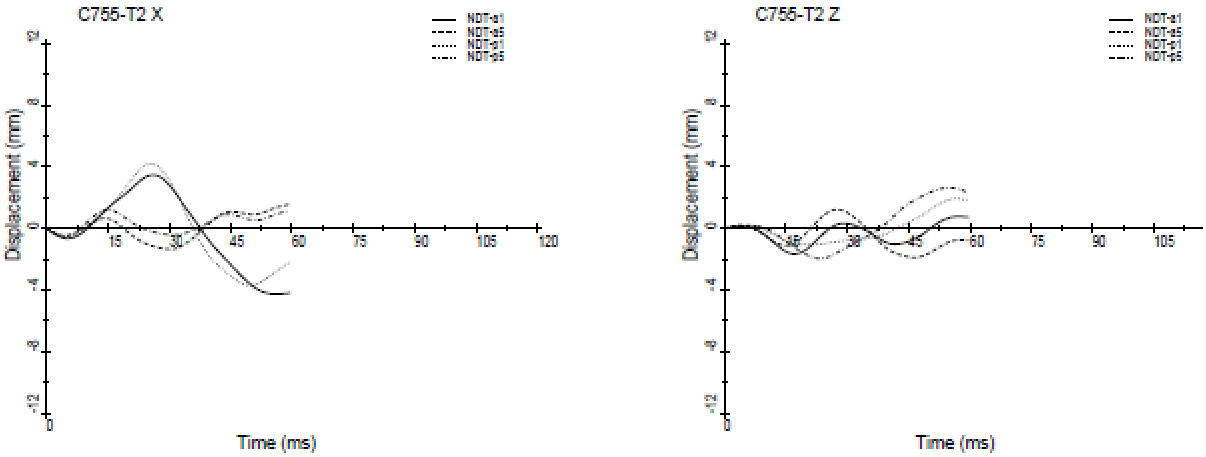

Figure 2-7 Hardy Displacement Results [19]

Adapted with permission from SAE International

In terms of validation, the finite element simulations tend not to show as good of a match to the reported experimental data as the pressure tests. Typically, the displacement curves match the proper direction and shape, but do not match the magnitude of the displacement as well.[20]–[23] A representative fit of the data from the displacement validation is shown in Figure 2-8. [20] One commonly reported reason for the larger discrepancy in brain displacement results between FE simulations and the experimental measurements is the approached used in modeling the CSF layer. Typically, the CSF is modelled as a solid with material properties representing water.[20]–[23] However, this approach over-constrains the brain, especially around the edges, resulting in an increase in strain, and a decrease in displacement.

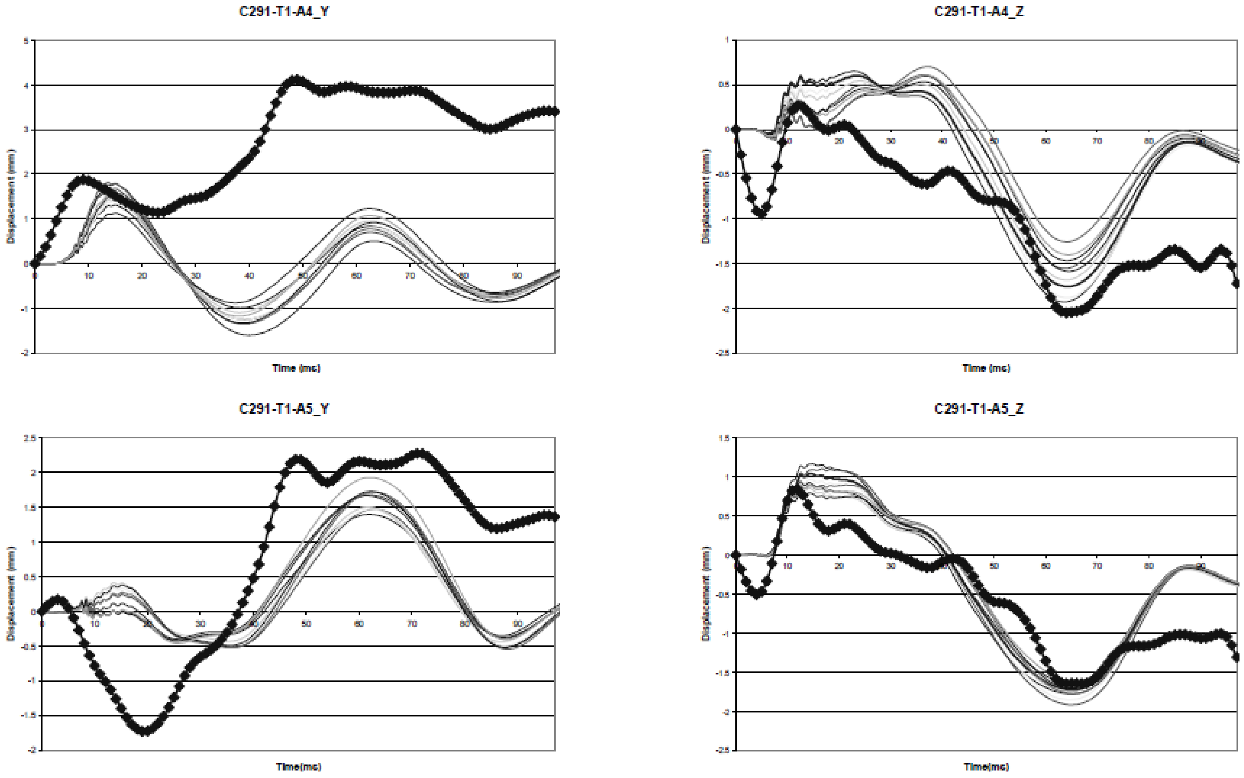

Grey: Model Prediction **Black**: Experimental Measurement

Figure 2-8 Displacement validation comparison [20]

Adapted with permission from SAE International

2.4 Sensor Location

In experimental impact studies, such as cadaver experiments, output variables such as pressure are measured at specific locations where the brain is instrumented. One limitation with this is the difficulty associated with precisely placing the sensors in the brain tissue. For example, the study by Nahum et al. used pressure sensors on the surface of the brain. The precise location of the sensors may vary due to the gyri and sulci on the surface. [9] Furthermore, measuring sensor location with respect to a common reference point presents an addition challenge. In order to compare the output of an FE simulation with experimental measures, a common reference must be used for the data. Output locations in FE models must be selected corresponding to locations that match with the experimental instrumentation. The historical paper by Nahum et al. in particular does not specify a precise location for the sensor measurements. Rather, it only mentions which lobe the sensor is located in. A sensor in the frontal lobe is not specific enough to make an accurate comparison of pressure values between an FE simulation and experimental measurement. The SIMON model explored taking different elements in the frontal lobe and comparing them to the experimental value reported by Nahum et al. [20] This showed a large sensitivity to location when plotting the pressure time history as shown in Figure 2-6. [20] However, little work has been done to quantify this sensitivity in either displacement or pressure.

Instrumentation location in the anthropomorphic physical model is also important. The pressure is not uniform across all brain regions, so choosing the right places to extract pressure information is critical for providing injury metrics. Researchers want to be able to output the maximal magnitudes to put into the injury criteria models. For long duration impacts (>2 ms) the pressure wave can be described as a quasi-static gradient that stretches across a slice of the brain.

This pressure gradient phenomenon is observed in all head impact FE models for long duration impacts. Thus, researchers have developed rudimentary equations to predict the pressure at different locations within the brain based on impact parameters. This is based upon the idea that the pressure is a uniform gradient across a slice of brain with its zero point in the center. This would create a positive and negative maximal location on either edge of the brain. If the impact parameters are known, the entire pressure gradient can be modelled as a linear gradient as seen in the equation below [26] where F_{max} is the maximum impact force, m is the mass of the head, ρ is the material density and r_c is the distance from the center of mass to the edge of the brain. This results in the P_{Quasi}, pressure at the edges of the brain.

$$P_{Quasi} = \frac{r_c \rho F_{max}}{m}$$

Using the knowledge that pressure acts as a gradient throughout the brain, the placement of sensors in the brain can be refined. Sensor location can be analyzed based upon where the sensor is located upon the line of action of the impact. This will allow for a more efficient use of sensors, and a more precise representation of key phenomena (coup and contrecoup pressures) during an impact event.

Finite element models are created to be a companion to experimental work. They can aid in developing injury metrics that reflect physical tissue damage and see a full field of view during an impact. Albeit there are some gaps in the literature, which this thesis will explore. The first being the method in which boundary conditions are applied to the simulations. Secondly, how much the output location in the simulation affects the output magnitudes. Lastly, how the pressure gradient effect can be utilized to determine the proper locations for pressure sensors.

Chapter 3. Model Development

3.1 BIPED Headform

The BIPED mk2 model is a physical surrogate model which aims to represent the human head. [7], [27] It includes key anatomical components that are meant to improve its bio-fidelity with respect to the human head. The elastomeric brain is surrounded by a cerebrospinal fluid (CSF) layer inside of a skull. Skin encompasses the skull, while a falx and tentorium membrane restrict the motion of the brain within the skull and provide rigidity in the model. A neck coupler and mass balance are added to connect the head to a neck and to balance the weight distribution to match other physical head forms. Figure 3-1 shows the physical head form.

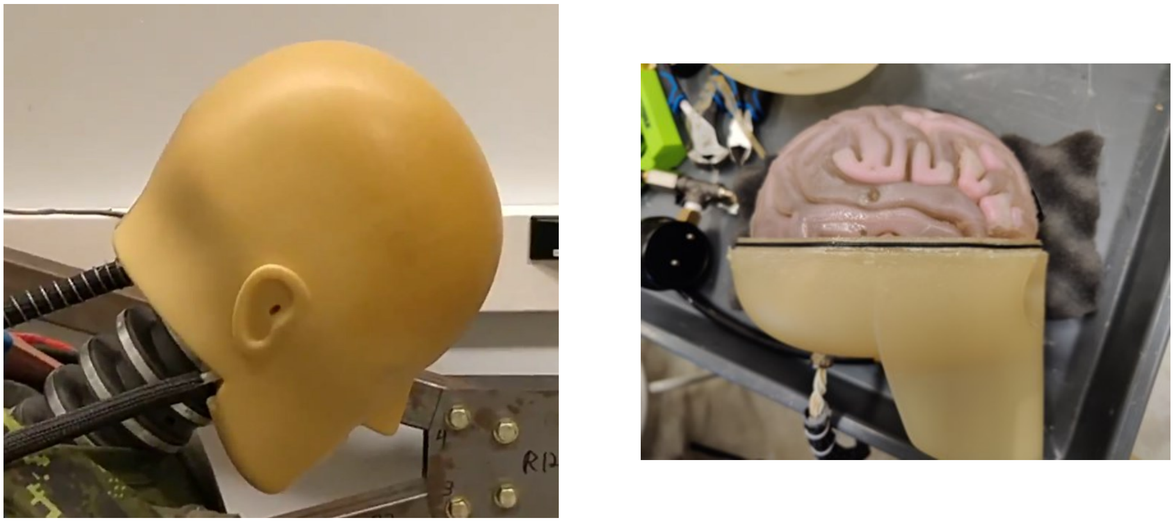

BIPED

Exposed brain and skull

Figure 3-1 Physical BIPED head form [8]

While the BIPED was previously used for blast wave testing, the current iteration of the BIPED is being evaluated in impact scenarios.[8] The instrumentation that the BIPED has reflects this objective. A 6-axis accelerometer (6DX Pro, DTS Inc.) is attached under the nose piece to monitor head kinematics. Two Kulite XCL-072 pressure sensors are located in the brain in order to capture pressures.[8] These are located on a sagittal slice of the brain, 15 mm from center at a front and back location. There are also CSF pressure sensors in this model, but the data from them was not used in this thesis. Radiopaque markers can also be cast into the brain material on the same 15 mm parasagittal slice in order for a x-ray system to determine displacement. [28] Figure 3-2 shows the location of both the radiopaque markers and pressure sensors.

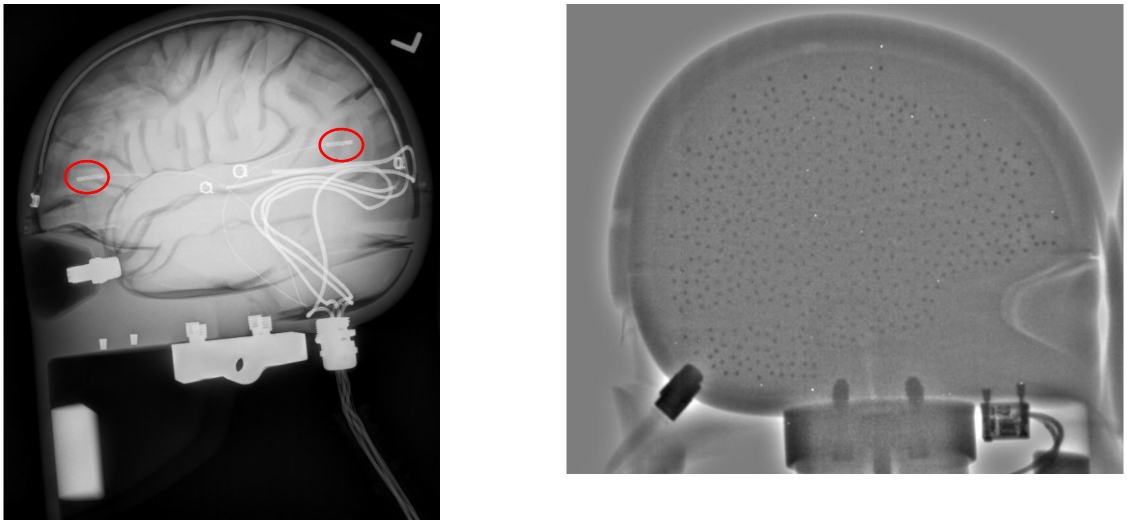

Pressure Sensors (Circled in red)

Radiopaque Markers (Black dots)

Figure 3-2 Instrumentation locations of the BIPED

3.2 Geometric Modelling

A finite element model was developed to replicate the BIPED including all of components of the physical model. Figure 3-3 and Figure 3-4 show the individual meshed components and assembly of the BIPED head form, respectively. In order to mesh and build the model, part files of each component were provided by DRDC. These CAD models were originally created to manufacture the physical BIPED and became the starting point of the computer model. These CAD files had to be cleaned where small geometric features were smoothed and merged. The skull, brain, and falx parts were imported into Solidworks (Dassault Systemes, France), positioned and assembled. A CSF layer was then generated from the empty space between the components and created as a new part. Lastly, the CSF layer was partitioned into multiple parts to ensure that the meshing would provide accurate results. This was due to the complex nature of the geometry at the CSF layer near the skull seam. By making it two sections, the CSF could be meshed with a uniform pattern. These sections of the same part were then tied together in the final assembly in ABAQUS.

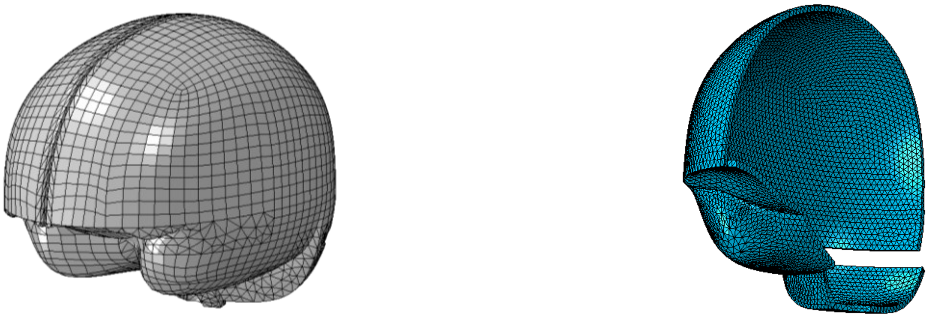

Brain

Cerebrospinal Fluid (half)

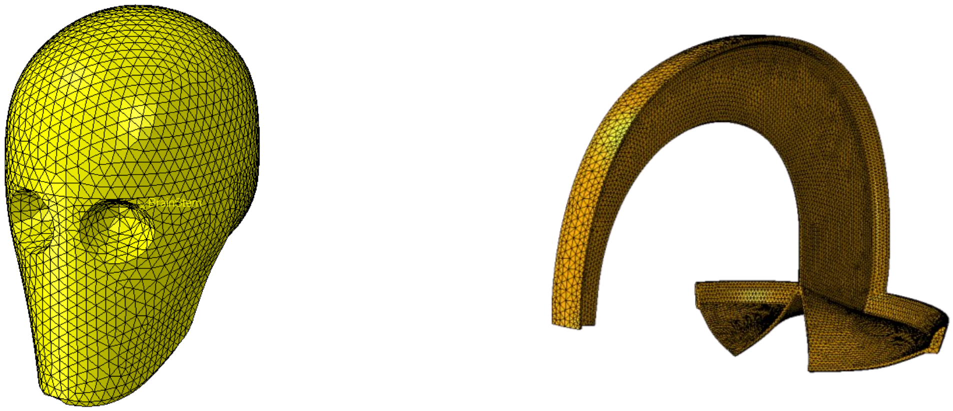

Skull

Falx and Tentorium Membranes (one piece)

Skin

DTS Sensor

Mass Balance

Neck Coupler

Figure 3-3 Meshed Parts of the BIPED Model

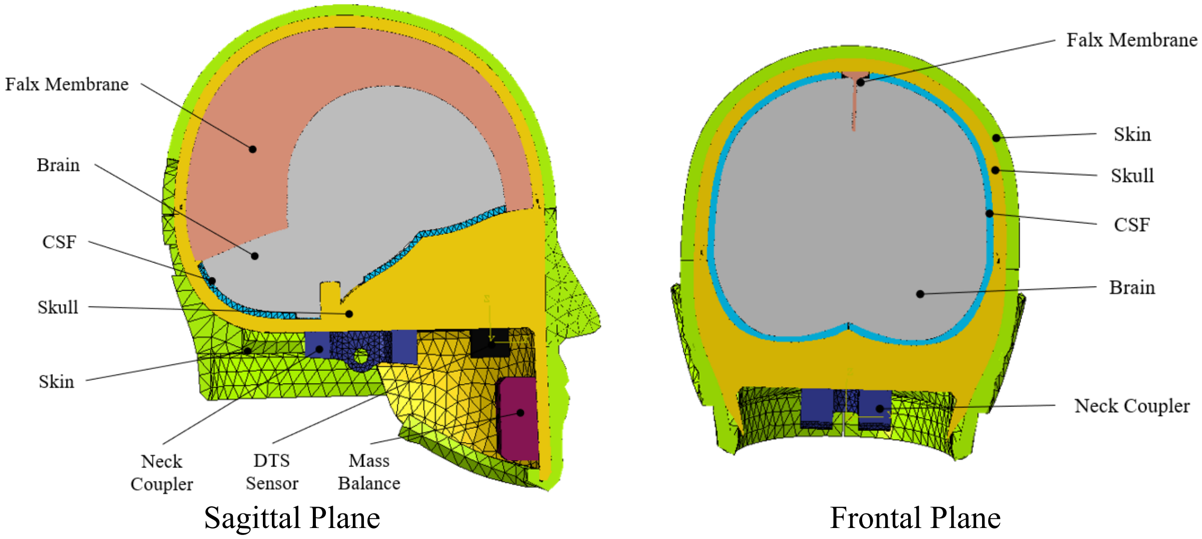

Figure 3-4 BIPED Assembly

3.3 Mesh Generation

All parts except the brain and CSF layer were meshed in the Hypermesh (Altair, United States) software before being imported to ABAQUS. Hypermesh has the ability to mesh geometrically complex parts efficiently with tetrahedrons. All of the elements in Hypermesh passed the basic analysis checks of size and shape and were deemed of acceptable quality. This prevented the meshes from failing during simulation, but were not in place to optimize size or shape characteristics. The brain was meshed in ABAQUS for multiple reasons. First it allowed more user control, which ensured that a full mesh convergence analysis could be undertaken, as well as more specific surface selection for constraints. It also allowed a more structured hexagonal mesh to be used for the brain component. The majority of the brain (left and right upper lobes) was meshed with reduced hexahedral elements (C3D8R) while the remaining, more complex geometric locations (brain stem, cerebellum, and around the falx membrane) were meshed using tetrahedral elements (C3D4). The CSF layer was meshed in ABAQUS as well using hexahedral elements. The summary of element sizes and element types can be found in Table 3-1. Overall, the full model consisted of 208,897 elements.

Table 3-1 Element Selection

Component	Meshing Software	Element Type	Approximate Element Size [mm]
CSF	ABAQUS	C3D8R	3
Brain	ABAQUS	C3D8R	5
Falx/Tentorium	Hypermesh	C3D4	1.5
Skin	Hypermesh	C3D4	7.5
Skull	Hypermesh	C3D4	7
Mass Balance	Hypermesh	C3D4	8.5
Neck Coupler	Hypermesh	C3D4	3
DTS Sensor	Hypermesh	C3D8R	10

Since the primary output variable of interest for this study was the response of the brain model, it was important to ensure that the chosen mesh did not influence the results significantly. Thus, a mesh convergence was undertaken for an impact scenario with a kinematic input, starting at a mesh size of 7 mm and decreasing by 1 mm until the difference between two adjacent mesh sizes was negligeable. The outcome parameter was the maximum pressure at four common nodes between the differently meshed models. The mesh convergence showed that a mesh size of 5 mm was sufficient to accurately capture pressure data in the brain from an impact scenario. The difference in pressures between a 5mm mesh and a finer 4mm mesh was an average of 1.7% for the locations tested as shown in Figure 3-5. This figure compares the maximum pressure at the four node sites, and is an alternative to a traditional scatter plot, as there are two few data points to visually see the proper convergence results.

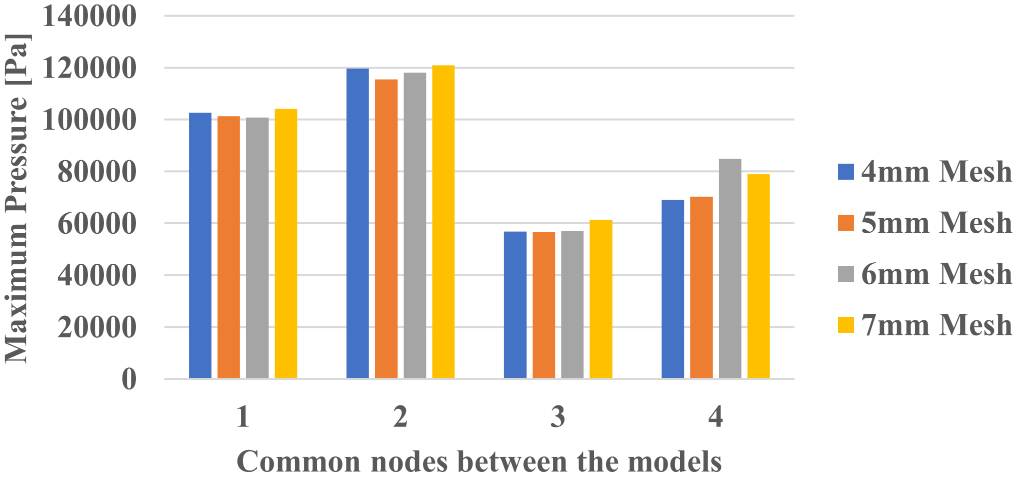

Figure 3-5 Mesh Convergence

3.4 Material Models

Since the physical model is made from synthetic materials, and not biological tissue, the material models are already well defined. The two exceptions to this are the brain material and fluid layer. The rest of the parts can be modelled with linear elastic materials as they undergo minimal deformation. [20] The following parts had linear elastic material models (Table 3-2): the falx/tentorium (neoprene), the skull (polyurethane), the skin (vitaflex 40), the neck coupler (steel 304) and the mass balance (aluminium 6061). A summary of the densities, elastic modulus and Poisson ratio can be found in Table 3-2 along with literature references to support the parameter values. In order to implement kinematic boundary conditions to the model at the DTS sensor location, the DTS sensor part was made to be rigid. This means that it could not undergo any deformation.

Table 3-2 Linear Elastic Material Properties

Component	**Material**	**Density [kg/m^3]**	**Elastic Modulus [GPa]**	**Poisson Ratio**
Falx Tentorium [27]	Neoprene	1200	0.0027	0.49
Skull [27]	Polyurethane	1200	2.275	0.30
Skin [7]	Vitaflex 40	1030	0.002	0.45
Neck Coupler [29]	Steel 304	7850	197	0.29
DTS Sensor [30]	Aluminium 6061	2700	2.75	0.33
Mass Balance [30]	Aluminium 6061	2700	2.75	0.33

3.4.1 Cerebrospinal Fluid Characterization

In many head impact FE models, pseudo fluid properties are applied to a Langrangian solid part to model the CSF layer. [9], [20]–[23] This is done as the computational cost and complexity of multi-physics modelling is high. Modelling CSF as a solid part is not without assumptions, as CSF is an incompressible fluid that cannot carry shear forces. Conversely, solid elements carry shear forces and depends largely on the element type to determine the amount of shear locking in the material. Shear locking is a phenomenon that describes the overestimation of shear stress in a material because of element types. [31] Tetrahedral elements are more likely to carry shear stress and limit the deformation for the material than hexahedral elements. [31] In the case of the CSF, hexahedral elements are important to minimize the amount of shear being carried in a fluid layer. While previous papers have expressed concerns over modelling the CSF layer as a solid, it has seemed to provide adequate results. [22]

The CSF layer was modelled using a Lagrange solid component in ABAQUS. ABAQUS has a built-in function that is recommended for this application called the “equation of state”. [32] This equation defines the relationship between the shock and particle velocity. Water can be modelled as a C_0 constant along with a viscosity. [32] The summary of CSF layer properties is outlined in Table 3-2.

Table 3-3 Water Material Properties

Component	Material	Density [kg/m^3]	Viscosity [Pa·s]	C_0
CSF [32]	Water	1000	0.01	1450

3.4.2 Brain Material Characterization

In the brain, most models are comprised of a hyperelastic model, with a viscoelastic component.[20]–[23] For the hyperelastic component, Ogden models are commonly used, but there are numerous different hyperelastic functions that can adequately describe the hyperelastic qualities of brain tissue. The Ogden strain density function relies on the principal stretches and material properties as seen in the equation below. [33] λ is the principal stretch and, μ and α represent material constants, while W is the strain energy density. If the Ogden model contains multiple terms, then the summation of the p terms comes into effect. For a single term Ogden model, the p subscript and the summation is ignored.

$$W = \sum_{p=1}^{N} \left[\frac{\mu_p}{\alpha_p} \left({\lambda_1}^{\alpha_p} + {\lambda_2}^{\alpha_p} + {\lambda_3}^{\alpha_p} - 3 \right) \right]$$

The viscoelastic component can be modelled multiple ways, but a common one is to use a Prony Series as seen in the equation below. [34] The G_∞ is the fully relaxed modulus, G is the initial modulus, and τ_i is the relaxation time associated with the i^{th} model component.

$$G = G_\infty + \sum_{i=1}^{N} G e^{\frac{-t}{\tau_i}}$$

In the case of the BIPED, the material used in the brain is Sylgard 527 which has been previously described with a hyperelastic Ogden model. [35] This was done by running a quasi-static compression test on a small disk of Sylgard 527. While this work was already available, curing of hydrogels at different temperatures or for different lengths of time can lead to differences in material properties. For this reason, the curing process that DRDC uses will be the material tested for the FE model.

In order to get material properties for the Sylgard 527 brain, material testing was undertaken. Brain material is largely considered hyperelastic and viscoelastic, and a sample of Sylgard 527 has been characterized using an Ogden hyperelastic model previously. [35] In order to further characterise the material, a stress relaxation compression test, and a quasi-static compression test were performed to obtain a single term Ogden model and a Prony viscoelastic model. A second reason was to ensure that the Sylgard material used in the material test was prepared and cured in the same manner as the experimental brains. Even though the literature had done a test on Sylgard 527, it may have been prepared slightly differently.[35] A Biomomentum, Mach-1 material tester was used for both experiments.

The quasi-static, uniaxial unconfined compression test used a cylindrical actuator to compress a 1 cm cube of Sylgard material to a 50% compression value. The cube material sample and experimental setup are shown in Figure 3-6. This was repeated on 3 Sylgard cubes, while the built-in camera on the Mach-1 recorded images at a 60 Hz frame rate. The force time history results were used to calculate true stress and true strain. To do this, the camera images were used to track the cross-sectional area of the cube as it underwent compression. (Figure 3-7) This was done using a program called Tracker (comPADRE, USA), where a calibration stick measured the initial undeformed length, and the deformed length was then calculated in every frame. The deformed configuration at each frame was used to calculate the true stress and true strain. These values were then averaged to find a mean and standard deviation curve of stress and strain.

An ABAQUS model of the cube and compressor was created and used to match the single term Ogden model to the experimental force time curve. This was done with a cube, and two plates as seen in Figure 3-8. First the boundary conditions in the simulation were confirmed by comparing the deformed shape of the model to the experimental cube. A tied boundary condition was used between the Sylgard 527 cube and the compression platen to represent the physical test. The material was sticky and would stick to the compression platen during the test. The force time curve was chosen as the comparison for the mechanical properties as it was the primary output of the mechanical test instrument, and thus unaffected by approximations of the cross-sectional areas.

Three parameters in the Ogden material model (α, μ, and bulk modulus D1) were determined through an iterative procedure by matching the force-time curve output from the FE model with that measured experimentally. It was found that the bulk modulus had no significant effect on the force-time curve in the simulation (an exact overlay), and thus the literature value of 1.878E-9 was used for the D1 bulk modulus. Iterations were done in increments of 50 for μ and 0.5 for α until the material curve from the simulation matched the experimental curve. These increments were chosen, as they provided discernible differences to the shape of the material curve. The iterations stopped when visually, the experimental force curve and the simulation force curves were indistinguishable, which took 10 iterations. Comparing to the existing model in literature, the stress strain data matched such that the new experimental curve fit within the standard deviations of the literature stress strain curve presented.[35] The results and final material parameters are shown in Figure 3-9 and Table 3-4.

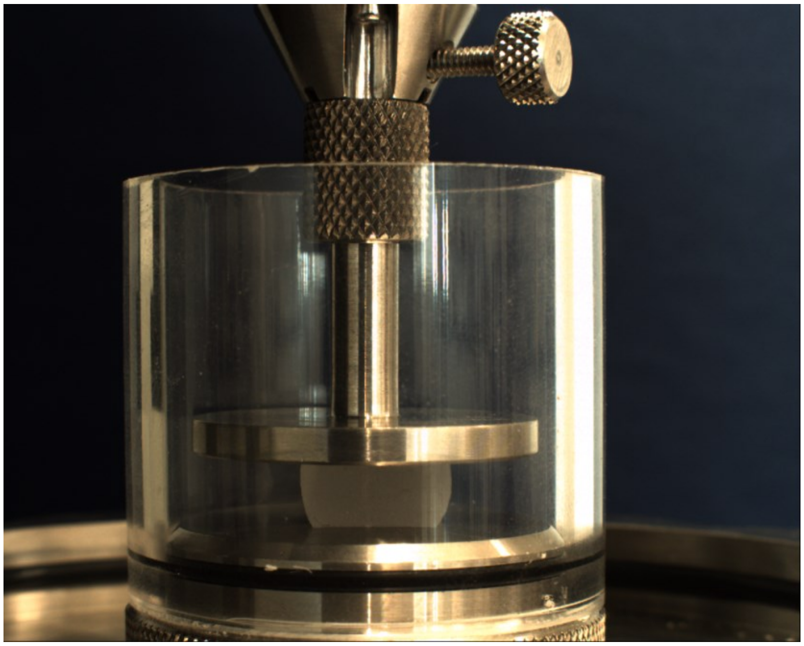

Figure 3-6 Experimental setup for the compression test

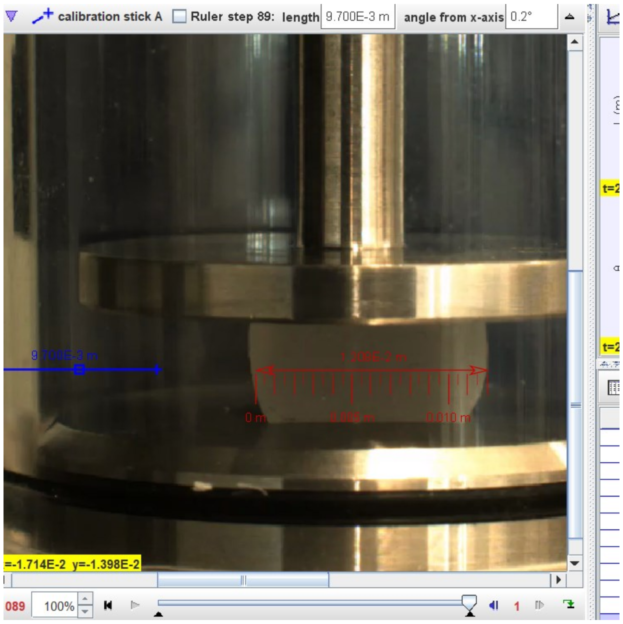

calibration stick A ☐ Ruler step 89: length 9.700E-3 m angle from x-axis 0.2°

Figure 3-7 Tracked images to measure cross section

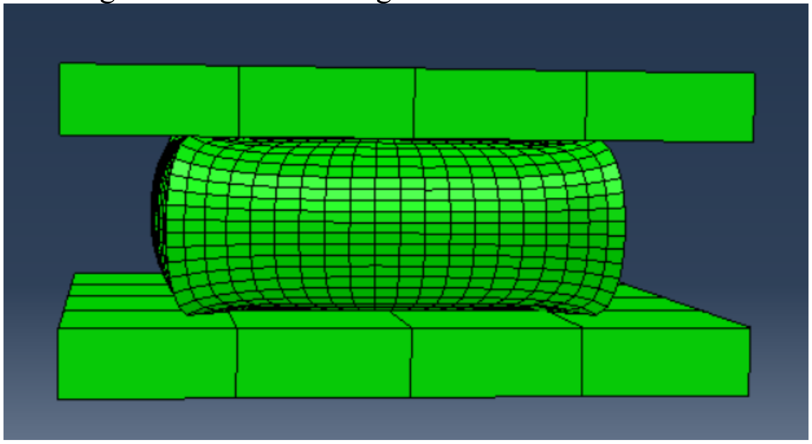

Figure 3-8 ABAQUS Compression Test Experimental Setup

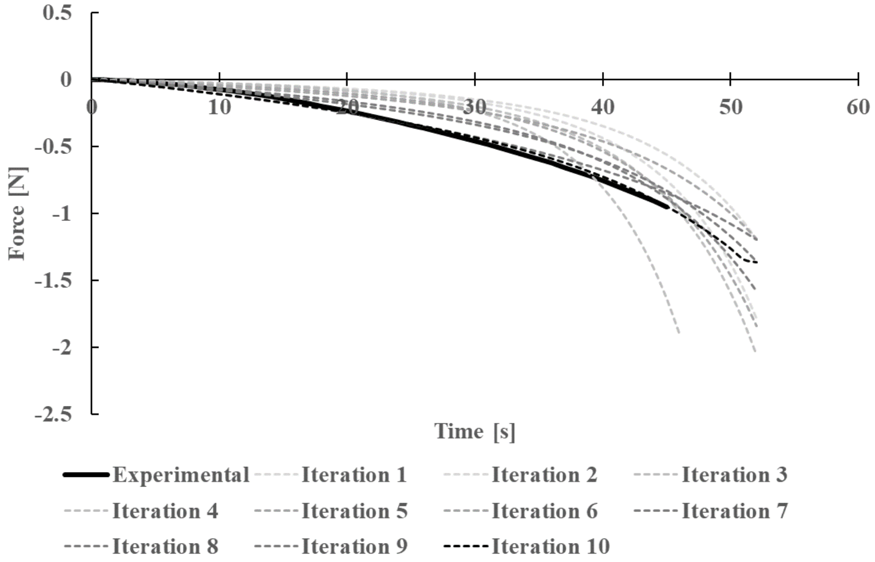

Figure 3-9 Iterations of Material Model using ABAQUS

Table 3-4 Brain Odgen Model

Component	Material	Density [kg/m^3]	μ	α	D1
Brain	Sylgard 527	970	550	4	1.878E-9

A Prony series viscoelastic model was developed by running a stress relaxation test using the Mach-1 material test instrument, where the Sylgard 527 sample was compressed to 50% and then held for 5 seconds. The stress on the Sylgard relaxed during those five seconds to form a curve. While strain rate values for brain impacts (36 to 241 /s) could not be met with the initial compression, the rate used on the Mach-1 machine was 70 mm/s (~ 7 /s strain rate). [36] Comparing to a pilot test done at 10 mm/s, the first section of the relaxation, from 0 to 0.05ms are almost indistinguishable from the 70 mm/s tests. This is the range of time the impact takes place, so we can assume that the strain rate does not significantly affect the response for this material analysis. A plot showing the mean and standard deviations of the viscoelastic curve is shown in Figure 3-10. The time series force data was then used in the ABAQUS material solver to match the force data to a three entry Prony series. ABAQUS uses a least squares approach in order to iterate for the matched material model parameters. The parameters are shown in Table 3-5, where G_i is the modulus and τ_i is the relaxation time constant.

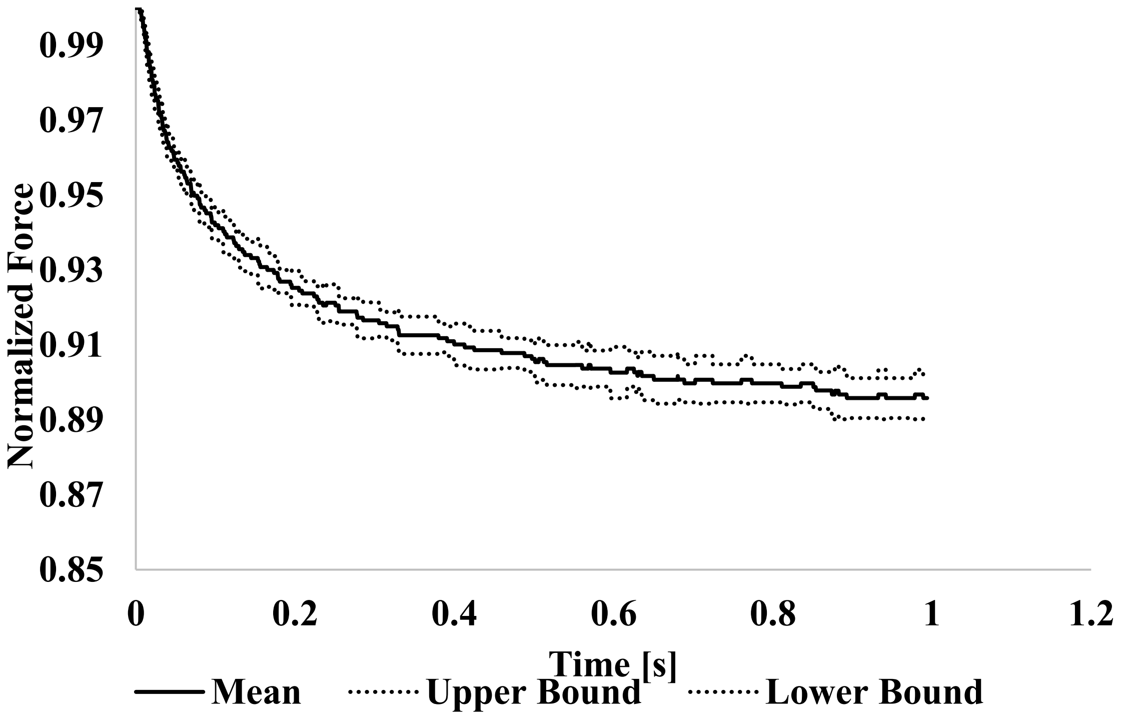

Figure 3-10 Viscoelastic Material Curves

Table 3-5 Brain Prony Series

Component	Material	G_i	τ_i
Brain	Sylgard 527	-0.00855	0.002795
		0.0495	0.0343
		0.063	0.267

3.5 Contacts and constraints

In most literature models, head components are combined using a surface to surface tied constraint. [21] This ensures that the surfaces do not separate. This approach has provided a good representation of experimental data. First, it provides a continuous material throughout an impact, making sure that the impulse travels without generating noise at surfaces impacting one another. Conversely, slight impacts between material components would mean the model develops gaps and overlapping material for short periods of time. Lastly, ties constraints provide the rigidity that the head experiences, especially in the skin, skull membrane connections where there is very little movement. The one area where the tied constraint is not representative of the physical system is the CSF-skull-brain interface. Ideally, the CSF would not carry any shear force, but using a tied constraint, it moves with the skull. This also constrains the brain around the edges as it does not allow unimpeded rotation. Most future work discussions centers around improving this connection. However, within the context of this work, as well as previously reported work, the tied constraint provides adequate results with the limitation and understanding that the strain in the brain areas around the edges may not be accurate. [10] It can be noted that some studies have provided alternative approaches. One such study used a tied constraint that allowed rotation of the surfaces. [22] This would allow the brain to rotate within the skull without being impeded by the CSF. This showed results that changed the magnitudes of peak pressures in the frontal and parietal regions of the brain, but no studies have done an analysis on nodal displacement with differences in sliding condition. [22] More research is needed before this can be implemented widely in head models.

Parts were assembled in ABAQUS using built in constraints. The origin for the model was selected to be the center of the DTS sensor. This was due to the kinematic inputs of the model being applied there. Each component was set in place by doing a full tie constraint to the components touching it. For example, the brain is tied to the falx and tentorium along the sagittal plane as well as the skull at the brain stem. It is then tied in place with the CSF in all of the other areas surrounding it. Each tie constraint is a surface-to-surface tie, meaning that the surfaces stay connected, and it does not allow node penetration. [37] [23]

3.6 Model Solution

The model is solved using the ABAQUS Explicit algorithm. This means that the simulation marches forward in time at set intervals based upon the stable time increment. The stable time increment is a calculation based upon the element size and material properties. This tells the solver what the largest increment the model can move forward in without risking becoming unstable. Parallelization was used to speed up the simulations, with all 8 cores being used. The computer used an Intel Core i7 processor to solve the simulations. On average, the simulation took an hour to solve each 0.0025 s of simulation. Input into the model was done using either a kinematic input of linear acceleration and rotational velocities to the rigid DTS sensor, or a kinetic force condition acting on the nodes of the skin. The outputs measured in the simulation were the pressure and nodal displacement of the brain. The model was validated by comparing these output parameters with experimental measurements as discussed in Chapter 4 and 5.

Chapter 4. Model Validation: Pressure

4.1 Objective

The objective of this chapter is to validate the finite element model with pressure experiments. It will also explore the differences between applying the boundary condition as either kinematics or kinetics.

4.2 Experimental Setup

Experimental impact tests were completed with the BIPED head form along with a Hybrid III body and neck as part of a parallel study. [38] The dummy was positioned seated and crouched forward with the neck at a 45-degree angle. The BIPED was placed on the neck, and the assembly was impacted with a pendulum at various speeds. The pressures in the brain (front and back), impact force, and head kinematics were recorded for each impact event. All of this was recorded at 25 kHz via Kulite XCL-072 sensors, PCB Crystal Quartz Force Plate, and a 6DX Pro accelerometer (DTS) respectively. A sample experimental setup is shown in Figure 4-1. In total 9 experiments were chosen to be recreated in the computer simulation, three impacts at three separate impact speeds, as seen in Table 4-1. These speeds correspond to impact energies common in blunt head impacts. [39]

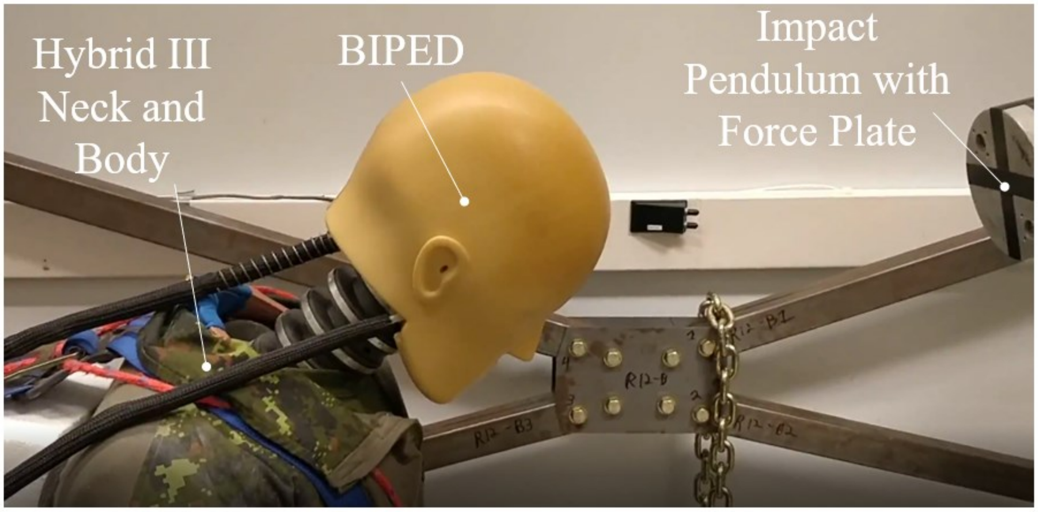

Figure 4-1 Pressure impact experimental Setup

Table 4-1 Test matrix for the pendulum impact pressure experiments

Experiment Name	Impact Velocity [m/s]	Peak Impact Force [N]
LowT0	2.48	4369.7
LowT1	2.48	4518.4
LowT2	2.48	4455.4
MedT1	3.42	6380.8
MedT2	3.39	6344.4
MedT3	3.19	6264.4
HighT0	3.84	6974.1
HighT1	3.84	7427.8
HighT3	3.82	6887.8

The inputs to the simulation were based upon the experimental data collected with either the pendulum force plate (kinetic force input) or the six degree of freedom accelerometer DTS sensor (kinematic input). Before the impact force could be input to the model, it was cut down to a 10 ms time window and then filtered at 1650 Hz using a 4th order Butterworth filter using the SAE standard.[40] It was then input into ABAQUS as a boundary condition. This boundary condition was applied at a singular front node of the skin at a 45 degree angle to represent the impact location direction of the experiment. An example input is found in Figure 4-2.

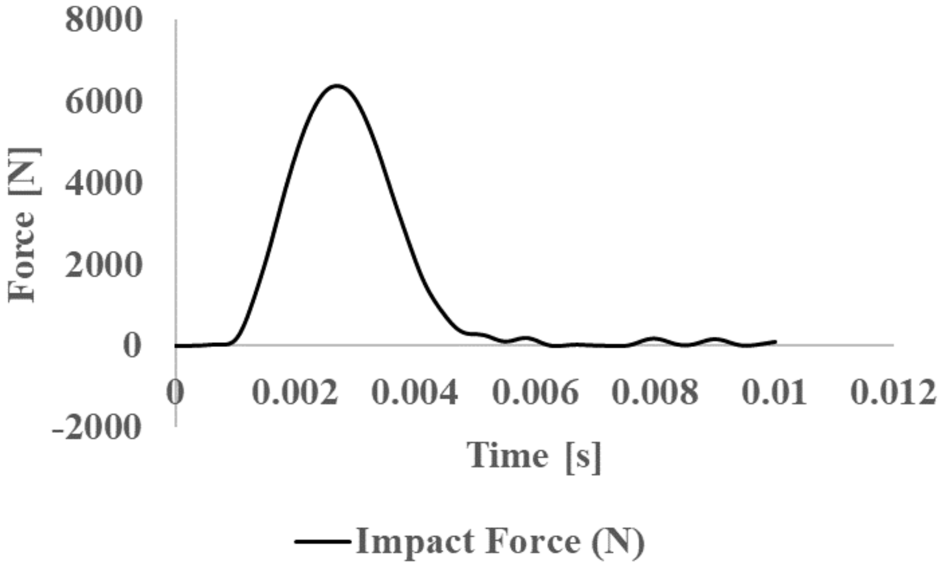

Figure 4-2 Kinetic inputs

For kinematic input, the acceleration data, sampled at 25 kHz, was filtered at 1650 Hz, as per SAE J211b (CFC 1000), to be input into ABAQUS. [40] The rotational velocity had low frequency oscillations, which affected the results, so SAE J211b allowed this signal to be filtered using CFC 180, a cutoff frequency of 300 Hz.[40] Six components were input into the ABAQUS model: linear acceleration x (anterior-posterior), y (medial-lateral), and z (superior-inferior) and rotational velocity x, y, and z. These became the boundary conditions for the model, input in to the DTS Sensor location. An example input is found in Figure 4-3.

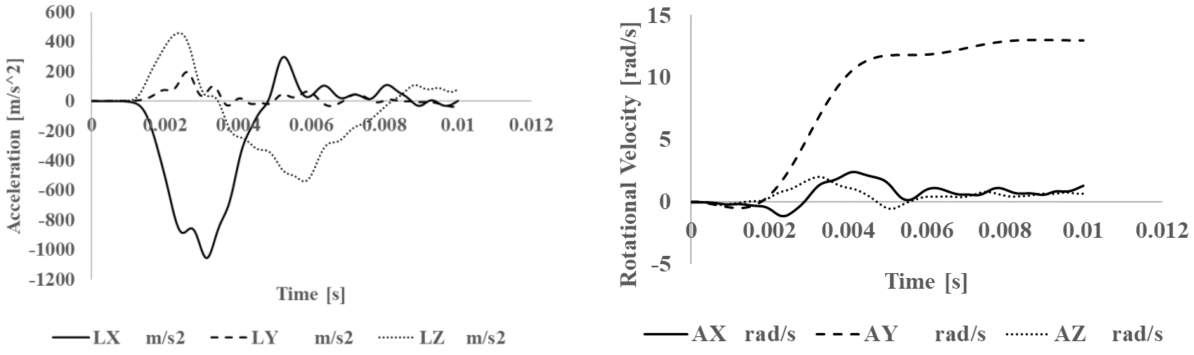

Linear Accelerations Rotational Velocities

Figure 4-3 Kinematic inputs

The pressure output frequency was set at 25 kHz for both of the pressure locations measured in the simulation. The model had two output points in the brain corresponding to the front and back pressure sensor locations. The locations of these sensors were determined with coordinates corresponding to x-ray images taken of the physical BIPED model. The locations of these sensors can be seen in Figure 4-4. These results were then filtered with a 4th order Butterworth filter at 4 kHz to match the onboard hardware filter on the pressure sensors.

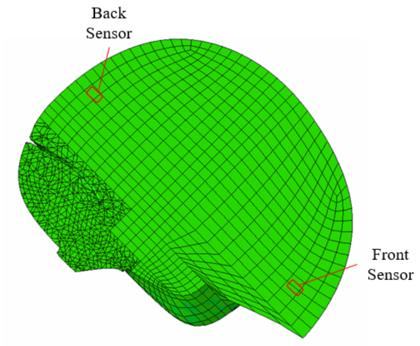

Figure 4-4 Pressure Impact Sensor Location (15mm from center sagittal slice)

4.3 Analysis

Data was processed using ABAQUS (Dassault Systemes, France), Excel (Microsoft, United States) and CORA (PDB, Germany). To evaluate the pressure and displacement time series data produced by the simulated impacts, a CORrelation and Analysis (CORA) was done. This method of analysis is used in impact biomechanics to compare human motion kinematics between experimental datasets.[8], [41] CORA is a method which evaluates the level of agreement using a cross-correlation technique. The cross-correlation is a weighted average of three curve characteristics: shape (50%), size (25%), and phase (25%). [42] To be in good agreement, Gehre et al. [42] suggests tested curves should have an overall rating greater or equal to 0.7. A fair correlation can be defined as a score of 0.5 to 0.7, while below 0.5 can be said to be a poor correlation. It has been shown that ratings of plus or minus 0.05 do not have a significant effect, implying room for interpretation within these scoring limits. [43] In the analysis, we used the default CORA parameters that have been reproduced in Table 4-2. D_Min and D_Max are the shares of the interval of evaluation, while Int_Min is the minimum overlap of the interval. K_V, K_G and K_P are the transition between ratings of 1 and 0 for the progression, size, and phase shift respectively. G_V, G_G and G_P are the weightings of the progression, size, and shape respectively.

Table 4-2 CORA analysis parameters for cross correlation method

D_Min	**D_Max**	**Int_Min**	**K_V**	**K_G**	**K_P**	**G_V**	**G_G**	**G_P**
0.01	0.12	0.8	10	1	1	0.5	0.25	0.25

A CORA analysis was done to compare the kinematic inputted pressure results to the experimentally measured pressure results and force inputted pressure results to the experimentally measured pressure results. The time window used in CORA covered the entire 10 ms impact, as the window of interest was the entire time series. The kinematics extracted at the sensor location for the force input simulations, were also compared to the experimentally determined kinematics. This allowed for another comparison between model inputs and enabled the observation of the effects of the neck boundary conditions on the kinematic response.

Peak pressures were also analyzed to find the error between the magnitudes of the experimental and simulated results. The maximum pressure was compared for the front sensor (coup pressure) while the minimum pressure was compared for the back sensor (contrecoup pressure). Error was calculated as the percent error of the simulated peak values compared to the experimental peak values.

In order to properly compare the differences between the kinematic and force input boundary conditions, the kinematics from the force input condition were extracted. The primary components of kinematics that described the movement, linear x and z accelerations, and rotational y velocity were outputted in the simulation at the DTS sensor location. These were then plotted alongside the experimental kinematics for the same impact.

4.4 Results

Typical time histories for the pressure response in the brain at both sensor locations can be seen in Figure 4-5. The shapes of the time histories are in agreement with the experimental findings, both for the kinematic and force inputs. For the front sensor, this is a large peak of pressure near the beginning of the simulated time, followed by the pressure decay. The back sensor observes a negative peak, followed by a positive peak before decaying. Time histories for all impacts can be found in the Appendix Figure A-1 and A-2.

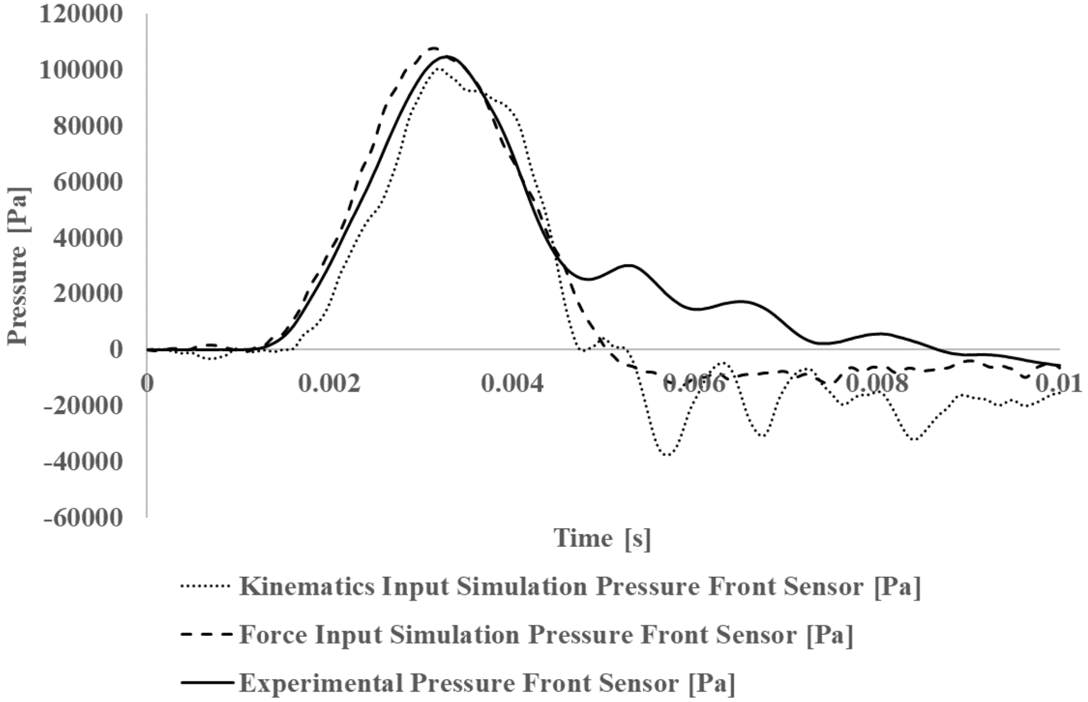

Front Sensor

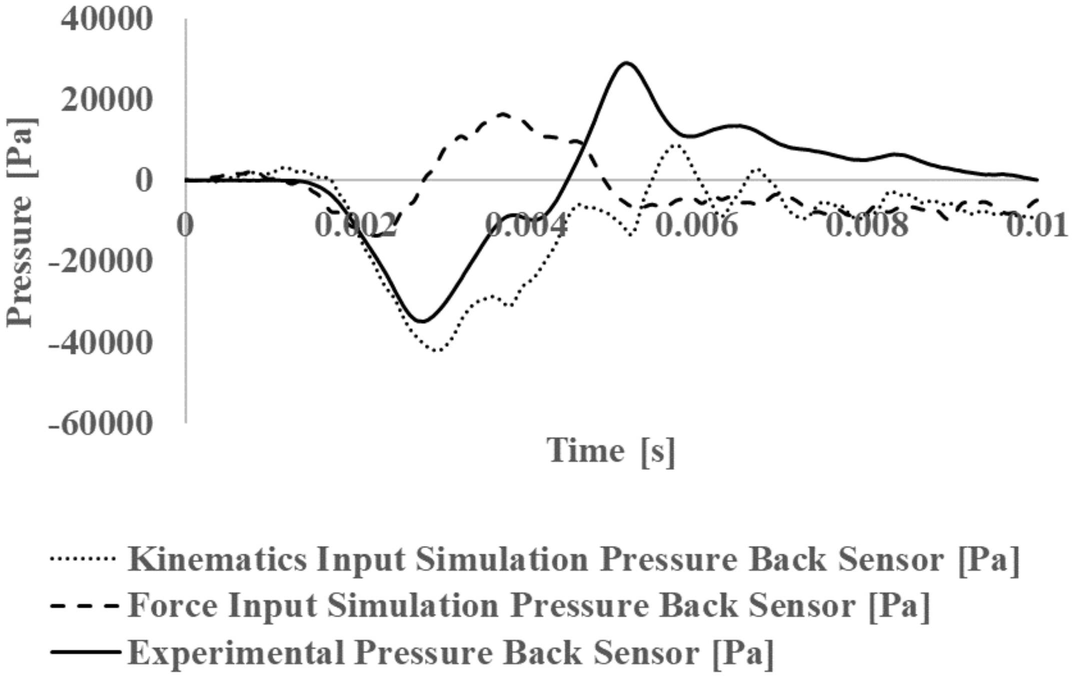

Back Sensor
Figure 4-5 Pressure time histories of the model for LowT1 impact

The typical pressure distribution in the brain for a crouched frontal impact is shown in Figure 4-6. Since the impact is a frontal impact, the pressure originates from the front side of the brain and propagates to the rear. As this occurs, a smaller negative pressure can be seen at the rear side of the brain, which is representative of the contrecoup pressure. This contrecoup pressure is well defined in the kinematic input case, but not as discernable in the force input case.

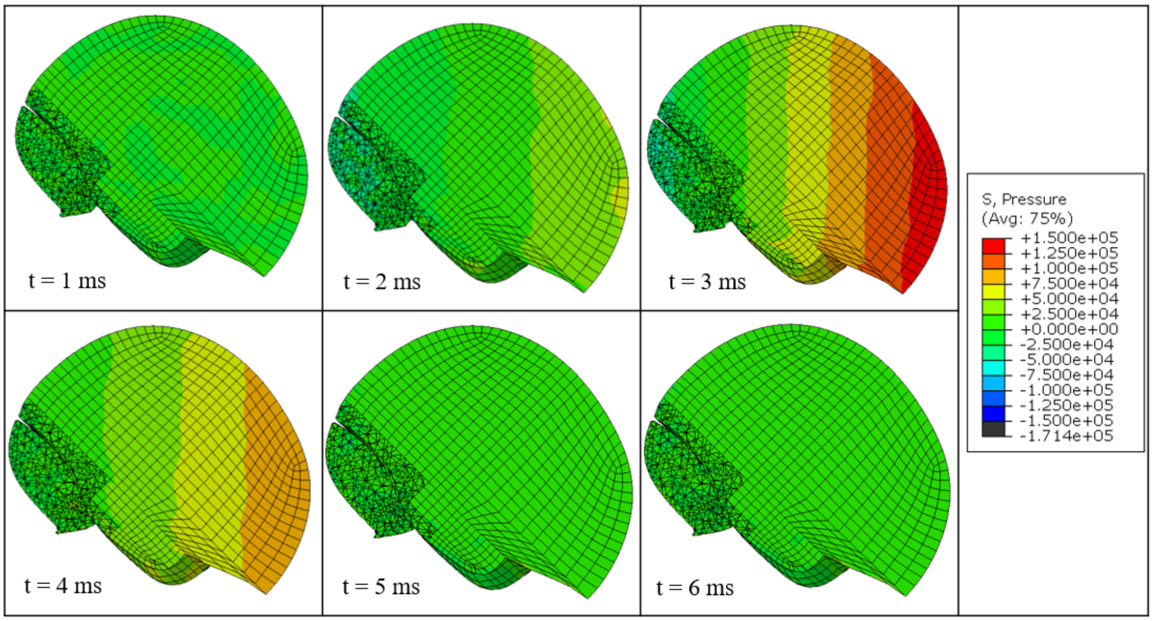

Force input

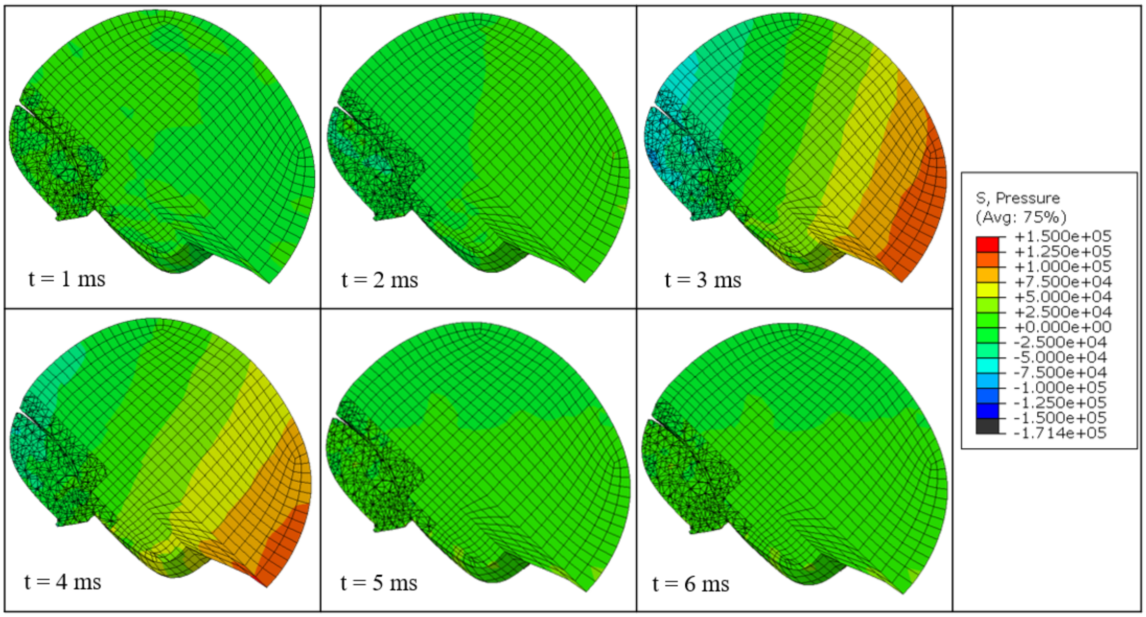

Kinematic input

Figure 4-6 Pressure test results for the pendulum LowT1 impact.

From the pressure time histories, the CORA analysis was run. The ratings for each of the coefficients, as well as the overall ratings can be seen in Table 4-3 for the front sensor and Table 4-4 for the back sensor. Overall ratings for the front sensor are deemed to be very good, with the values ranging from 0.649 to 0.766 for the kinematic input method and 0.827 to 0.874 for the force input method. Averaging the overall ratings led to a mean of 0.851 for the force input and 0.701

for the kinematic input (Table 4-3). Both of these averages surpass the threshold of 0.7 to be considered a good fit to the data.

The back sensor location ratings were not as conclusive, with the values for the force input ranging from 0.232 to 0.279 and kinematic inputs ranging from 0.401 to 0.466. The averages of the overall ratings for the force input are 0.255 and the kinematic input are 0.442. Both of these averages are considered poor based on the 0.5 threshold, but the kinematic results consistently gave numerically higher ratings compared to the force input. This is further backed up based upon the time series plots, which show the kinematic time series have more similar trends to the experimental data.

Table 4-3 CORA ratings for the pressure time histories front sensor

Impact name	Input Method	Shape [50%]	Size [25%]	Phase [25%]	Cross-Correlation Total
Low T0	Kinematic	0.534	0.995	1.000	**0.766**
	Force	0.749	0.998	1.000	**0.874**
Low T1	Kinematic	0.472	0.969	1.000	**0.728**
	Force	0.752	0.949	0.972	**0.856**
Low T2	Kinematic	0.455	0.986	1.000	**0.724**
	Force	0.739	0.951	0.972	**0.851**
Med T1	Kinematic	0.438	0.960	0.972	**0.702**
	Force	0.855	0.780	1.000	**0.873**
Med T2	Kinematic	0.325	0.947	1.000	**0.649**
	Force	0.708	0.912	1.000	**0.832**
Med T3	Kinematic	0.446	0.975	1.000	**0.717**
	Force	0.778	0.840	1.000	**0.849**
High T0	Kinematic	0.349	0.980	1.000	**0.669**
	Force	0.878	0.727	1.000	**0.871**
High T1	Kinematic	0.373	0.987	1.000	**0.683**
	Force	0.719	0.873	1.000	**0.827**
High T3	Kinematic	0.385	0.918	1.000	**0.672**
	Force	0.721	0.872	1.000	**0.828**
Average	Kinematic				**0.701**
	Force				**0.851**

Table 4-4 CORA ratings for the pressure time histories rear sensor

Impact name	Input Method	Shape [50%]	Size [25%]	Phase [25%]	Cross-Correlation Total
Low T0	Kinematic	0.177	0.749	0.735	**0.460**
	Force	0.002	0.378	0.735	**0.279**
Low T1	Kinematic	0.143	0.769	0.735	**0.448**

	Force	0.002	0.296	0.735	**0.259**
Low T2	Kinematic	0.177	0.814	0.696	**0.466**
	Force	0.003	0.272	0.696	**0.243**
Med T1	Kinematic	0.080	0.990	0.696	**0.461**
	Force	0.011	0.210	0.696	**0.232**
Med T2	Kinematic	0.066	0.927	0.735	**0.448**
	Force	0.005	0.344	0.696	**0.262**
Med T3	Kinematic	0.081	0.811	0.735	**0.427**
	Force	0.002	0.341	0.696	**0.260**
High T0	Kinematic	0.051	0.892	0.696	**0.422**
	Force	0.017	0.243	0.696	**0.243**
High T1	Kinematic	0.038	0.968	0.735	**0.445**
	Force	0.004	0.312	0.696	**0.254**
High T3	Kinematic	0.031	0.846	0.696	**0.401**
	Force	0.004	0.350	0.696	**0.263**
Average	Kinematic				**0.442**
	Force				**0.255**

In addition to the curve shape, the maximum magnitude of the pressure was compared for the front pressure sensor, and the minimum magnitude of the pressures was compared for the back pressure sensor. The results are presented in Table 4-5, Table 4-6, Table 4-7, and Table 4-8. As the simulated tests increased in impact speed and force, the peak pressure results also increased, which matched the experimental findings. For the force input, all of the front sensor magnitudes were within an average 10.67% error compared to the experimental measurements, while the back sensor magnitudes were within 55.88% error. Kinematic input tests yielded errors of 9.33% for the front sensor, while the back gave 27.54% error. The kinematic test outperformed the force input test on the back sensor, but the front sensor errors were very similar between the two input approaches.

Table 4-5 Force Input Simulation Front Sensor Error

	Experimental Pressure [Pa]	**Force Input Simulation Pressure [Pa]**	**Individual Error [%]**	**Average Error by Impact Severity [%]**
Low T0	110929	108522	2.17	2.93
Low T1	104622	107472	2.72	
Low T2	103040	107053	3.89	

Med T1	164706	140757	14.54	12.61
Med T2	170690	150627	11.75	
Med T3	166116	146927	11.55	
High T0	190509	146119	23.30	16.45
High T1	199890	175051	12.43	
High T3	207834	179486	13.64	
Average			**10.67**	

Table 4-6 Kinematic Input Simulation Front Sensor Error

	Experimental Pressure [Pa]	**Kinematic Input Simulation Pressure [Pa]**	**Individual Error [%]**	**Average Error by Impact Severity [%]**
Low T0	110929	102418	7.67	5.58
Low T1	104622	100364	4.07	
Low T2	103040	97896	4.99	
Med T1	164706	144588	12.21	12.81
Med T2	169968	144447	15.02	
Med T3	166116	147516	11.20	
High T0	190509	173342	9.01	9.61
High T1	199890	187881	6.01	
High T3	207834	179157	13.80	
Average			**9.33**	

Table 4-7 Force Input Simulation Back Sensor Pressure Error

	Experimental Pressure [Pa]	**Kinematic Input Simulation Pressure [Pa]**	**Individual Error [%]**	**Average Error by Impact Severity [%]**
Low T0	-36204	-16113	55.49	55.5
Low T1	-34847	-13747	60.55	
Low T2	-34159	-16921	50.46	
Med T1	-43466	-20923	51.86	49.54
Med T2	-40419	-22242	44.97	
Med T3	-39298	-18950	51.78	
High T0	-40024	-19210	52.00	62.6
High T2	-18870713	-24610	99.87	
High T3	-37597	-24088	35.93	
Average			**55.88**	

Table 4-8 Kinematic Input Simulation Back Sensor Pressure Error

	Experimental Pressure [Pa]	**Kinematic Input Simulation Pressure [Pa]**	**Individual Error [%]**	**Average Error by Impact Severity [%]**
Low T0	-36204	-40336	11.41	16.88
Low T1	-34847	-42184	21.06	

Low T2	-34159	-40370	18.18	
Med T1	-43466	-52701	21.25	
Med T2	-40383	-52279	29.46	26.05
Med T3	-39298	-50087	27.45	
High T0	-40024	-54528	36.24	
High T2	-40636	-54811	34.88	39.69
High T3	-37597	-55625	47.95	
Average			**27.54**	

Kinematic data was collected from the DTS sensor location for the force input pressure tests. This data was then compared against the experimentally measured kinematic data for the same experiment. The comparison of these kinematic curves can be seen in Figure 4-7. The linear x acceleration (Lx) simulated kinematics provided good estimates of the experimental data, while the linear z acceleration (Lz) was missing the distinctly negative phase present in the experimental data. The rotational y velocity (Ry) simulated data provided a good initial fit to the data in the first 0.002 seconds, but then did not continue to the same peak as the experimental values.

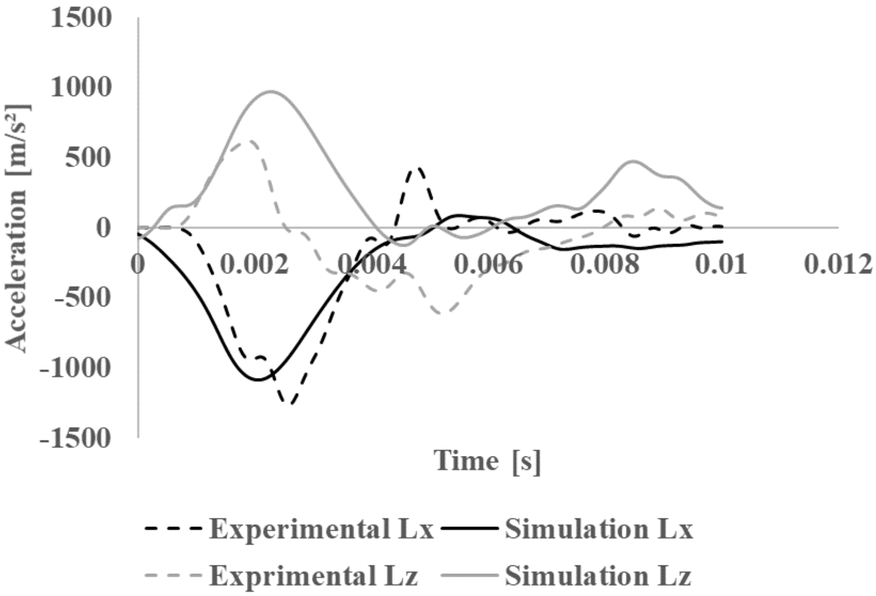

Linear Accelerations

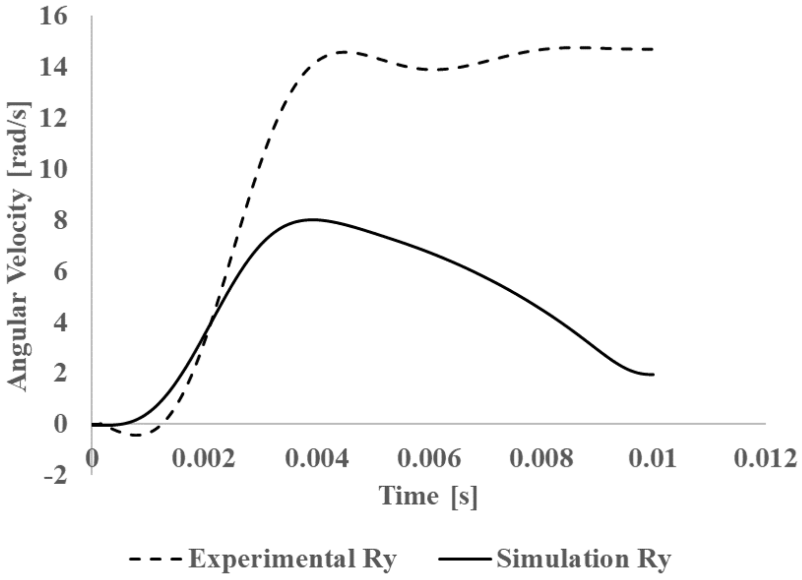

Rotational Velocities

Figure 4-7 Kinematics pulled from the force input High T1 impact

4.5 Discussion

The finite element model provides a good estimation of brain pressure for blunt impacts. It can successfully predict coup pressures for frontal impact energies corresponding to pendulum velocities of approximately 2 to 4 m/s. The contrecoup phenomena is observed in the simulation, but the results are not quite representative in their magnitudes.

The neck plays an important role in determining the response of the head kinematics during an impact. Since the head is attached to the experimental test device at the neck, the neck acts as the boundary condition needed to be applied to the model. Kinematic inputs to the simulation would already account for this boundary condition, as the kinematics are derived from the motion of the headform during the experiment. However, the force inputs would not account for this neck boundary condition, as the force was measured on the pendulum impactor. If the neck boundary condition made a difference in the pressure results, then a difference should appear in the two different input methods tested. From the time histories of the front sensor location, we can see only slight differences between the force and kinematic input data. CORA ratings from the two tests support this, as both are determined to be good fits. Contrasting this, the back sensor has differing pressure data between the two input methods. The kinematic data is much more representative of the experiment, and shows a strong correlation with the first negative peak. In the kinematic input, the neck compresses and physically stops the head from travelling in a singular direction. The force input does not do this, as it purely translates in space along the 45-degree x z plane. This difference in kinematics explains the difference in the back pressure sensor time history, as there is another force in force input case not being accounted for. This phenomenon was further supported by looking at the kinematic histories of the force input test. The z direction acceleration does not go through the distinct negative acceleration phase that the kinematics do experimentally. Rotation of the model was also not satisfied beyond the opening 3 milliseconds of the experiment. Both of these differences in kinematics help explain the discrepancies in the back pressure time histories between the kinematic and force input cases. Conclusions from this analysis indicate that to determine the pressure response in the brain near the impact site (coup pressure), a force or kinematic input can be utilised to equal effect. Conversely, for areas further away from the impact site, or near the neck, the kinematics give a more complete picture of the experimental pressure response. Kinematic inputs are also necessary to model motions over a longer period of time.

Overall, this comparison to BIPED experimental data in pressure provides a more complete set of results than previous cadaver finite element models. First, the geometry of the two models is the same, and the sensor locations in the experiment can be precisely replicated in the simulation. This allows for a more accurate comparison of pressure between model and experiment. Also, the comparison between the experiment and simulation was completed by looking at the entire time history response of the impact and not just the peak values. This allows our study to have confidence in the entire pressure response, as opposed to only matching one location at one time point. This study provides a more comprehensive comparison of the pressure response between experiment and simulation than previous head finite element models.

It is also important to note that the output of pressure in the simulation may not be equivalent to the pressure in the experiment. The sensors are not measuring a stress tensor value, but rather the force over a small sensor area. In the simulation, the best match to the physical sensors seems to be the pressure. Other outputs such as the principal stresses, and applied forces were also tried as outputs. Moving forward, perhaps having a better understanding of the physical sensor's finite element equivalent or modelling the actual sensors and the interaction with the brain tissue. This method was not pursued, as the sensors were smaller than the mesh size, and would have required refinement and precision that was not worth the modelling effort.

Chapter 5. Model Validation: Displacement

5.1 Objective

This chapter will use displacement experiments to help validate the BIPED finite element model.

5.2 Experimental Setup

The Hardy et al. displacement study was recreated using BIPED impacts created with a pneumatically driven linear impactor, and an unbiased neckform as part of a parallel study by Jennifer Rovt. [28] The BIPED underwent frontal impacts at a range of speeds with a low-compliance impactor face (MEP), and a high-compliance impactor face (VN foam). Two representative impacts were selected for comparison: a 2.04 m/s low-compliance impact and a 3.06 m/s high-compliance impact, as outlined in Table 5-1.

Table 5-1 Test Matrix for the displacement experiments

Experiment Name	Impact Velocity [m/s]
Hit 1	2.04
Hit 2	3.06

The simulation inputs were based on experimental accelerometer data collected using a six degree of freedom DTS sensor (6DX Pro). The kinematics were recorded at 20 MHz, filtered to 300 Hz, and normalized for input into ABAQUS.[28] Six components were input into the ABAQUS model as amplitudes: linear acceleration x (anterior-posterior), y (medial-lateral), and z (superior-inferior) and rotational velocity x, y, and z. These became the boundary conditions for the model, input at the sensor location. An example of a filtered set of normalized kinematics is presented below in Figure 5-2.

The displacement data was collected using a custom-built high-speed X-ray imaging system, coupled to the linear impactor. During the casting process of the BIPED brain surrogate a series of trackable elastomeric radiopaque markers were embedded in a parasagittal plane of the brain for displacement tracking. These radiopaque markers consisted of barium sulphate powder (60% by weight) mixed with humimic gel #4. The marker design was optimized in a previous study to minimize its interference in the displacement field of a surrounding Sylgard matrix [44]. The images were analyzed using an open-source DIC software package, NCorr [45], to calculate the displacement and strain fields, based on the motion of the markers. These techniques and the use of the BIPED for this type of displacement and intracranial strain measurement has been described previously [28]. A total of 70 ms of data was collected with a sampling rate of 5 kHz. A sample experimental setup is shown in Figure 5-1.

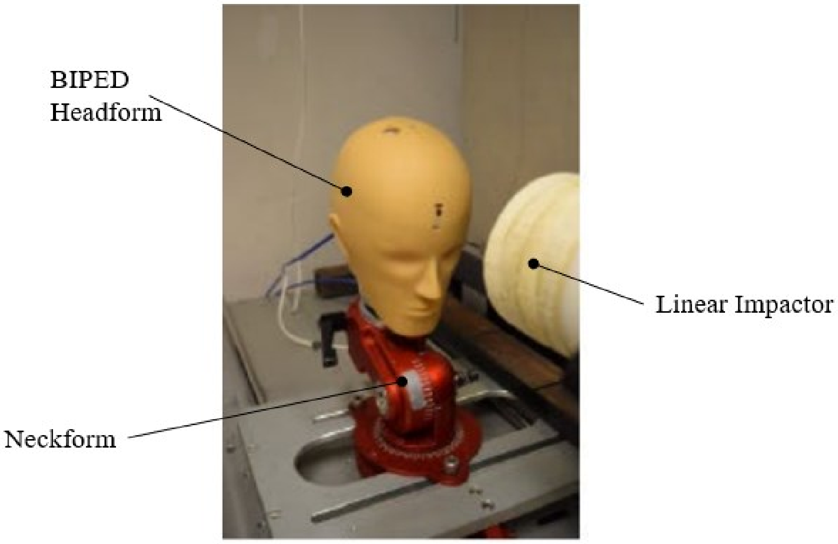

Figure 5-1 Displacement Impact Experimental Setup [46]

Six components were input into the ABAQUS model as amplitudes: linear acceleration x (anterior-posterior), y (medial-lateral), and z (superior-inferior) and rotational velocity x, y, and z. The kinematics were use instead of a force input, since the duration of the impact meant that the neck boundary condition affects the head motion. These became the boundary conditions for the model, input in to the DTS Sensor location. An example input is found in Figure 5-2.

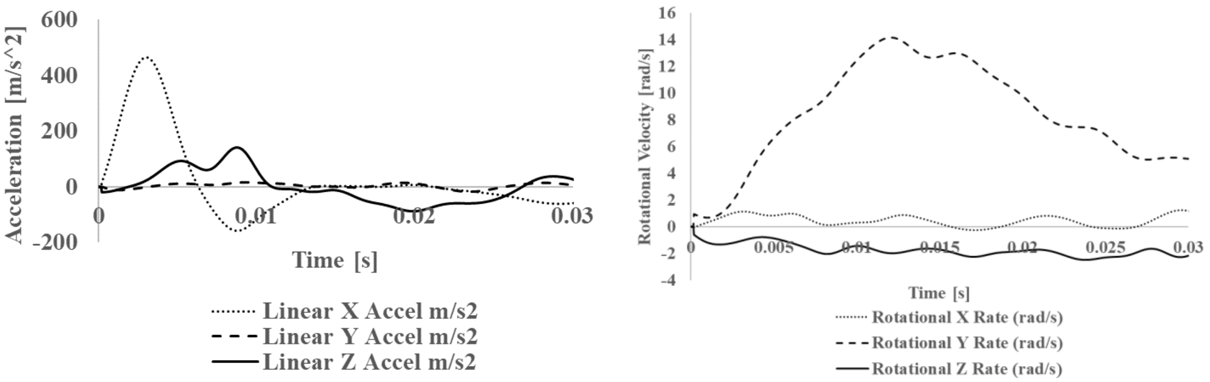

Linear Acceleration Rotational Velocity

Figure 5-2 Kinematic input displacement experiment

The output of the model were the x and z nodal displacements of 18 points in the brain, chosen to adequately represent a plane 15mm parasagittal (left). A skull fixed frame system was chosen at the DTS sensor and the relative motion compared to that sensor determined for each point. The nodal displacements were sampled at a frequency of 5 kHz. Corresponding pixel displacements in the x-ray video were extracted from the experimental results. The nodes chosen are shown in Figure 5-3.

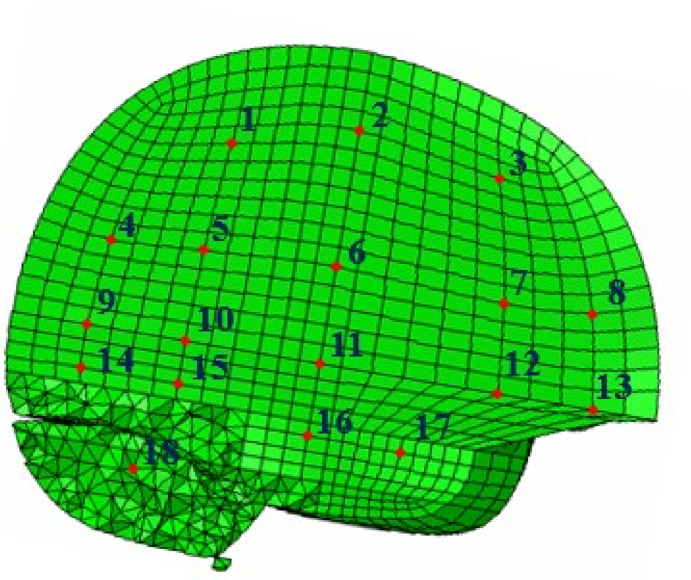

Figure 5-3 Position of displacement nodes

The x-ray experimental setup also has the ability to take the pixel displacement and convert it into principal strain. [28] This gave a full field view of the strain on the same 15 mm parasagittal slice of the brain. In the simulated model, an equivalent output with the same color map could also be made. This allowed for a visual comparison of the areas in which the simulation and physical model experienced similar strain values.

5.3 Analysis

For the displacement results, another CORA analysis was undertaken. The 18 displacement nodes in the simulation were compared to their corresponding experimental pixel displacement. The time window used for this CORA analysis was 30 ms, as there were issues with model stability after the first 30 ms. This time window encompasses the first peak of the displacement and is a commonly used time frame in brain strain studies.[23] See Chapter 4 for full CORA parameters and rationale.

5.4 Results

The typical x and z displacement time histories for the nodal displacements are shown in Figure 5-4. The shape and size of the displacement time histories are in agreement with the experimental data. At every point, there is a distinct displacement curve to the time history corresponding to the rotation of the brain in response to the frontal impact. The simulation results undergo the same rotations as the experiment. The model was better at capturing the areas of high displacement than low displacement as shown in Figure 5-4. The remaining 17 points for both hit 1 and 2 can be found in the Appendix: Figure A-3 and A-4.

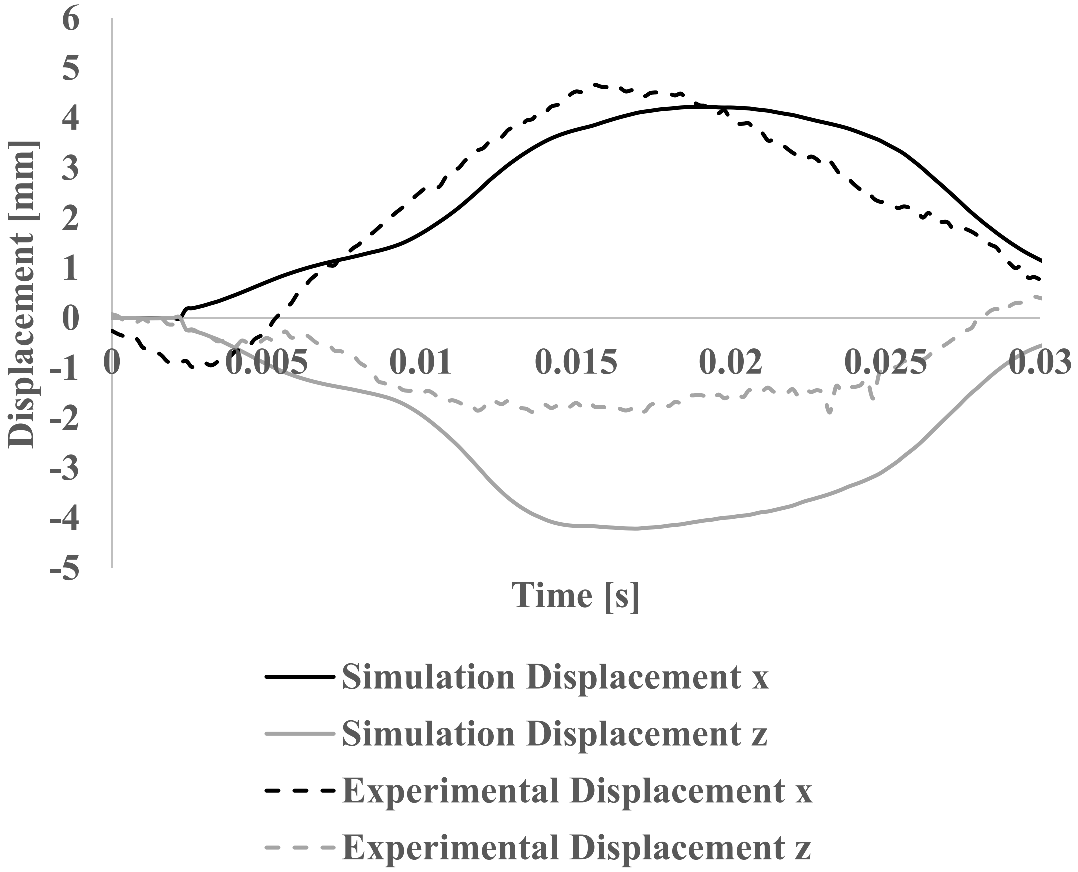

Figure 5-4 X and Z displacements of node 5

To quantify the match of the displacement and strain between the model and the experiment, a CORA analysis was run on the x and z displacements of all 18 extracted points. The Hit 1 overall ratings ranged from 0.016 to 0.890. The average for the overall ratings was 0.538, which would indicate a fair correlation with the data, but not one that is objectively great. For Hit 2, the overall ratings range from 0.012 to 0.936, with an average of 0.569. Again, these values confirm that the simulation results agree with the experimental data. The CORA results solidify what was observed in the time history results, as the better CORA scores were from high displacement regions. A summary of the CORA values can be seen in Table 5-2 and Table 5-3.

Table 5-2 CORA ratings for Hit 1

Point	**Direction**	**Shape [50%]**	**Size [25%]**	**Phase [25%]**	**Cross-Correlation Total**
Point 1	X	0.891	0.997	0.344	**0.781**
Point 1	Z	0.967	0.195	0.468	**0.650**
Point 2	X	0.952	0.648	0.032	**0.646**
Point 2	Z	0.000	0.338	0.966	**0.326**
Point 3	X	0.927	0.620	0.000	**0.619**
Point 3	Z	0.945	0.325	0.281	**0.624**
Point 4	X	0.000	0.188	0.966	**0.289**
Point 4	Z	0.926	0.364	0.904	**0.780**
Point 5	X	0.008	0.184	0.000	**0.050**
Point 5	Z	0.976	0.605	0.344	**0.725**
Point 6	X	0.014	0.234	0.000	**0.065**
Point 6	Z	0.000	0.271	1.000	**0.318**
Point 7	X	0.000	0.229	0.000	**0.057**
Point 7	Z	0.973	0.958	0.000	**0.726**
Point 8	X	0.000	0.543	0.000	**0.136**
Point 8	Z	0.945	0.524	0.157	**0.643**
Point 9	X	0.230	0.489	0.966	**0.479**
Point 9	Z	0.920	0.371	0.593	**0.701**
Point 10	X	0.802	0.566	0.966	**0.781**
Point 10	Z	0.922	0.752	0.966	**0.890**
Point 11	X	0.929	0.759	0.842	**0.865**
Point 11	Z	0.921	0.463	0.000	**0.576**
Point 12	X	0.913	0.245	0.780	**0.713**
Point 12	Z	0.954	0.776	0.406	**0.773**
Point 13	X	0.046	0.045	0.000	**0.035**
Point 13	Z	0.010	0.044	0.000	**0.016**
Point 14	X	0.210	0.360	0.966	**0.437**
Point 14	Z	0.842	0.142	0.219	**0.511**
Point 15	X	0.717	0.226	0.966	**0.656**
Point 15	Z	0.655	0.859	0.966	**0.784**
Point 16	X	0.982	0.808	0.966	**0.934**
Point 16	Z	0.921	0.631	0.000	**0.618**
Point 17	X	0.960	*0.087	0.966	**0.743**
Point 17	Z	0.033	0.011	0.966	**0.261**
Point 18	X	0.415	0.417	0.966	**0.553**
Point 18	Z	0.350	0.702	1.000	**0.600**

Table 5-3 CORA ratings for Hit 2

Point	**Direction**	**Shape [50%]**	**Size [25%]**	**Phase [25%]**	**Cross-Correlation Total**
Point 1	X	0.960	0.489	1.000	**0.852**
Point 1	Z	0.803	0.278	0.966	**0.713**
Point 2	X	0.965	0.961	0.717	**0.902**
Point 2	Z	0.000	0.182	0.966	**0.287**
Point 3	X	0.952	0.886	0.780	**0.892**
Point 3	Z	0.986	0.408	0.531	**0.728**
Point 4	X	0.000	0.034	0.966	**0.250**
Point 4	Z	0.900	0.625	0.966	**0.848**
Point 5	X	0.020	0.008	0.966	**0.254**
Point 5	Z	0.937	0.876	0.966	**0.929**
Point 6	X	0.293	0.712	0.966	**0.566**
Point 6	Z	0.000	0.645	0.281	**0.232**
Point 7	X	0.000	0.050	0.000	**0.012**
Point 7	Z	0.989	0.875	0.095	**0.737**
Point 8	X	0.000	0.490	0.000	**0.122**
Point 8	Z	0.988	0.665	0.593	**0.809**
Point 9	X	0.000	0.222	0.966	**0.297**
Point 9	Z	0.847	0.704	0.966	**0.841**
Point 10	X	0.802	0.198	0.468	**0.567**
Point 10	Z	0.872	0.554	0.966	**0.816**
Point 11	X	0.968	0.991	0.406	**0.833**
Point 11	Z	0.926	0.318	0.219	**0.597**
Point 12	X	0.987	0.297	0.531	**0.700**
Point 12	Z	0.965	0.549	0.281	**0.690**
Point 13	X	0.627	0.047	0.000	**0.325**
Point 13	Z	0.364	0.068	0.000	**0.199**
Point 14	X	0.000	0.069	0.966	**0.259**
Point 14	Z	0.738	0.972	0.966	**0.854**
Point 15	X	0.555	0.043	0.593	**0.436**
Point 15	Z	0.622	0.398	0.966	**0.652**
Point 16	X	0.973	0.831	0.966	**0.936**
Point 16	Z	0.913	0.436	0.344	**0.651**
Point 17	X	0.985	0.133	1.000	**0.776**
Point 17	Z	0.000	0.171	0.000	**0.043**
Point 18	X	0.004	0.193	0.966	**0.292**
Point 18	Z	0.607	0.169	0.966	**0.587**

The maximum principal strain at four time points throughout the impact is also shown in Figure 5-5. The simulated results are on the bottom, while the experimental results are on the figure top. This comparison shows the regions of the brain that have similar strain, while also highlighting the differences between the model and physical brains. The same low strain center of the brain is present in both the experiment and simulation, while the strain values are similar around it. On the edges of the brain, the simulation values are higher than the experimental.

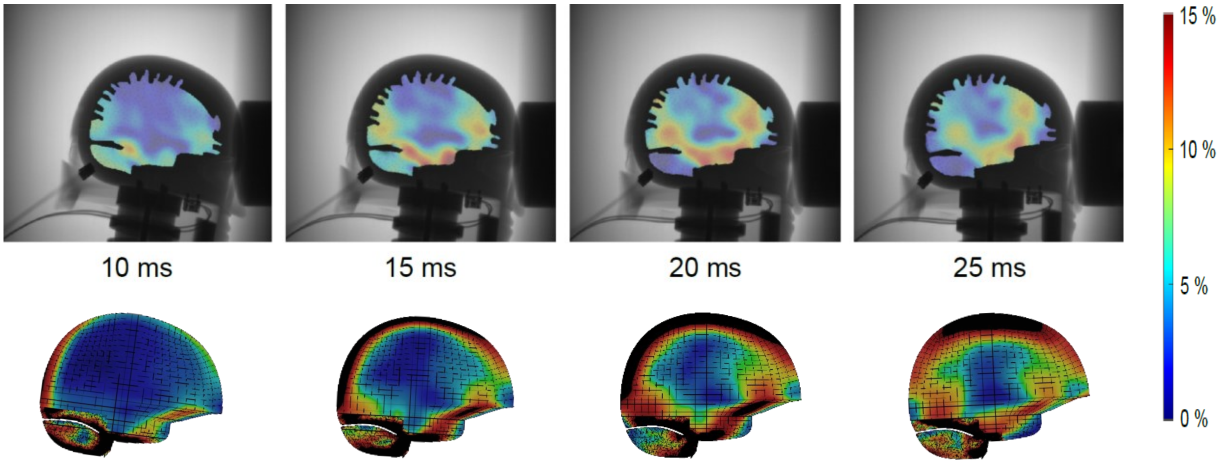

Figure 5-5 Maximum principal strain for Hit 1

5.5 Discussion

In addition to the pressure response in the brain, the finite element model can predict the displacements of specific points in the brain for frontal impact energies with impact speeds ranging from 2 to 3 m/s.

Boundary conditions for the model were selected based upon two things: the ability of the model to run without elements being distorted and the simulation failing, and whether the conditions were realistic. Realistic conditions would have the fluid layer be able to distort and flow around the brain without carrying any shear forces. Due to the nature of the ABAQUS Explicit model, and the need to have the fluid change pressures during impact, the fluid was modelled by a Lagrange solid material. This meant that the brain was fixed in place at its surface and could never move through the fluid, though the fluid layer could compress and stretch. This fluid layer was then joined to both the skull and brain parts by a tied constraint. This allowed for a continuous part with no separation. An alternative approach was investigated where a contact condition was applied to the model, which would allow the three parts to contact one another without necessarily remaining attached. Results from this test were unrepresentative of a continuous pressure wave propagating through the brain, due to the fact that the layers could separate from one another and produce gaps between the materials. ABAQUS also had difficulty in keeping the layers from intersecting briefly due to the impact severity. A sliding boundary condition which does not allow separation on the CSF, brain, and skull would have been the most intuitive solution to provide a realistic boundary condition for these parts, but ABAQUS could not run the model with this condition due to excessive distortion of some elements. This condition was applied to models in literature [22], and showed improvement over a regular tied constraint that has been a standard for most finite element head models. [37] More research into applying this condition on the BIPED model in ABAQUS is necessary.

This limitation in the boundary condition most likely led to some unrealistic strain results in the current model, as the brain would not be subject to large strains at the interface of the fluid layer as seen in the simulations. This was the one major region of inconsistency in the strain field, and led to disparities in the displacement results of points around the edge of the brain. This is evident in the three edge points tested: point 8,13,17. On average these points scored drastically worse than the more interior points since the brain was over constrained on the edges of the model.

Overall, the model satisfied the research questions it wanted to answer. The BIPED FE model can accurately represent experimental pressure and displacement data. Analysis into boundary condition both for the input methods, as well as for contact constraints were explored to further the understanding of head impact finite element modelling. This concludes the objective to partially validate the BIPED FE model under impact conditions. Both the pressures and nodal displacements provided results that lead to a confidence that the simulation can represent these parameters in similar impact velocities.

This study undertook a more comprehensive comparison to displacement values than previous cadaver finite element models. As was the case for the pressure comparison, our BIPED model contains the exact geometry of the physical model. This means that the comparison points are the exact locations of the experimental data. Comparison between the experiment and simulation was completed by looking at the entire time history response of the impact and not just the peak values. This allows our study to have confidence in the entire nodal displacement response, as opposed to only matching one location at one time point. This study provided a view of the displacement over a total of 18 points in a sagittal slice as opposed to a few select locations.

It also provided an entire field of view strain comparison between the simulation and experiment. Overall, this comparison to experimental nodal displacement results is more complete than previous cadaver finite element work.

Chapter 6. Effect of Sensor Placement

6.1 Objective

The primary objective of this chapter is to determine the sensitivity of the model outputs to location changes. It will also determine how well the sensor placement captures the pressure response in the brain. This will be done by analysing the impacts discussed in Chapters 4 and 5, as well as new helmeted impacts.

6.2 Experimental Setup

In order to collect helmeted drop data on the BIPED, the Advanced Combat Helmet (ACH) blunt impact drop test configuration was used.[16] The orientations in the ACH document have ranges, so the true angles tested are specified in Table 6-1.This involved using the drop tower in six configurations and two heights. Overall, the drop mass, excluding helmet was meant to be 15 ± 1 kg, and with the carriage weighing 11kg and the BIPED weighing 4.5 kg, this was within the guidelines set out by the ACH standard. The helmet used was a standard modern military issue helmet, placed upon the BIPED following the guide for fit with the distance from the helmet brim to the nose. This helmet fit procedure is outlined in previous research on bicycle helmets and modified to make the miliary helmet sit 75 mm from the tip of the nose to the helmet brim. [47] On every impact this was readjusted. Of the recommended velocities to test the helmet in the ACH standard they were all deemed too high for the BIPED to withstand based on skull seam leakage on earlier trials. This narrowed the test down to two speeds, both below the lowest velocity specified in the standard. The BIPED was mounted on the Hybrid III neck, which was then mounted on the drop carriage that had the ability to rotate the neck angle and the inclination angle into six positions. A velocity gate measured the velocity of the drop carriage immediately prior to impact. These angles and orientations are shown in Table 6-1 and Figure 6-2. Five drops were performed at each height and orientation. All tests were deemed acceptable based upon the velocity gate measurement being within 5% of the target value. Additionally, the unhelmeted impacts used for the pressure validation and the displacement validation experiments (Chapter 4 and 5 respectively) were also used in the sensitivity analysis presented here.

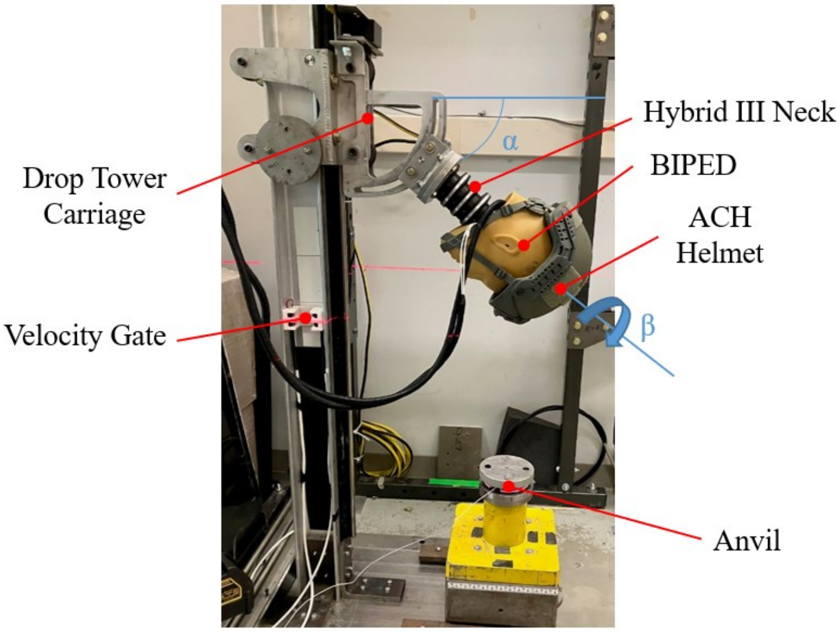

Figure 6-1 Drop Tower Experimental Setup

Table 6-1 Helmeted Impact Orientations

Orientation	**α [º]**	**β [º]**
Front	40	0
Crown	85	0
Front Boss	40	50
Rear Boss	20	150
Rear	5	180
Side	30	90

Front Front Boss Crown

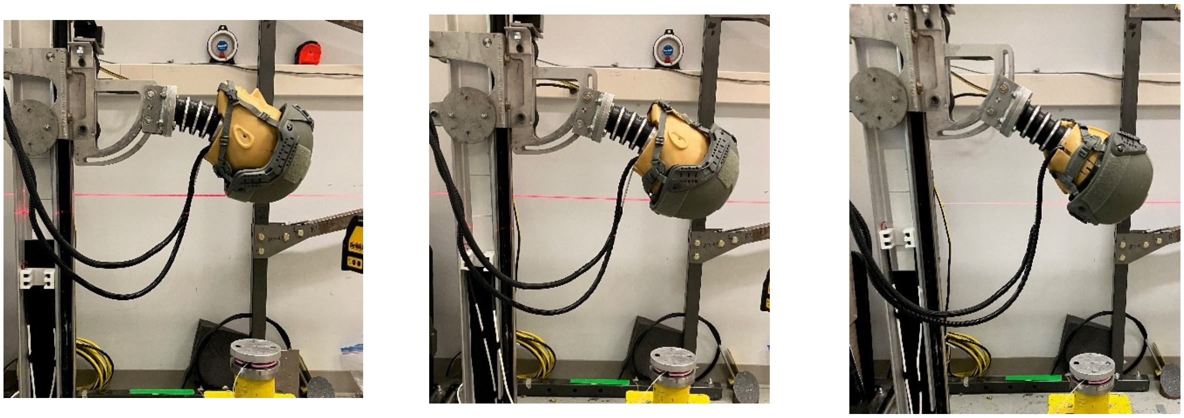

Rear Rear Boss Side

Figure 6-2 Orientations of the Helmeted Impacts

Data was recorded via a velocity gate, DTS sensor and IPP sensors at the same rates and specifications of the pendulum impacts for the pressure tests done previously (Chapter 4). The DTS and pressure sensors both sampled at 25 kHz. Since the impacts are not all frontal impacts, and in order to avoid confusion, the two sensors are now referred to as the sensor close to the impact site and far from the impact site. For example, a rear impact would have the previously called back sensor be the near sensor, while the previously called front sensor is now referred to as the far sensor. In the case of the side and crown impacts, both sensors are characterized as far from the impact site. The full 60 impacts (5 at each velocity) performed were narrowed down and resulted in 12 impacts (one at each velocity) to analyze in the ABAQUS model. This was because the kinematics from impacts under the same conditions were nearly identical; thus the median impact severity for each set of five impacts was chosen to analyze. A summary of the impact speeds and pressures can be seen in Table 6-2.

Table 6-2 Helmeted Impact Matrix

Experiment Name	**Impact Velocity Median [m/s]**	**Impact Velocity Standard Deviation [+/- m/s]**	**Peak g mean [g]**	**Peak g Standard Deviation [+/- g]**
Front Low	1.61	0.006	25.5	1.16
Front High	2.36	0.004	46.2	2.89
Front Boss Low	1.58	0.007	23.2	0.80
Front Boss High	2.34	0.024	39.6	2.98
Crown Low	1.59	0.007	30.5	2.49
Crown High	2.34	0.009	45.3	1.85
Side Low	1.59	0.004	22.0	1.00
Side High	2.31	0.007	42.9	1.62
Rear Low	1.56	0.005	55.3	5.87
Rear High	2.37	0.005	53.5	2.37
Rear Boss Low	1.55	0.010	30.0	1.43
Rear Boss High	2.39	0.023	56.8	4.82

This data was then filtered to 1650 Hz for the linear accelerations and 300 Hz for the rotational velocities as per SAE J211b through a Matlab code and input as a kinematic boundary condition to ABAQUS.[40] One impact from each set was chosen to be run in the model, with a time duration of 30 ms. The 30 ms covers the entire first peak of pressure from the impact and is short enough to not experience the instabilities experienced while running the model for displacement. Since the test was much longer than the first set of pressure data, and the file sizes of results were very large, the sample rate was reduced in half to 12,500 Hz. A sample set of kinematics for a front impact is shown in Figure 6-3

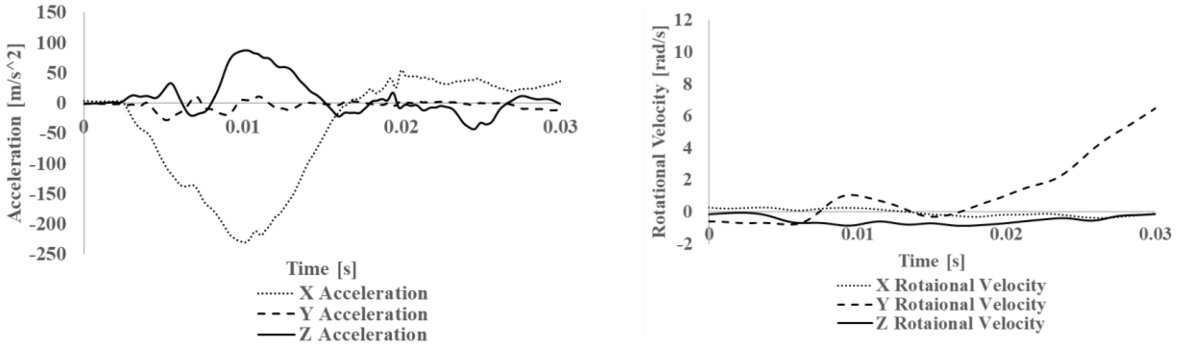

Linear Accelerations

Rotational Velocities

Figure 6-3 Helmeted experiments kinematic input

For the pressure local sensitivity, adjacent elements in each direction from the sensor location were chosen. (Figure 6-4) On average, the distance between elements was 5 mm. Seven elements at both the front and back sensor locations were output from the model.

Displacement was analysed for local sensitivity by selecting the four adjacent nodes to the central node. (Figure 6-4). On average the distance between nodes was 5 mm. Only four of the 18 nodes were selected to analyze the sensitivity: nodes 1, 3, 10, 12. (Figure 5-3) Peak pressures and displacements were compared from each location to the original center sensor element using a simple percent difference calculation.

Pressure Sensitivity Element Configuration

Displacement Sensitivity Nodal Configuration

Figure 6-4 Sensitivity Output Configuration

To determine if the pressure sensors were placed in areas of maximal magnitude, full slices of the brain were analyzed. The slices were extracted at the time of maximal pressure and rotated to be in parallel to the line of impact (rotation of angle β, about the transverse axis of the body). A pressure gradient was then extracted along the plane from the largest to the smallest pressure.

6.3 Results

6.3.1 Sensitivity Analysis Pressure

There were some signs of directionality bias in the results, so results are presented broken down into directional components. This was done as a parallel to the pressure gradient and perpendicular to the pressure gradient. For example, for a frontal impact the parallel direction is the x direction while the perpendicular directions are the y and z directions. Additionally, results were split to account for the differences in sensitivity from sensors close to the impact site, and away from the impact site. For example, a front impact would classify the front sensor as near and the back sensor as away from the impact site.

In order to calculate the percent difference of the elements, the maximum of each time history was compared. The unhelmeted tests returned that the overall sensitivity was 6.0 %. In the front sensor, the percent difference is 7.8 in the direction parallel to impact, while it rises to 16.4 in the rear sensor. The direction perpendicular to the impact has a significantly lower percent difference at 1.2 % in the front sensor and 4.5 % in the rear sensor.

Table 6-3 Unhelmeted Pressure Sensitivity Results

	Front Sensor %		**Rear Sensor %**		
	Parallel to Impact (x)	**Perpendicular to Impact (y,z)**	**Parallel to Impact (x)**	**Perpendicular to Impact (y,z)**	**Total %**
Pressure Sensitivity	7.8	1.2	16.4	4.5	6.0

Similar to the unhelmeted results, the helmeted tests returned an overall sensitivity of 6.4 %. The near sensor gave a percent difference of 8.4 % parallel to the gradient, while a higher percent difference of 15.1 % was observed in the far sensor. Perpendicular to the impact direction, there was a 2.1 % difference in the near sensor and 3.7 % in the far sensor.

Table 6-4 Helmeted Pressure Sensitivity Results

	Near Sensor %		**Far Sensor %**		
	Parallel to Impact	**Perpendicular to Impact**	**Parallel to Impact**	**Perpendicular to Impact**	**Total %**
Pressure Sensitivity	8.4	2.1	15.1	3.7	6.4

A visualisation of this sensitivity can be seen in Figure 6-5 and Figure 6-6. This confirms the results in Table 6-3 that show the sensitivity having a large directional bias in the direction parallel to the pressure gradient. NearIPP stands for the pressure at the near sensor, while N +/- directions show the pressure at one element moved from the front pressure sensor location. Subsequently, the same is occurring for the FarIPP (far sensor) and F +/- directions. The remaining sensitivity plots can be found in the Appendix: Figure A-6, A-7 and A-8

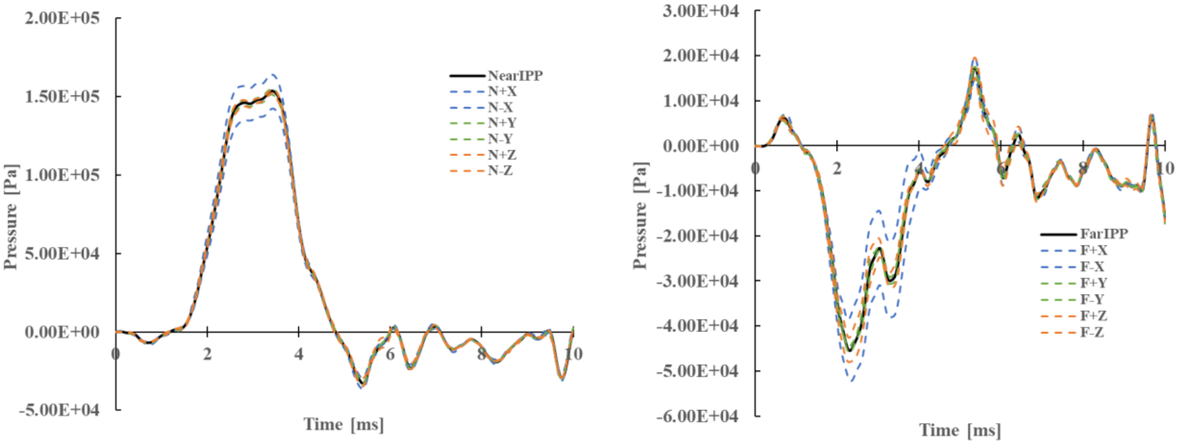

Near Pressure Sensor

Far Pressure Sensor

Figure 6-5 Pressure Sensitivity for the unhelmeted MedT1 impact

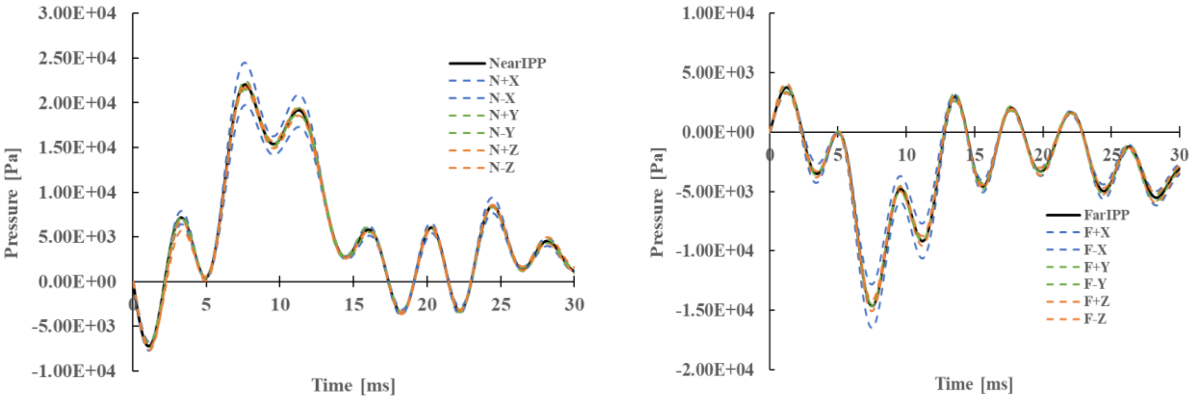

Near Pressure Sensor

Far Pressure Sensor

Figure 6-6 Pressure Sensitivity for the helmeted Front Low impact

6.3.2 Sensitivity Analysis Displacement

All of the impacts (Hit 15 and 27) produced acceptable results for the sensitivity study. After analysis, there seemed to be no directional bias between the different displacement directions. Not only was there no difference between the x and z components of the displacement, but also no difference between moving in either the x or z direction relative to the center. Table 6-5 shows that the overall percent difference between the displacement values was 14.6 %.

Table 6-5 Displacement Sensitivity Results

	X Direction %	Z Direction %	Total %
Displacement Sensitivity	13.3	15.8	14.6

Figure 6-7 shows the sensitivity of the displacement curves with respect to changes in the z and x directions. Point 1 x represents the x component of the displacement, while the +/- x and z represent the nodes in those directions. Point 1 z is the displacement of point 1 in the z direction, while the +/- x and z are the nodes in those directions. The same holds true for points 2 through 4. The results for hit 2 can be found in Figure A-5.

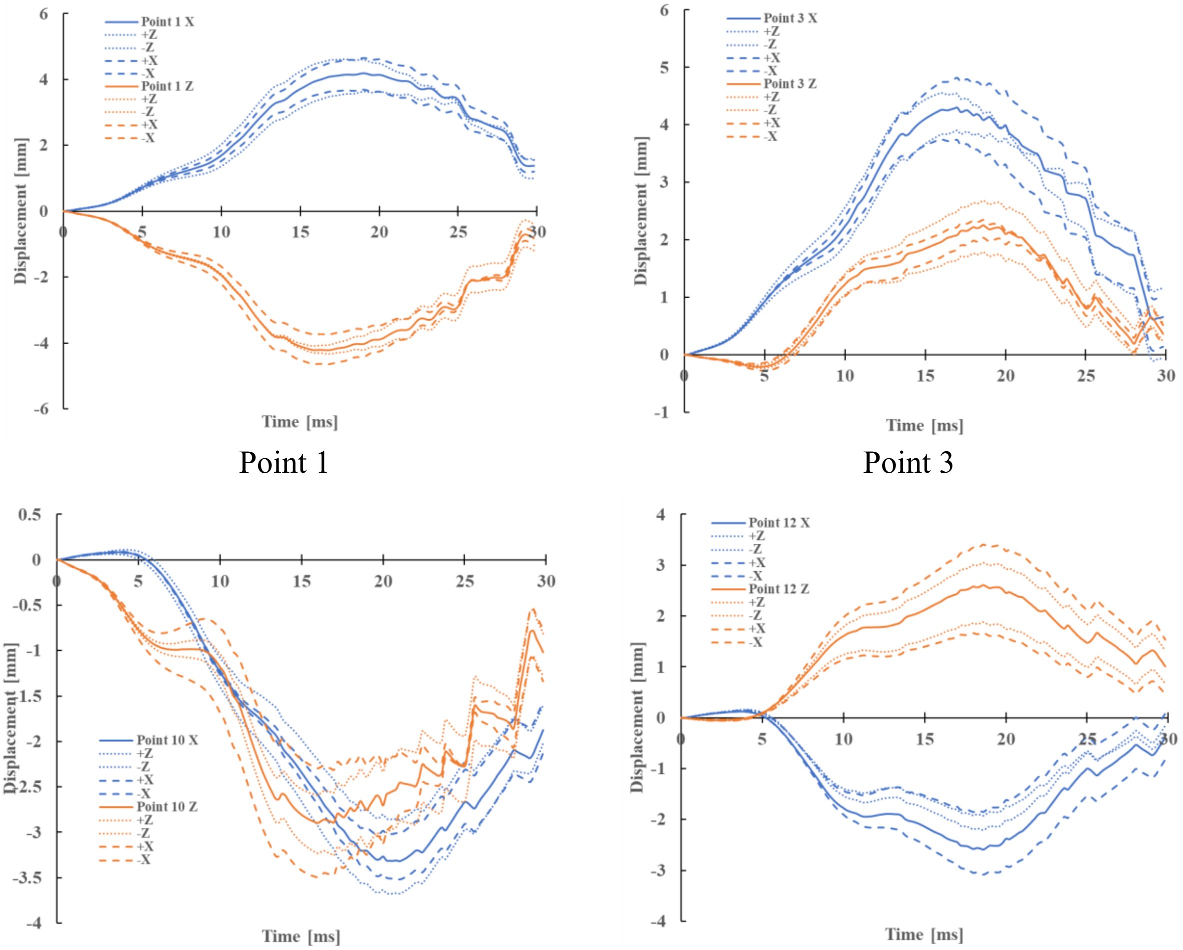

Point 1

Point 3

Point 10

Point 12

Figure 6-7 Displacement Sensitivity for the Hit 1 impact

6.3.3 Sensor Placement

The slices of brain were extracted from ABAQUS and presented in Figure 6-8 and Figure 6-9. A pressure gradient was formed starting with a maximum pressure near the impact site and then an equivalent negative pressure opposite the impact site. These correspond to the coup and contrecoup pressure.

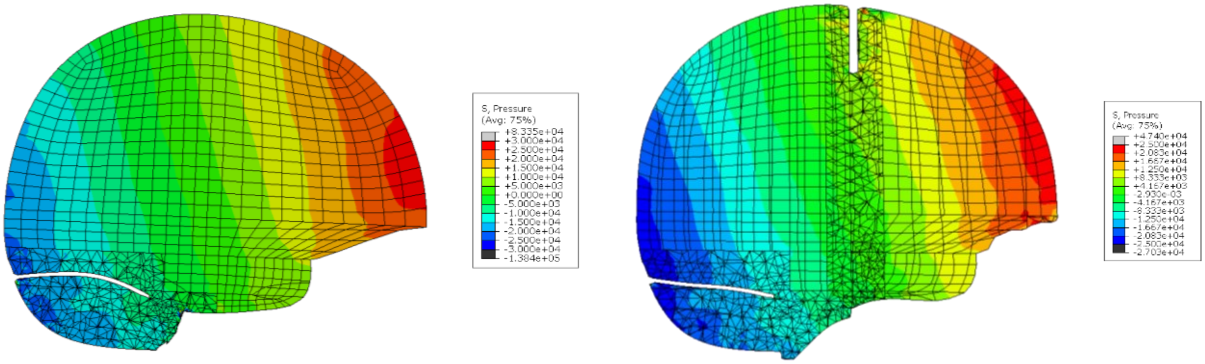

Front Impact

Front Boss Impact

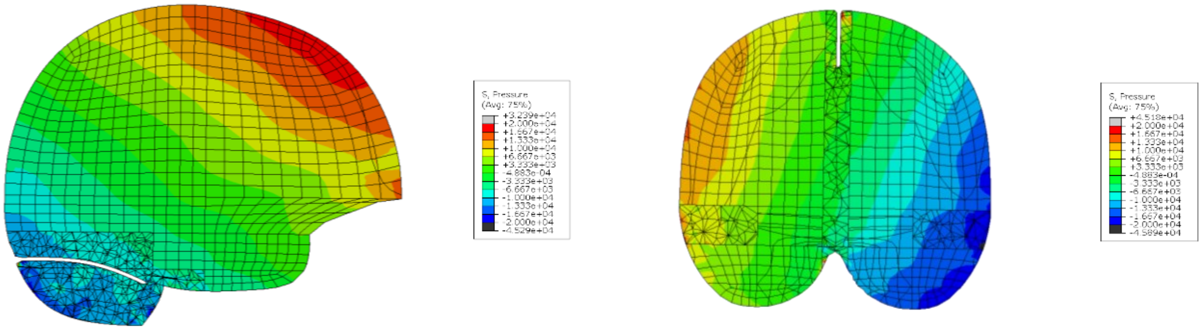

Crown Impact

Side Impact

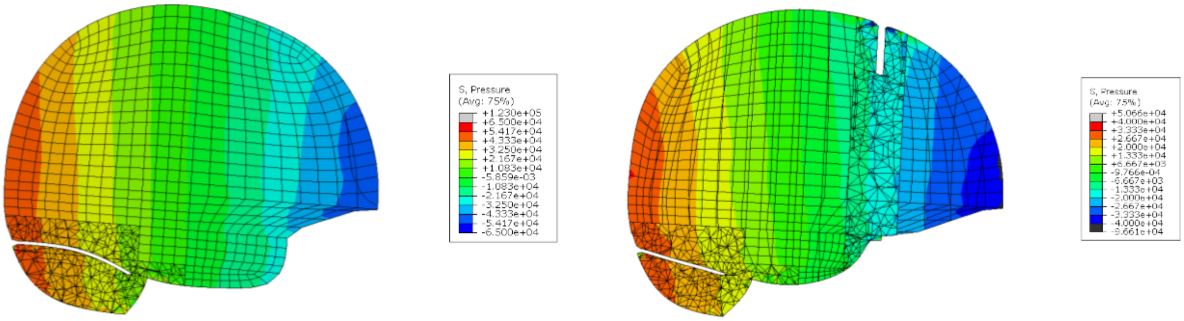

Rear Impact

Rear Boss Impact

Figure 6-8 Pressure from low speed impacts

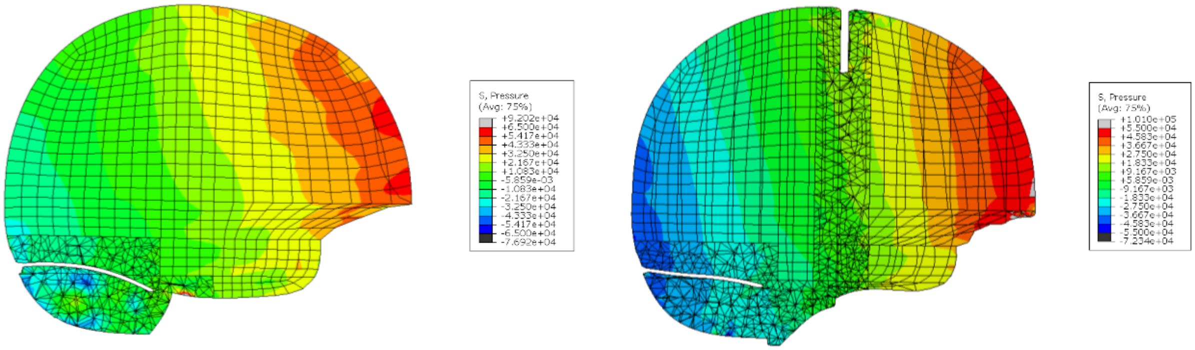

Front Impact　Front Boss Impact

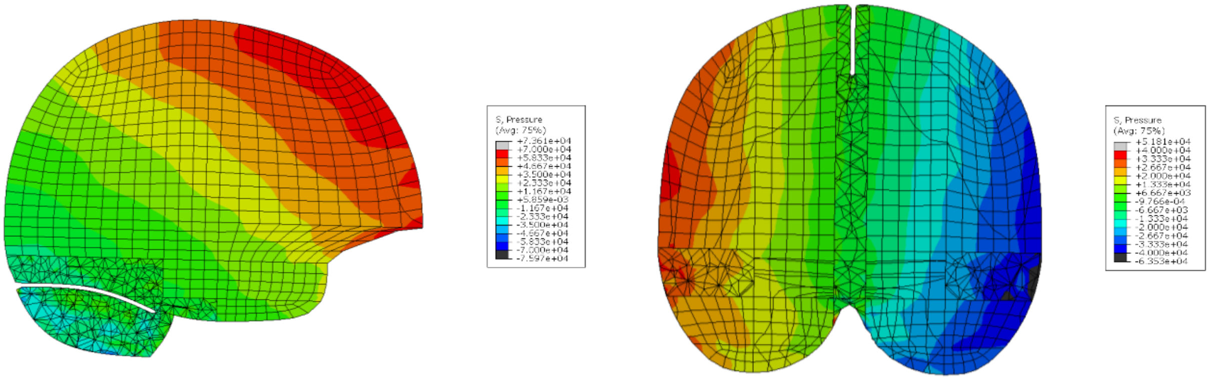

Crown Impact　Side Impact

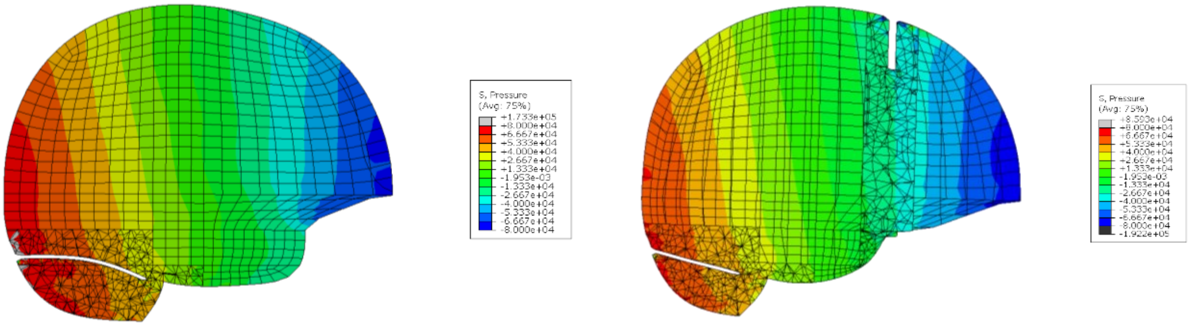

Rear Impact　Rear Boss Impact

Figure 6-9 Pressure from high speed impacts

Along the slice of the brain, the pressures were plotted as a function of distance across the brain. The near and far pressure sensor values were also overlaid to the plots as a visual to indicate how close the sensors were to the maximum. The first and last 12 mm of the pressure gradient were removed to better indicate a practical comparison point. In the physical brain, approximately 12 mm of the outer edges have the gyri and sulci. By removing this area, we are only comparing the maximum and minimums that can be physically recorded in the Sylgard material. The strong linear trend is very apparent in these graphs. (Figure 6-10, Figure 6-11).

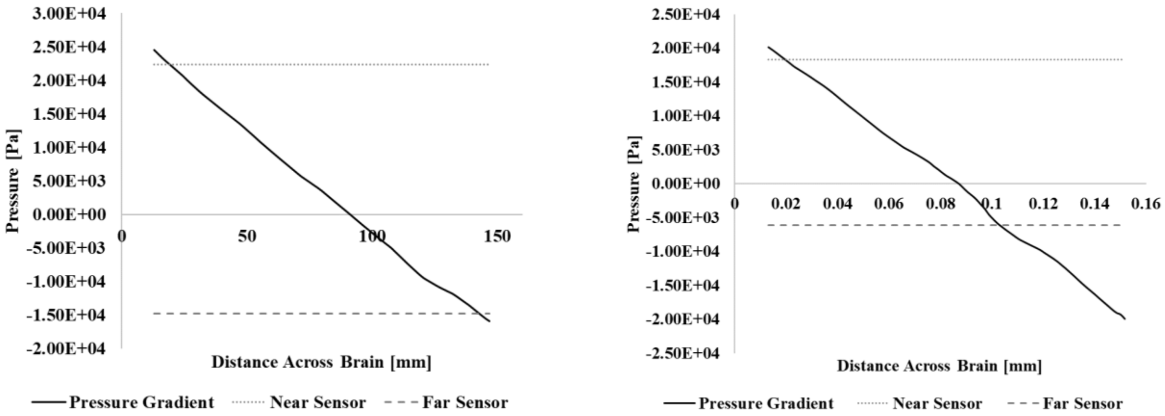

Front Impact Front Boss Impact

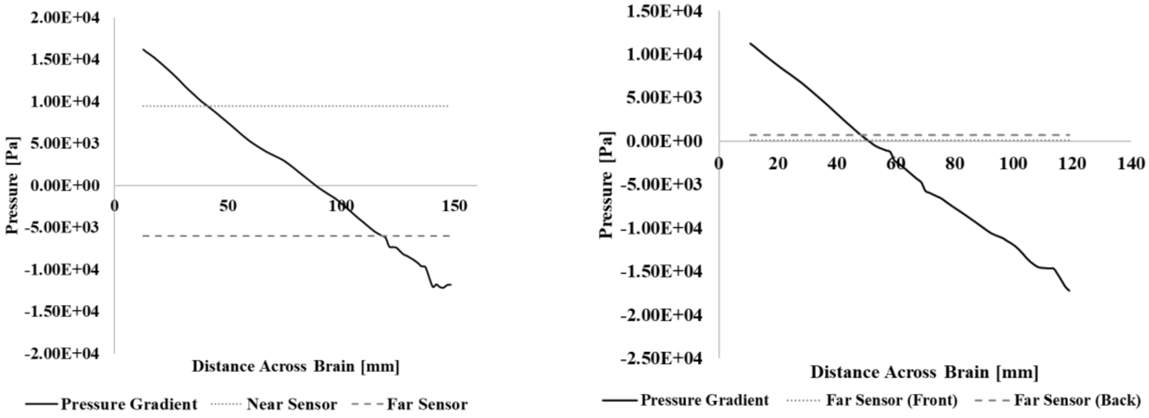

Crown Impact Side Impact

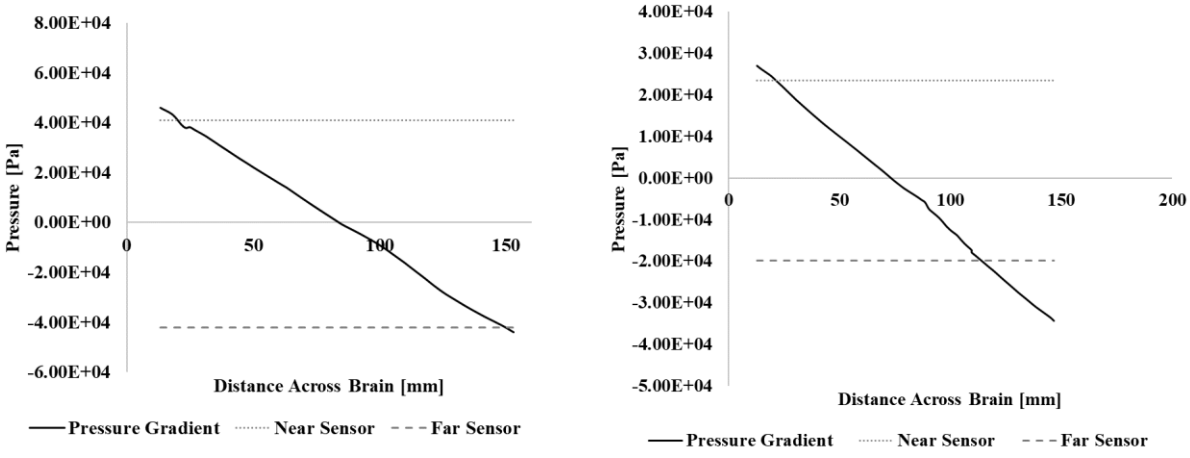

Rear Impact Rear Boss Impact

Figure 6-10 Low speed impact pressure gradient

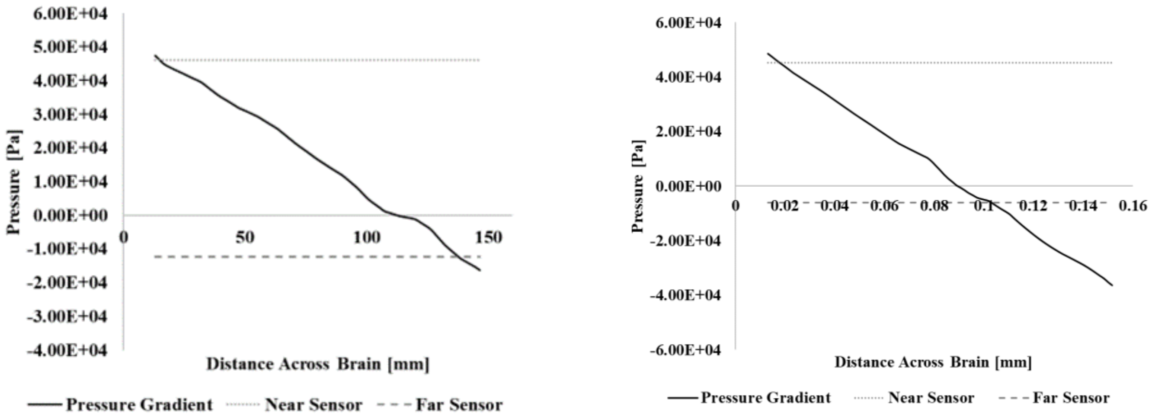

Front Impact

Front Boss Impact

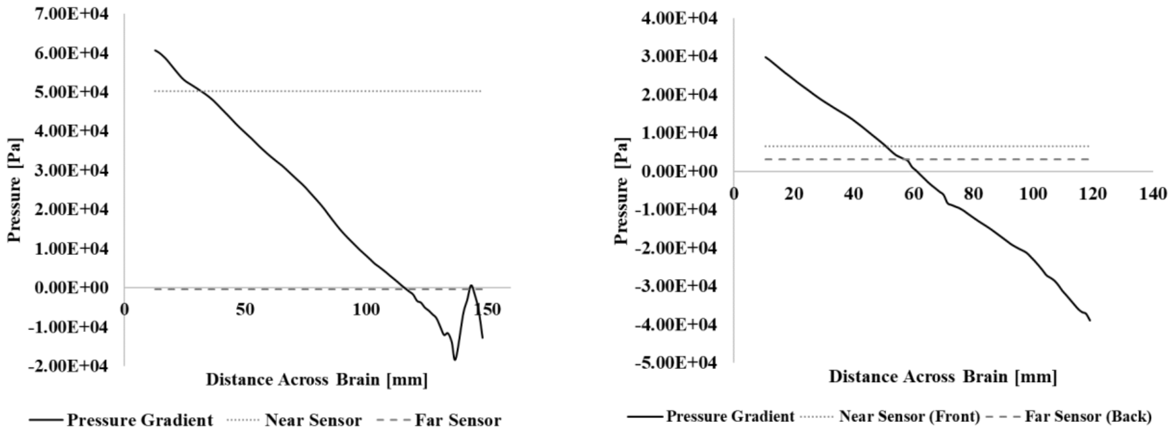

Crown Impact

Side Impact

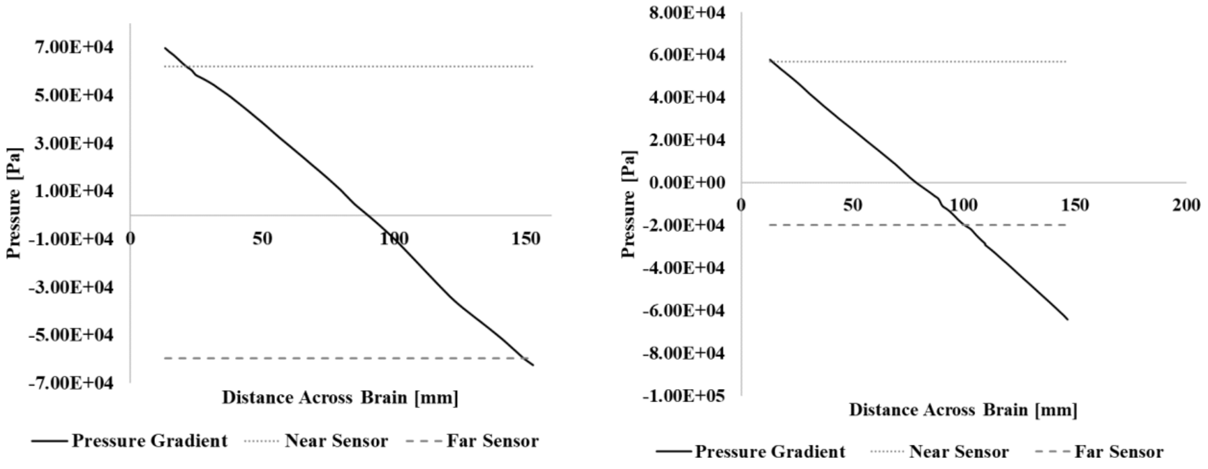

Rear Impact

Rear Boss Impact

Figure 6-11 High speed impact pressure gradient

Table 6-6 Sensor error compared to pressure gradient

Impact	Near Sensor Error [%]	Far Sensor Error [%]
Front Low	6.3	7.2
Front High	0.6	24.5
Front Boss Low	7.2	69.4
Front Boss High	4.6	83.4
Crown Low	40.6	49.1
Crown High	16.9	97.0
Side Low	99.4	104.2
Side High	77.7	107.8
Rear Low	9.3	3.8
Rear High	9.0	4.7
Rear Boss Low	11.1	42.1
Rear Boss High	0.7	33.6

6.4 Discussion

The large discrepancies in the sensitivities between the near and far sensors are in part since the pressure wave is well defined at the impact site. This work is important in defining numerically how sensitive selecting the proper location of the FE model output is. For comparison, parametric studies have analyzed changing material models, and found that these account for anywhere between a 9% to 28% difference in pressure.[10] This disparity depended on parametric studies where values are set to extremum values or selecting differing material models from literature. Our values show that diligence while selecting location of outputs could be just as important as these other factors.

From the pressure gradient results, we can see whether or not the two pressure sensors are capturing the coup and contre-coup pressure values. The results indicate that the front and rear impacts capture both the coup and contre-coup pressure using the two-sensor configuration. Additionally, the front and rear boss impacts would correctly define the coup pressure at the near sensor, but would fail to characterize the pressure at the far sensor location. For the side and crown impacts, the sensor locations did not adequately measure the coup and contre-coup locations. These results were expected and in line with theoretical values. Each gradient followed the linear pattern that held an equal magnitude maximum and minimum on either edge of the brain. Following this theory and the impact directions, it is clear that the two-sensor configuration would only be suitable for impacts that occur along its line of action. Since the two sensors run along a sagittal slice of the brain, the only impacts it can assess both the coup and contre-coup pressures are the impacts that create a gradient along that plane (front and rear impacts).

These two studies on the sensor sensitivity and the overall sensor position show two things. First, precisely knowing the locations of your sensors is important. Not knowing the location and approximating can lead to differences for displacement and pressure that are in line with other significant errors. Secondly, there is an importance to overall sensor location in the sense that you set your sensors to be in line with the impact as close to the edge of the brain as possible. If that is the case, you can approximate the gradient that occurs throughout the entire slice of the brain that the line of impact is occurring on. In the case of the BIPED's two sensors, for front, rear, front boss and rear boss impacts we know the pressure in the entire slice of brain. This information can be used to help determine injury metrics during helmet testing requirements, without the need of a finite element model simulation.

This chapters concludes the objectives set out by the thesis, and specifically the goal of exploring how the pressure sensors react to a helmeted impact study. Numerically, the sensitivity of the sensor output location was determined, as well as a broader study on how the sensor locations represent the coup and contrecoup pressures.

Chapter 7. Conclusions

7.1 Contributions

In this thesis, the primary goal was to develop a digital twin of the BIPED Headform. This model was then used to iterate and improve on the physical model by testing the locations of the pressure sensors. In order to complete this investigation, a partial comparison analysis in pressure and nodal displacement of the finite element model had been undertaken.

First, the model was developed using geometry supplied by the DRDC design molds, and then meshed in a combination of Hypermesh and ABAQUS. Then material properties were determined for the parts by using the properties of the synthetic materials that they were made from. In the case of the Sylgard gel used in the brain, experimental testing was undertaken to determine the hyperelastic and viscoelastic material properties. The fluid was modelled as a solid layer with an equation of state. All of the parts were combined with tie constraints to ensure proper connectivity, and a meshing convergence on the brain was successfully completed.

Two sets of experimental data were used to compare the model and ensure that it resembled the physical surrogate. The first was pressure experiments. These were simulated in the model using experimental kinematic and kinetic boundary condition. Outputs for the model were two sensor locations: a front and back sensor. Pressure time histories were compared to the experimental data using the CORA technique. A second set of experiments was compared. Nodal displacement experiments were simulated in the BIPED using kinematic boundary conditions. X and Z direction nodal displacements were analyzed in the brain at 18 different locations along a parasagittal slice. Again, these results were compared to the physical experimental model using a CORA analysis.

Sensor placement in the model was then analyzed. Output nodes and elements surrounding the real location of interest were compared. A percent difference was then calculated to quantify how sensitive the output parameters are to output location. Additionally, a study into where the pressure sensors are located, a gradient along the impact line was extracted and the sensor values were compared to the maximums and minimums of this gradient.

Overall, the results of the study suggest that the BIPED finite element model can represent the physical headform in impact scenarios:

- Pressure time histories for the two models correlated to a “good” score (front sensor >0.7 , back sensor <0.5) using the CORA rating scheme.
- Displacement time histories for the two models correlated to a “good” score (>0.5) using the CORA rating scheme.
- Six degree of freedom kinematic inputs provide a better correlation than force input as suggested by the rear sensor CORA ratings.
- Output location in FE head models is highly sensitive, as shown by the large percent difference in moving the location of the sensors by five millimeters.
- To adequately represent the coup and contrecoup pressures during an impact, there is need for a sensor close to the impact site and opposite the impact site along the line of action of the impact. This was demonstrated by the pressure gradient plots.

The results indicate that the BIPED finite element model developed can adequately represent the physical surrogate model in pressure and nodal displacement, and that careful sensor placement is necessary to get accurate outputs. This study provides a more complete approach to the comparison to experimental data in both pressure and nodal displacement. This was achieved by having confidence in the geometry between the simulation and experiment, and therefore selecting proper output locations for the model. Also, this study compared the entire time series data and not only peak values. These improvements to the experimental comparison process allows this study to have confidence in the pressure and nodal displacement results.

7.2 Future Work and Recommendations

After completion of this work, efforts to improve fidelity to the physical surrogate can be undertaken. Most of this effort should surround the modelling of the CSF layer. The method used in this thesis is highly dependent on mesh qualities such as resistance to shear locking. Ideally, a multi physics approach should be undertaken so that the fluid is modelled more accurately. This could allow the water to be modelled as a material that does not carry shear forces. A lack of shear forces would allow the brain to rotate freely within the skull, as the edges of the brain would be less constrained. Along these same lines, a multiphysics approach would allow for the brain to include the gyri and sulci on its surface without the worry of an unstable mesh in the fluid layer. In order to develop the fluid layer, it would be ideal to start with a simplified model where element stability and meshing has less of an effect on the useability. This way a pure analysis of the differences on modelling approaches can be done. Overall, this can lead to a more bio-fidelic finite element model.

Another useful development to the model would be analyzing the effect of short duration impact on sensor placement. This study was limited to long duration impacts (above 3 ms). Short duration impacts are seldom studied and can have properties similar to blast wave impacts. In terms of sensor placement, this would change the locations of the maximum pressures throughout the experiment instead of just having a reliable coup and contrecoup location. By analyzing the sensor placement during short duration impacts, the BIPED headform could then be used for ballistics testing in the future.

The BIPED finite element model has countless other uses, as it aids in the iterative design process. From material properties to part geometries, tests can be first done in simulation before spending the money to manufacture and experimentally test. Overall, this model provides insight into the intricacies of the physical surrogate model which is the BIPED.

References

[1] J. A. Langlois, W. Rutland-Brown, and M. M. Wald, “The Epidemiology and Impact of Traumatic Brain Injury: A Brief Overview,” *J. Head Trauma Rehabil.*, vol. 21, no. 5, pp. 375–378, Oct. 2006.

[2] Canadian Institute for Health Information, “Head injuries in Canada : a decade of change (1994-1995 to 2003-2004) / Issued jointly by Statistics Canada.” Ottawa - Ontario : Canadian Institute for Health Information August 2006, Apr. 03, 2013. [Online]. Available: publications.gc.ca/pub?id=9.573803&sl=0

[3] C. A. Taylor, “Traumatic Brain Injury–Related Emergency Department Visits, Hospitalizations, and Deaths — United States, 2007 and 2013,” *MMWR Surveill. Summ.*, vol. 66, 2017, doi: 10.15585/mmwr.ss6609a1.

[4] D. C. Thompson, F. P. Rivara, and R. S. Thompson, “Effectiveness of Bicycle Safety Helmets in Preventing Head Injuries: A Case-Control Study,” *JAMA*, vol. 276, no. 24, pp. 1968–1973, Dec. 1996, doi: 10.1001/jama.1996.03540240046029.

[5] D. Marjoux, D. Baumgartner, C. Deck, and R. Willinger, “Head injury prediction capability of the HIC, HIP, SIMon and ULP criteria,” *Accid. Anal. Prev.*, vol. 40, no. 3, pp. 1135–1148, Dec. 2007.

[6] C. Ward, M. Chan, and A. Nahum, “Intracranial Pressure — A Brain Injury Criterion,” *SAE Trans.*, vol. 89, pp. 3867–3880, 1980.

[7] S. Ouellet, A. Bouamoul, R. Gauvin, J. S. Binette, K. V. Williams, and L. Martineau, “Development of a biofidelic head surrogate for blast-induced traumatic brain injury assessment,” in *Proceedings of the Personal Armor System Symposium*, 2012.

[8] Y. Li, S. Ouellet, A. H. Vette, D. Raboud, A. Martin, and C. R. Dennison, “Evaluation of the Kinematic Biofidelity and Inter-Test Repeatability of Global Accelerations and Brain Parenchyma Pressure for a Head–Brain Physical Model,” *J. Biomech. Eng.*, vol. 143, no. 9, p. 091006, Sep. 2021, doi: 10.1115/1.4050752.

[9] A. Nahum, R. Smith, and C. Ward, “Intracranial Pressure Dynamics During Head Impact,” *SAE Tech. Pap. 770922*, 1977, Accessed: Feb. 09, 2016. [Online]. Available: http://papers.sae.org/770922/

[10] T. J. Horgan and M. D. Gilchrist, “Influence of FE model variability in predicting brain motion and intracranial pressure changes in head impact simulations,” *Int. J. Crashworthiness*, vol. 9, no. 4, pp. 401–418, Aug. 2004, doi: 10.1533/ijcr.2004.0299.

[11] B. Song, M. M. de Oliveira, S. Wang, Y. Li, P. Wen, and T. Ahfock, “A Preliminary Study of the Impact of Lateral Head Orientations on the Current Distributions During tDCS,” in *Brain Informatics*, P. Liang, V. Goel, and C. Shan, Eds., in Lecture Notes in Computer Science. Cham: Springer International Publishing, 2019, pp. 254–264. doi: 10.1007/978-3-030-37078-7_25.

[12] “CDC - TBI in the US Report - Traumatic Brain Injury - Injury Center.” http://www.cdc.gov/TraumaticBrainInjury/tbi_ed.html (accessed Mar. 08, 2014).

[13] C. W. Pearce and P. G. Young, “On the Pressure Response in the Brain due to Short Duration Blunt Impacts,” *PLOS ONE*, vol. 9, no. 12, p. e114292, Dec. 2014, doi: 10.1371/journal.pone.0114292.

[14] G. McLatchie, “J. TORG ‘Athletic injuries of the head, neck and face,’” *Br. J. Sports Med.*, vol. 16, no. 3, pp. 191–191, Sep. 1982, doi: 10.1136/bjsm.16.3.191.

[15] A. C. MCKEE and D. H. DANESHVAR, “The neuropathology of traumatic brain injury,” *Handb. Clin. Neurol.*, vol. 127, pp. 45–66, 2015, doi: 10.1016/B978-0-444-52892-6.00004-0.

[16] B. J. McEntire and P. Whitley, “Blunt Impact Performance Characteristics of the Advanced Combat Helmet and the Paratrooper and Infantry Personnel Armor System for Ground Troops Helmet.” U.S. Army Aeromedical Research Laboratory, Aug. 2005.

[17] R. Eppinger *et al.*, “Development of improved injury criteria for the assessment of advanced automotive restraint systems - II.” National Highway Traffic Safety Administration, 1999.

[18] E. G. Takhounts, M. J. Craig, K. Moorhouse, J. McFadden, and V. Hasija, “Development of Brain Injury Criteria (BrIC),” *Stapp Car Crash J.*, vol. 57, pp. 243–266, 2013.

[19] W. N. Hardy, C. D. Foster, M. J. Mason, K. H. Yang, A. I. King, and S. Tashman, “Investigation of head injury mechanisms using neutral density technology and high-speed biplanar x-ray,” *Stapp Car Crash J.*, vol. 45, 2001, Accessed: Feb. 09, 2016. [Online]. Available: http://wbldb.lievers.net/10022186.html

[20] E. G. Takhounts, R. H. Eppinger, J. Q. Campbell, R. E. Tannous, E. D. Power, and L. S. Shook, “On the Development of the SIMon Finite Element Head Model,” *Stapp Car Crash J.*, vol. 47, pp. 107–133, 2003.

[21] H. Mao *et al.*, “Development of a Finite Element Human Head Model Partially Validated with Thirty Five Experimental Cases,” *J. Biomech. Eng.*, vol. 135, no. 11, 2013.

[22] F. A. O. Fernandes, D. Tchepel, R. J. Alves de Sousa, and M. Ptak, “Development and validation of a new finite element human head model: Yet another head model (YEAHM),” *Eng. Comput.*, vol. 35, no. 1, pp. 477–496, Mar. 2018, doi: 10.1108/EC-09-2016-0321.

[23] T. J. Horgan and M. D. Gilchrist, “The creation of three-dimensional finite element models for simulating head impact biomechanics,” *Int. J. Crashworthiness*, vol. 8, no. 4, pp. 353–366, Jan. 2003, doi: 10.1533/ijcr.2003.0243.

[24] G. Martin, “Traumatic brain injury: The first 15 milliseconds,” *Brain Inj.*, vol. 30, no. 13–14, pp. 1517–1524, Dec. 2016, doi: 10.1080/02699052.2016.1192683.

[25] X. Trosseille, C. Tarriére, F. Lavaste, F. Guillon, and A. Domont, “Development of a F.E.M. of the Human Head According to a Specific Test Protocol,” presented at the Stapp Car Crash Conference, Nov. 1992, p. 922527. doi: 10.4271/922527.

[26] P. G. Young, “Intracranial pressure transients caused by head impacts,” *Int. Res. Counc. Biomech. Impact IRCOBI Conf. Proc.*, 1998.

[27] D. Downes, A. Bouamoul, S. Ouellet, and M. Nejad Ensan, “Development and validation of a biofidelic head form model to assess blast-induced traumatic brain injury,” *J. Def. Model. Simul. Appl. Methodol. Technol.*, vol. 15, no. 3, pp. 257–267, Jul. 2018, doi: 10.1177/1548512917737634.

[28] J. Rovt, S. Xu, S. Ouellet, and O. E. Petel, “A technique for in situ intracranial strain measurement within a deformable headform,” *J. Mech. Behav. Biomed. Mater.*.

[29] “Aisi 304 Stainless Steel.” MakeItFrom, 2020. [Online]. Available: https://www.makeitfrom.com/material-properties/AISI-304-S30400-Stainless-Steel

[30] ASM International, Ed., *ASM handbook*, 10th edition. Materials Park, Ohio: ASM International, 1990.

[31] E. Sun, “Shear locking and hourglassing in MSC Nastran, ABAQUS, and ANSYS.” Msc software users meeting, 2006.

[32] "Abaqus 6.13 Online Documentation: Impact of a water-filled bottle." Dassault Systèmes, 2013.

[33] R. W. Ogden, G. Saccomandi, and I. Sgura, "Fitting hyperelastic models to experimental data," *Comput. Mech.*, vol. 34, no. 6, pp. 484–502, Nov. 2004, doi: 10.1007/s00466-004-0593-y.

[34] J. E. L. Pacheco, C. A. Bavastri, and J. T. Pereira, "Viscoelastic Relaxation Modulus Characterization Using Prony Series," *Lat. Am. J. Solids Struct.*, vol. 12, pp. 420–445, Apr. 2015, doi: 10.1590/1679-78251412.

[35] D. Singh, S. Boakye-Yiadom, and D. S. Cronin, "Comparison of porcine brain mechanical properties to potential tissue simulant materials in quasi-static and sinusoidal compression," *J. Biomech.*, vol. 92, pp. 84–91, Jul. 2019, doi: 10.1016/j.jbiomech.2019.05.033.

[36] M. Hosseini-Farid, M. Amiri-Tehrani-Zadeh, M. Ramzanpour, M. Ziejewski, and G. Karami, "The Strain Rates in the Brain, Brainstem, Dura, and Skull under Dynamic Loadings," *Math. Comput. Appl.*, vol. 25, no. 2, Art. no. 2, Jun. 2020, doi: 10.3390/mca25020021.

[37] H. Mao *et al.*, "Development of a Finite Element Human Head Model Partially Validated With Thirty Five Experimental Cases," *J. Biomech. Eng.*, vol. 135, no. 11, p. 111002, Nov. 2013, doi: 10.1115/1.4025101.

[38] A. Martin, "Evaluation of the biofidelity of an internally pressurized novel surrogate headform using kinematic and pressure responses to blunt impacts," University of Alberta, 2023.

[39] A. M. Nahum and R. W. Smith, "An Experimental Model for Closed Head Impact Injury," presented at the 20th Stapp Car Crash Conference (1976), Feb. 1976, p. 760825. doi: 10.4271/760825.

[40] SAE International, "SURFACE VEHICLE RECOMMENDED PRACTICE." Mar. 2014.

[41] E. Hwang, J. Hu, and M. P. Reed, "Validating diverse human body models against side impact tests with post-mortem human subjects," *J. Biomech.*, vol. 98, p. 109444, Jan. 2020, doi: 10.1016/j.jbiomech.2019.109444.

[42] C. Gehre and S. Stahlschmidt, "Assessment of Dummy Models by Using Objective Rating Methods," presented at the 22nd International Technical Conference on the Enhanced Safety of Vehicles (ESV)National Highway Traffic Safety Administration, 2011. Accessed: Aug. 24, 2022. [Online]. Available: https://trid.trb.org/view/1365453

[43] D. L. Albert, “Variations in User Implementation of the CORA Rating Metric,” SAE International, Warrendale, PA, SAE Technical Paper 2020-22–0001, Apr. 2021. doi: 10.4271/2020-22-0001.

[44] S. Dutrisac, M. Brannen, T. B. Hoshizaki, H. Frei, and O. E. Petel, “A Parametric Analysis of Embedded Tissue Marker Properties and Their Effect on the Accuracy of Displacement Measurements,” *J. Biomech. Eng.*, vol. 143, no. 11, Jul. 2021, doi: 10.1115/1.4051527.

[45] J. Blaber, B. Adair, and A. Antoniou, “Ncorr: Open-Source 2D Digital Image Correlation Matlab Software,” *Exp. Mech.*, vol. 55, no. 6, pp. 1105–1122, Jul. 2015, doi: 10.1007/s11340-015-0009-1.

[46] J. Rovt, S. Xu, O. E. Petel, S. Ouellet, and S. Dutrisac, “Intracranial strain measurements within a polymeric head surrogate,” *IRCOBI Conf.*, 2021.

[47] H. Y. Yu, B. M. Knowles, and C. R. Dennison, “A Test Bed to Examine Helmet Fit and Retention and Biomechanical Measures of Head and Neck Injury in Simulated Impact,” *JoVE J. Vis. Exp.*, no. 127, pp. e56288–e56288, Sep. 2017, doi: 10.3791/56288.

Appendix

This appendix contains the additional plots and figures that go in accordance with the thesis. Included are the pressure time histories for the validation, displacement time histories, and sensitivity plots for all impacts.

Pressure Validation Results for all impacts

Figure A-1 outlines all of the pressure time histories of the force input tests, while A-2 has all of the kinematic input pressure time histories. Both also are compared to the experimental results.

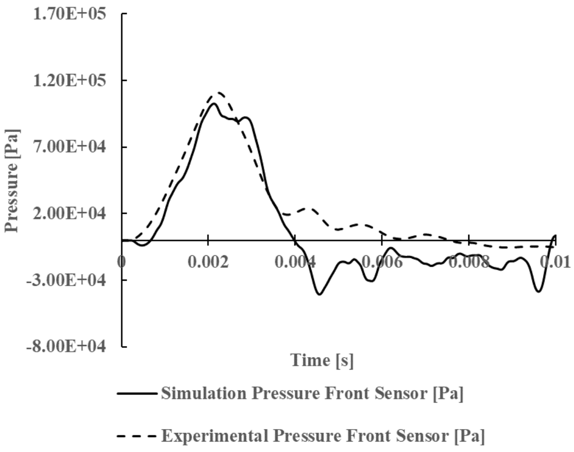

LowT0 FICP

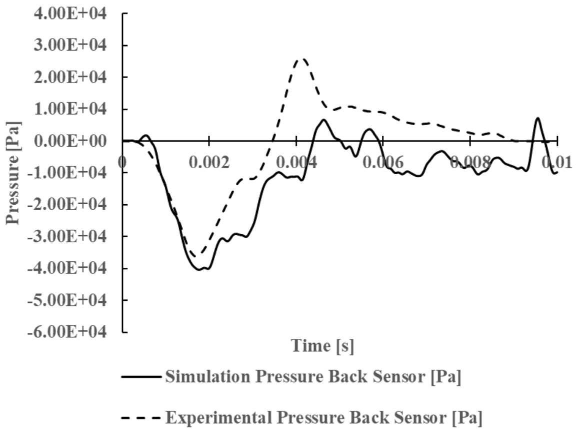

LowT0 BICP

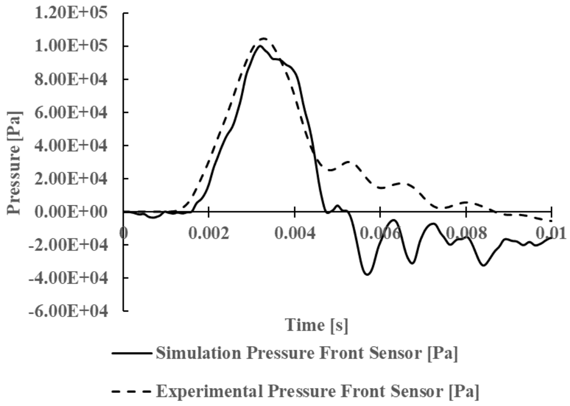

LowT1 FICP

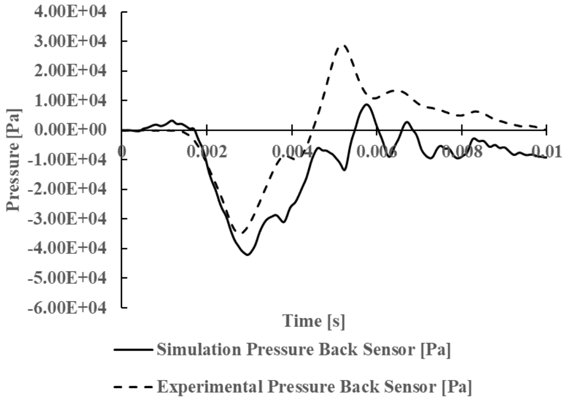

LowT1 BICP

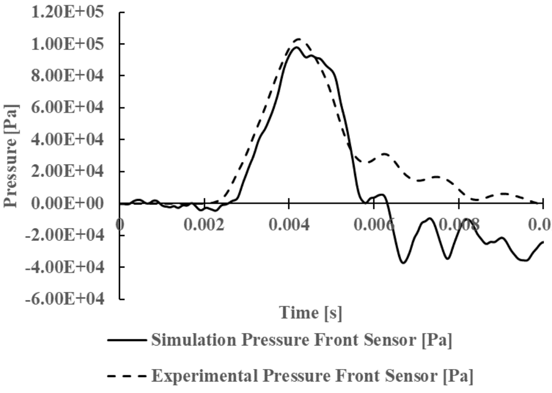

LowT2 FICP

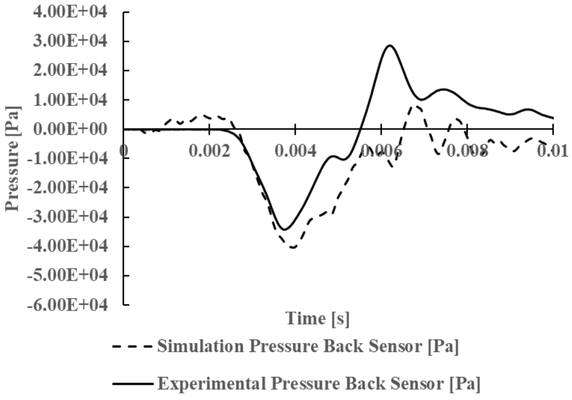

LowT2 BICP

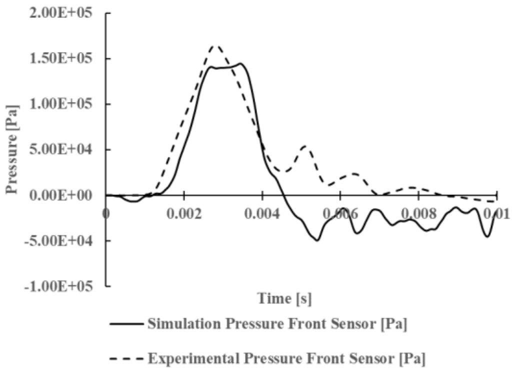

MedT1 FICP

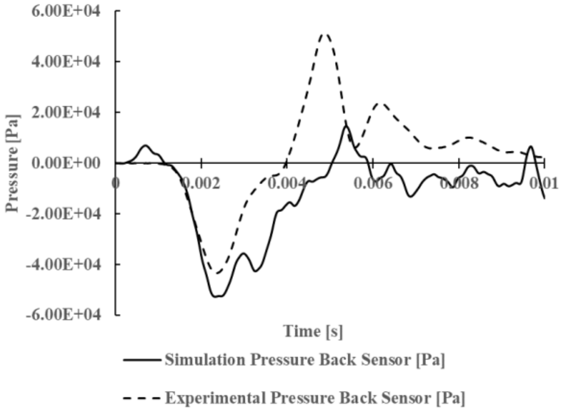

MedT1 BICP

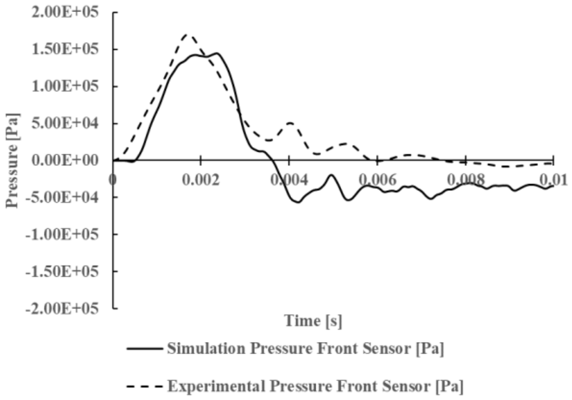

MedT2 FICP

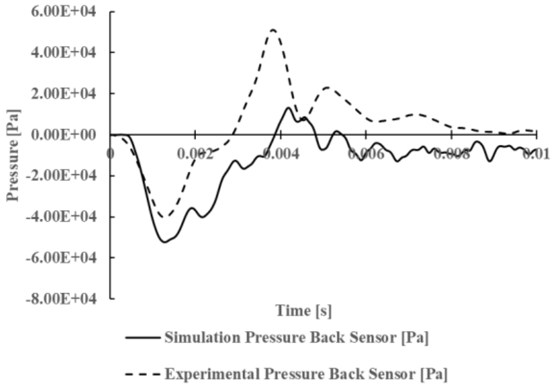

MedT2 BICP

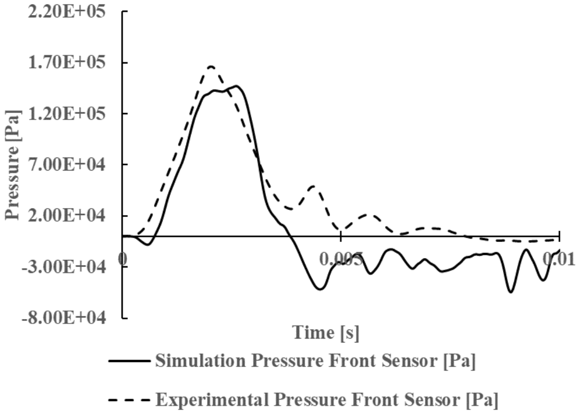

MedT3 FICP

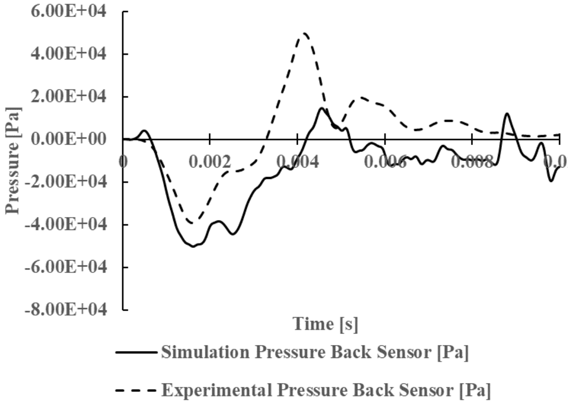

MedT3 BICP

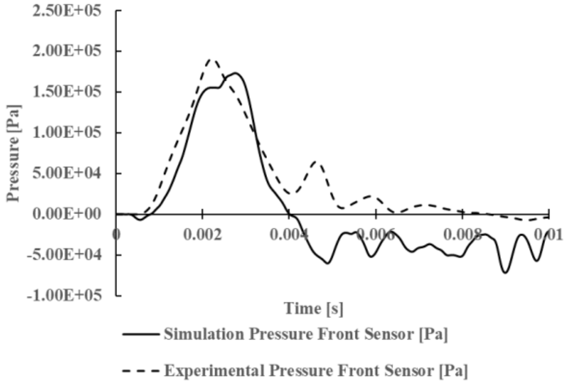

HighT0 FICP

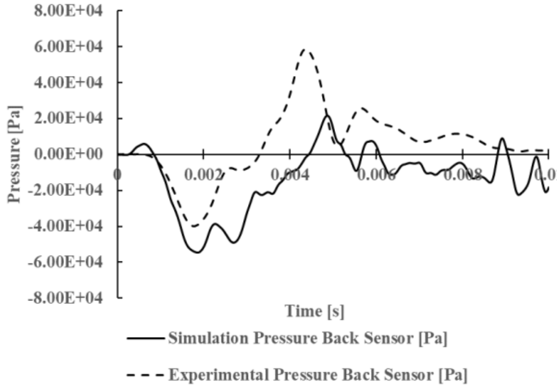

HighT0 BICP

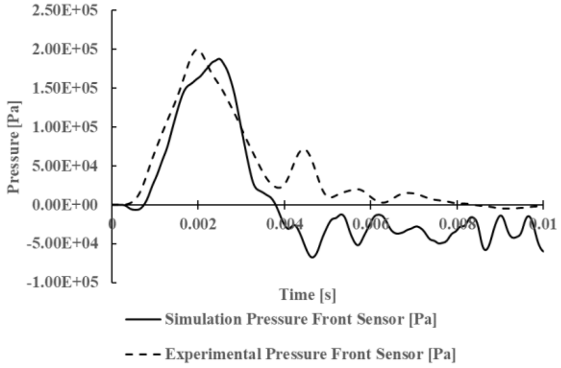

HighT1 FICP

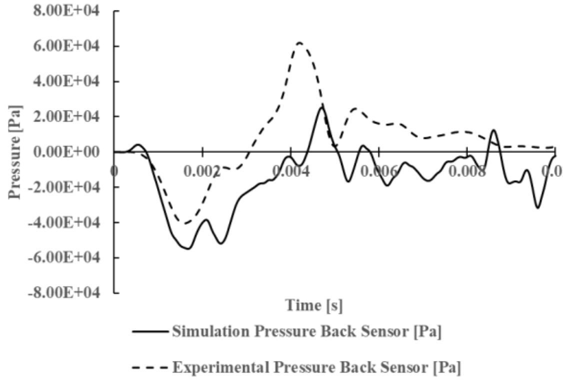

HighT1 BICP

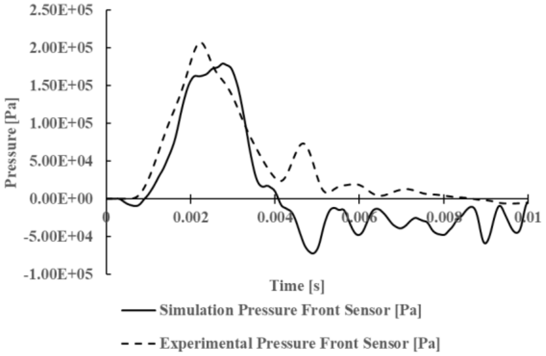

HighT3 FCIP

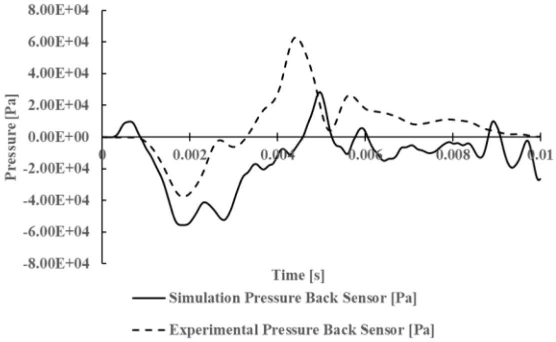

HighT3 BICP

Figure A-1 Pressure time histories for all impacts force input

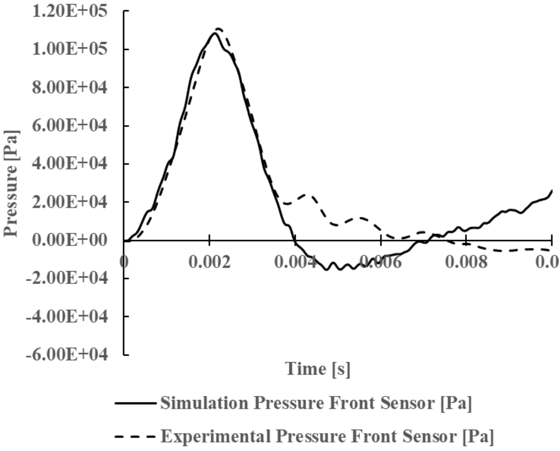

LowT0 FICP

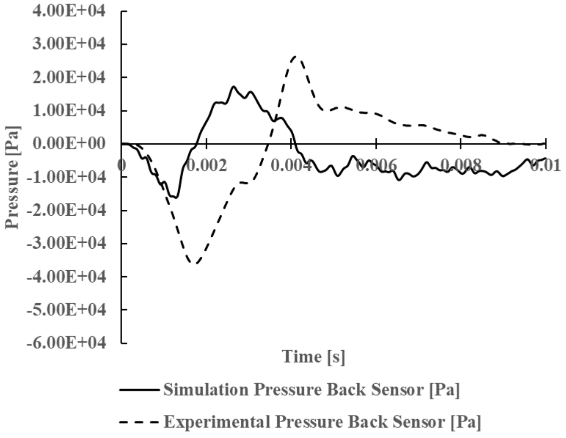

LowT0 BICP

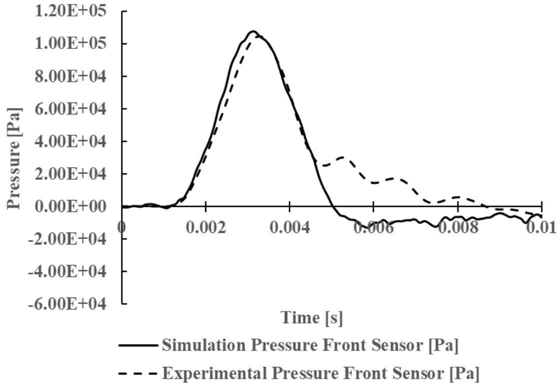

LowT1 FICP

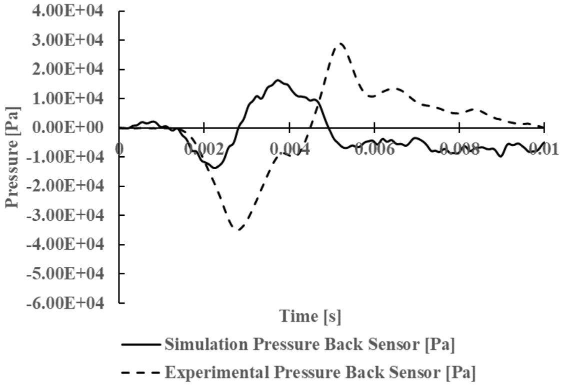

LowT1 BICP

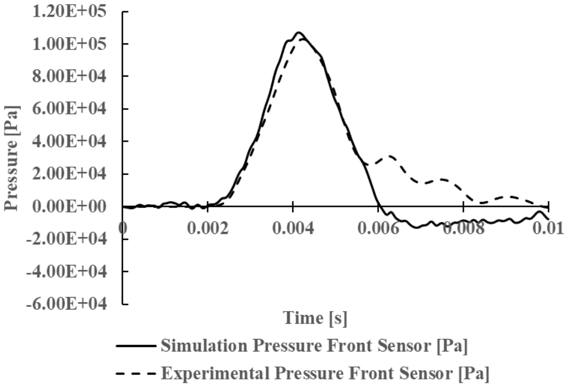

LowT2 FICP

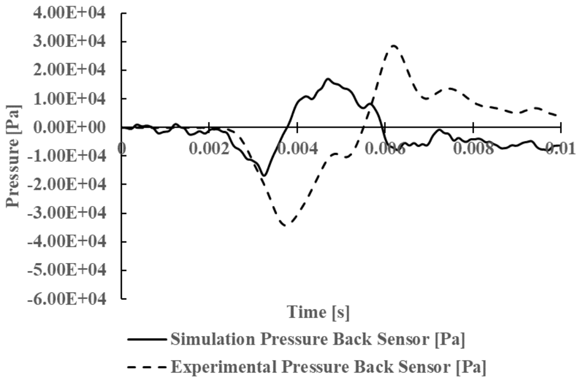

LowT2 BICP

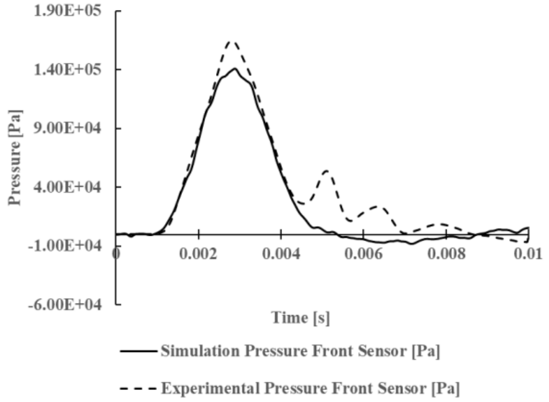

MedT1 FICP

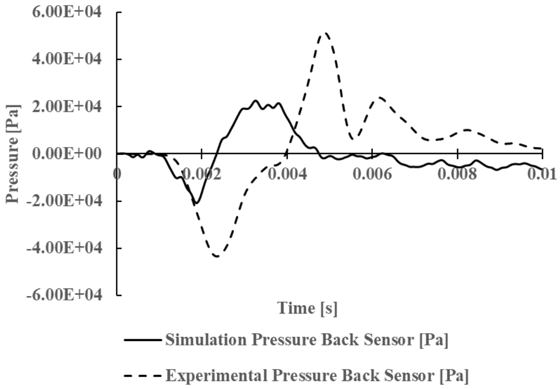

MedT1 BICP

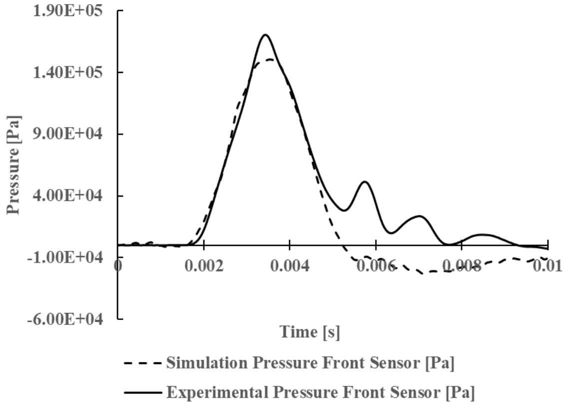

MedT2 FICP

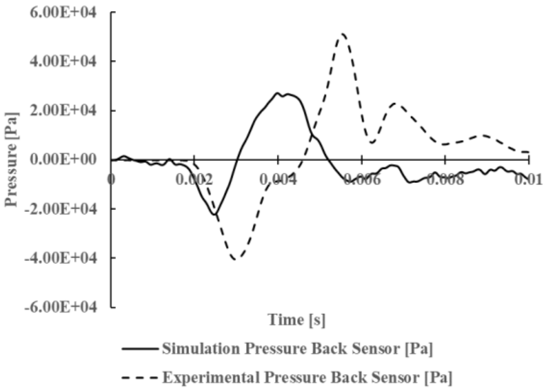

MedT2 BICP

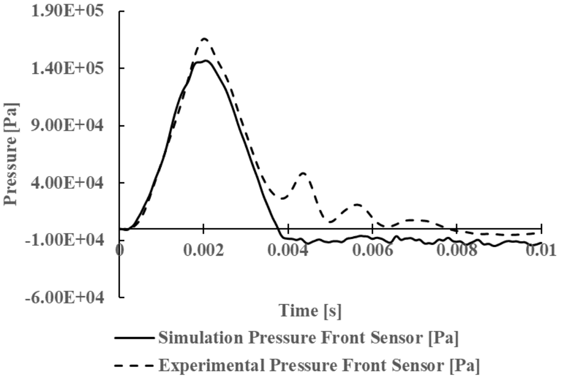

MedT3 FICP

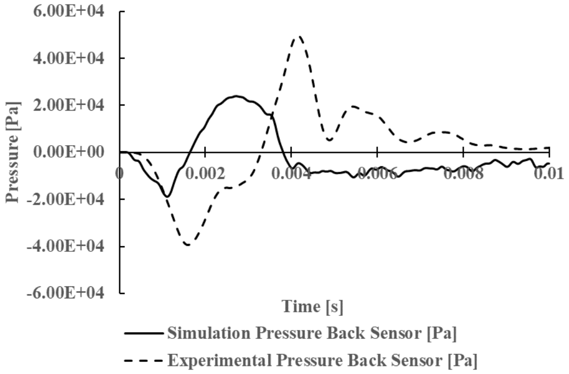

MedT3 BICP

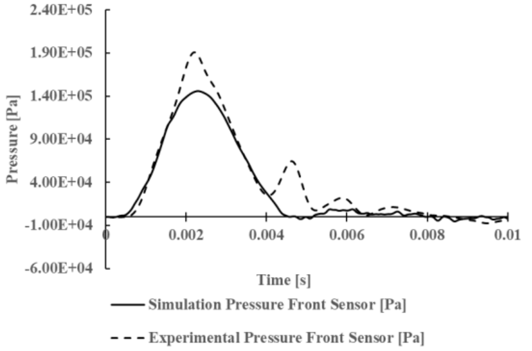

HighT0 FICP

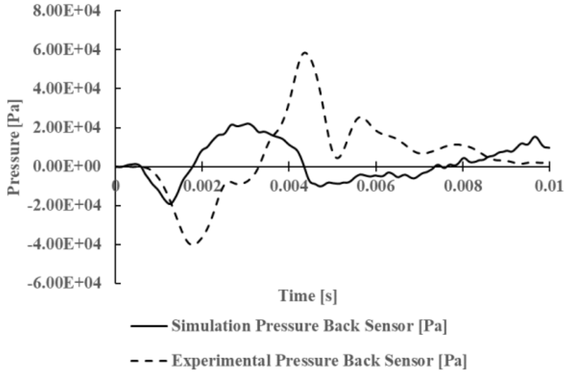

HighT0 BICP

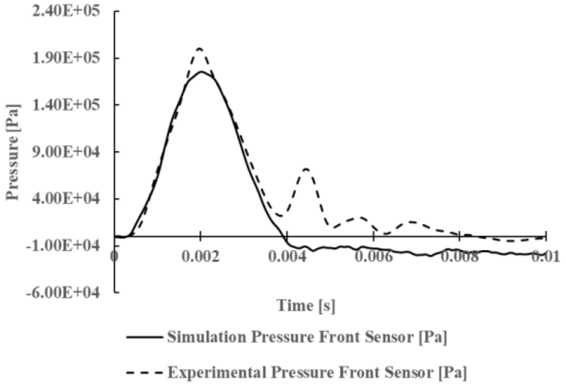

HighT1 FICP

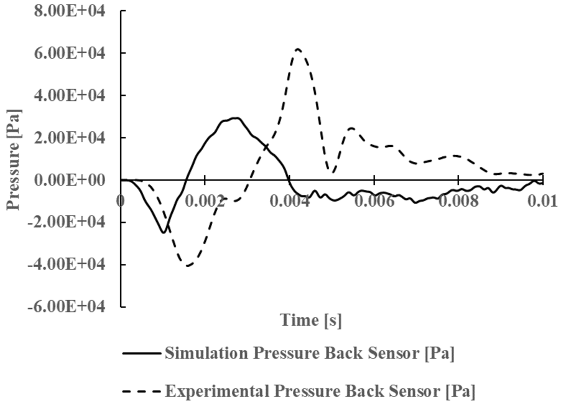

HighT1 BICP

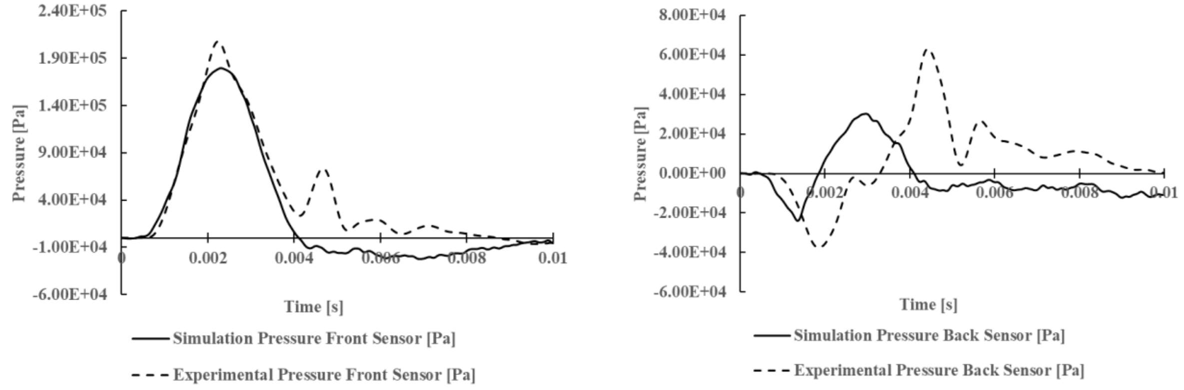

HighT3 FCIP HighT3 BICP

Figure A-2 Pressure time histories for all impacts kinematic input

Displacement results for all impacts

Displacement time histories for Hit 1 are shown in Figure A-3, while time histories for Hit 2 are shown in Figure A-4.

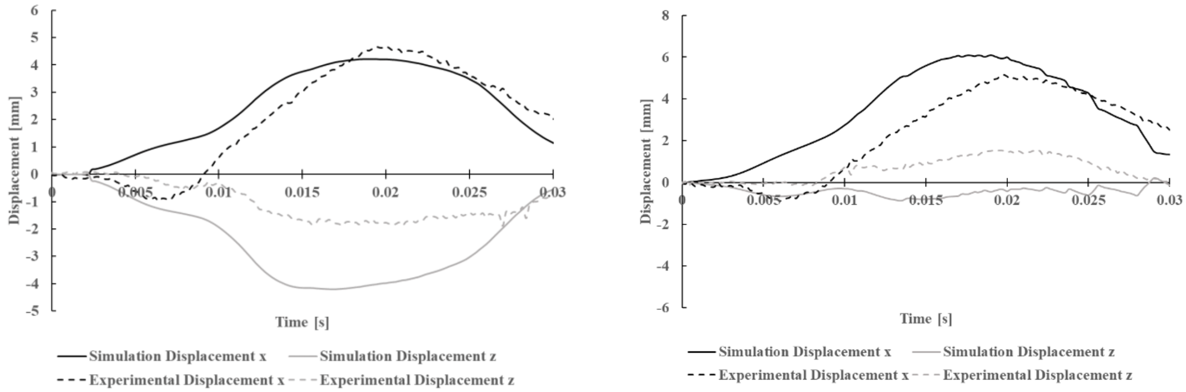

Point 1 Point 2

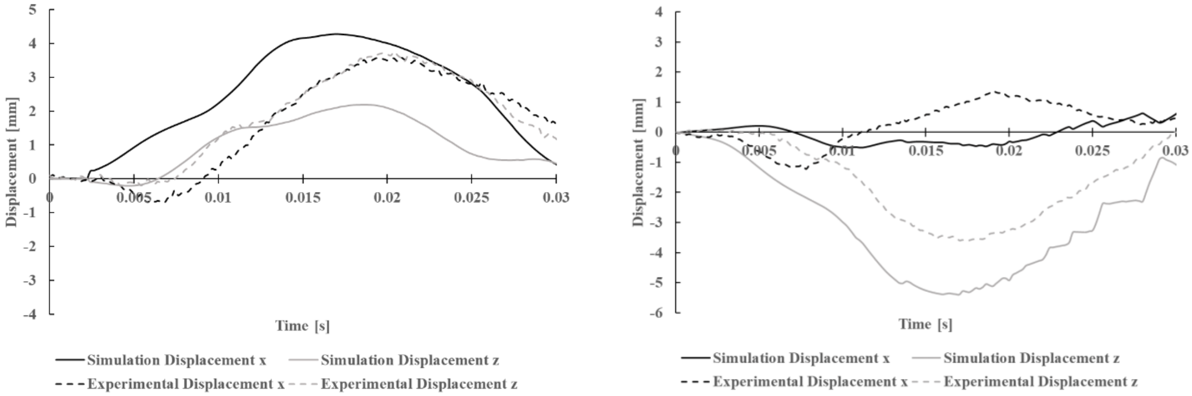

Point 3 Point 4

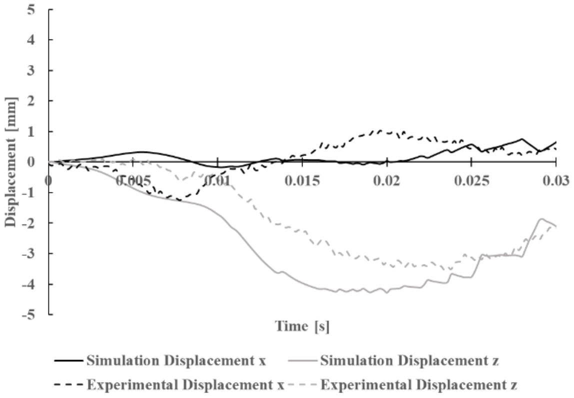

Point 5

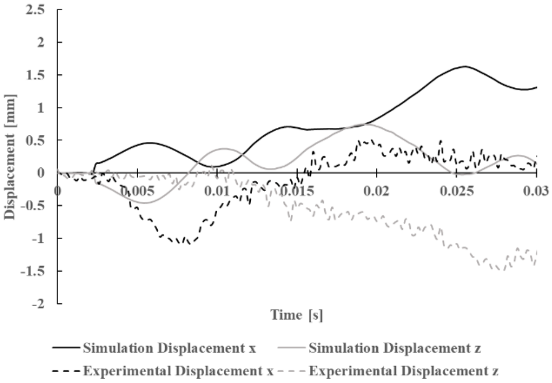

Point 6

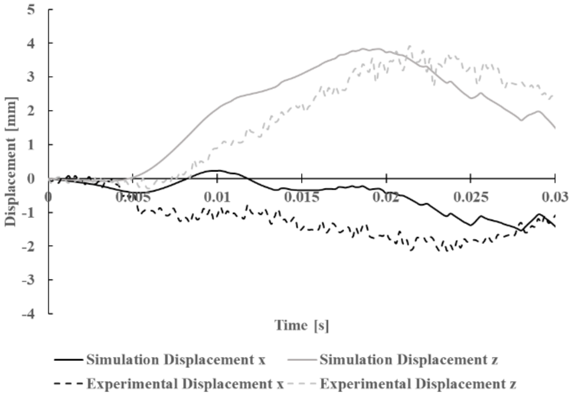

Point 7

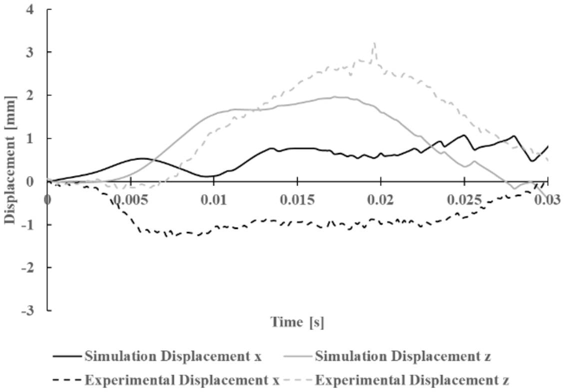

Point 8

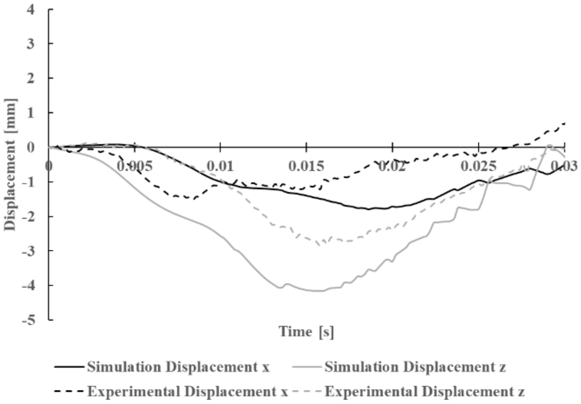

Point 9

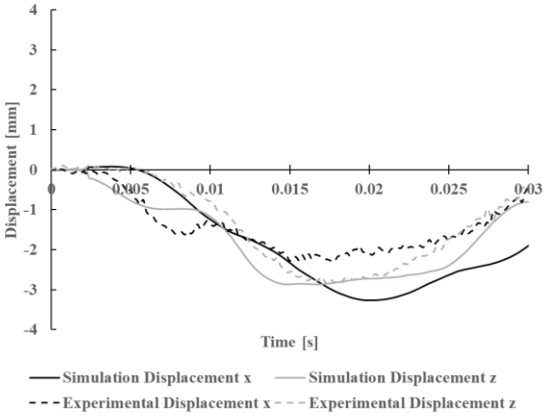

Point 10

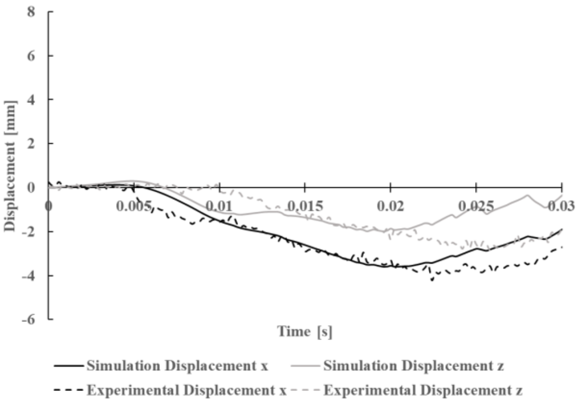

Point 11

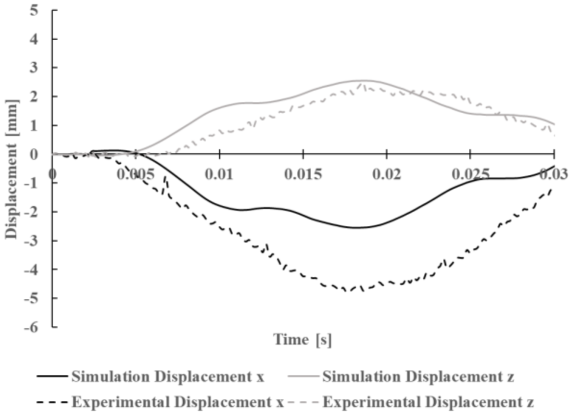

Point 12

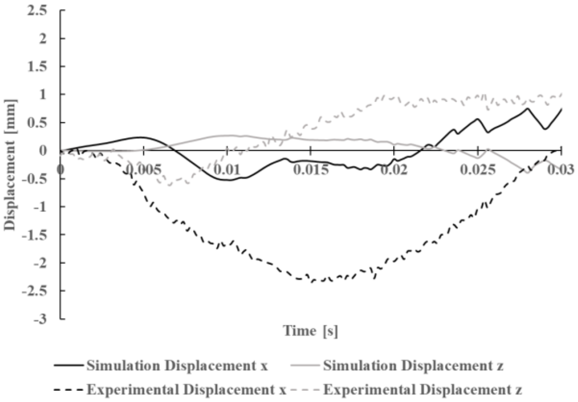

Point 13

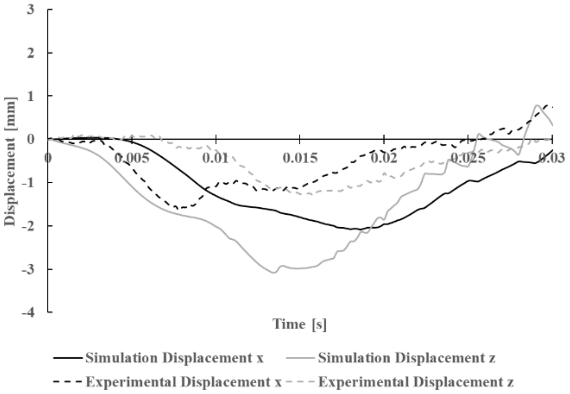

Point 14

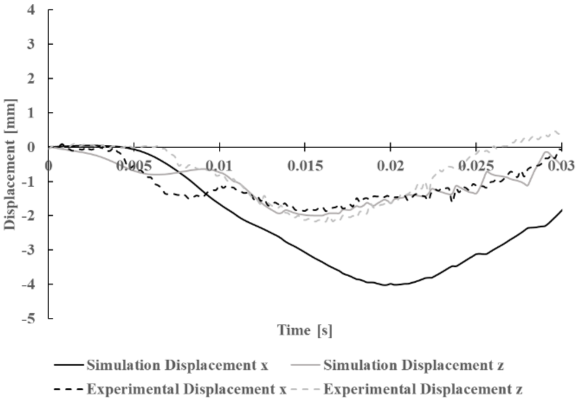

Point 15

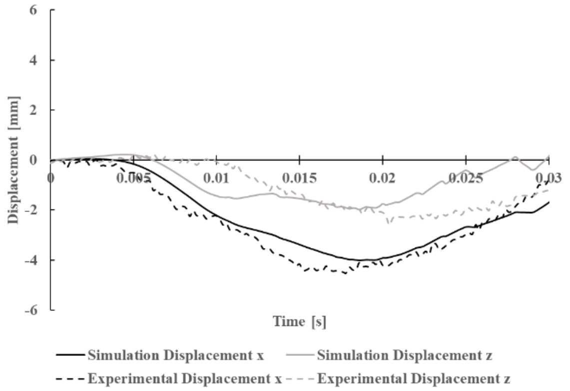

Point 16

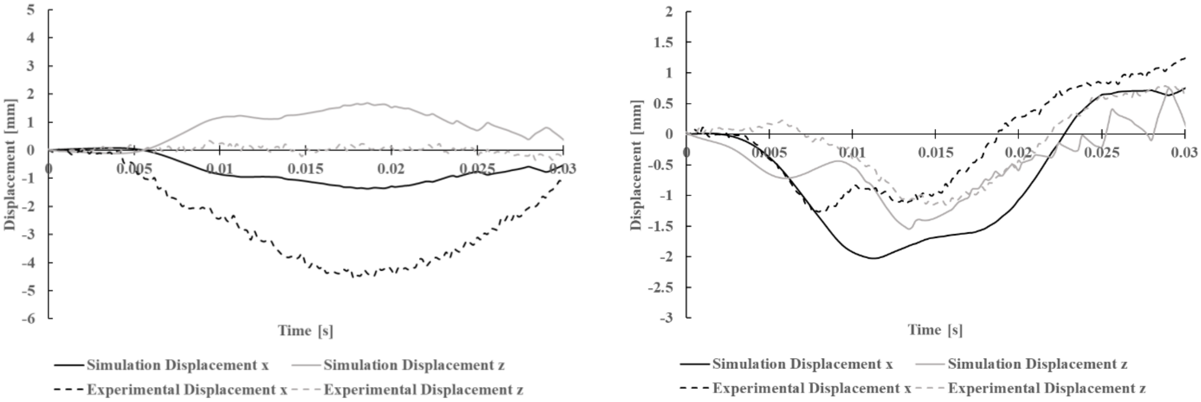

Point 17 Point 18

Figure A-3 Displacement time histories for Hit 1

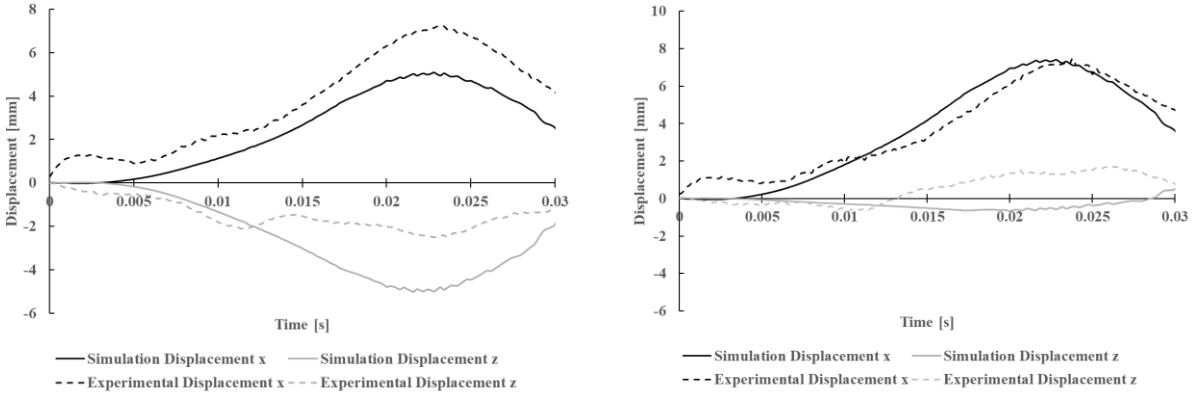

Point 1 Point 2

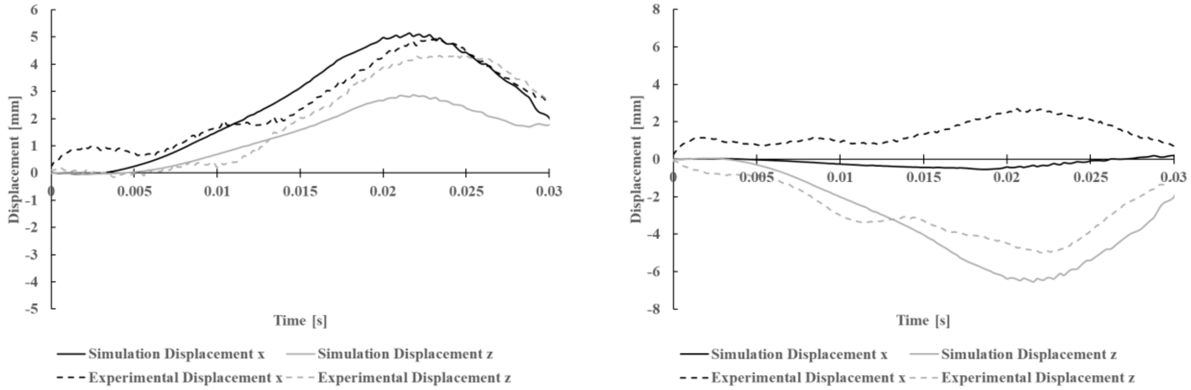

Point 3 Point 4

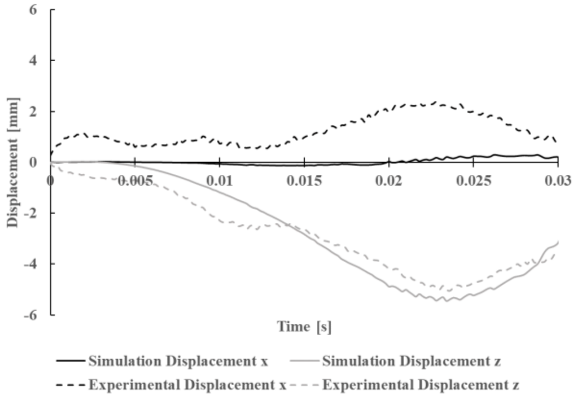

Point 5

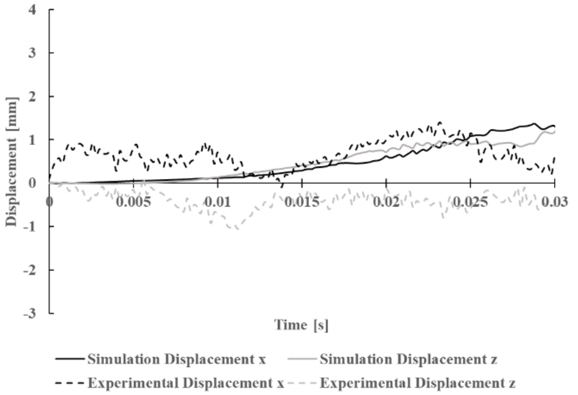

Point 6

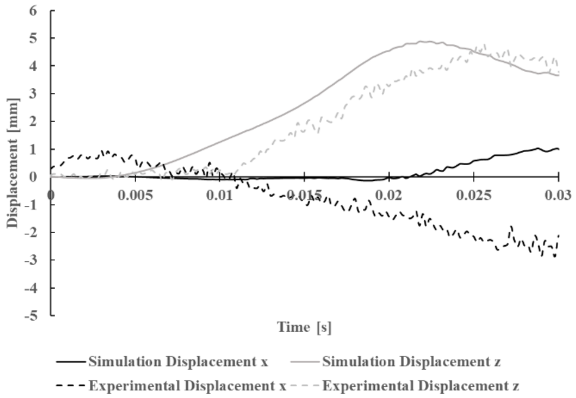

Point 7

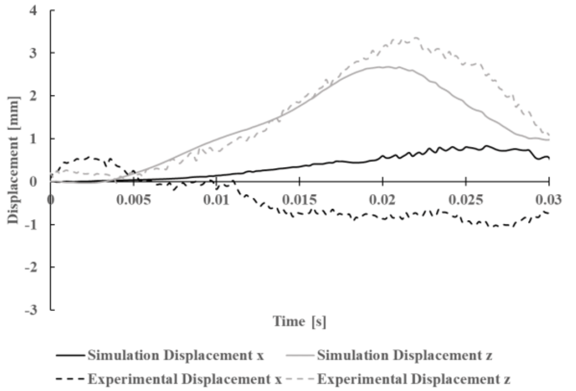

Point 8

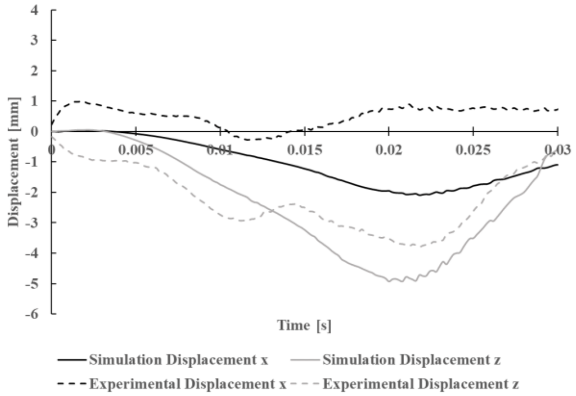

Point 9

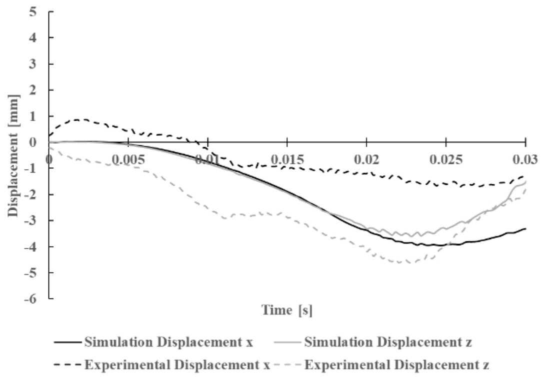

Point 10

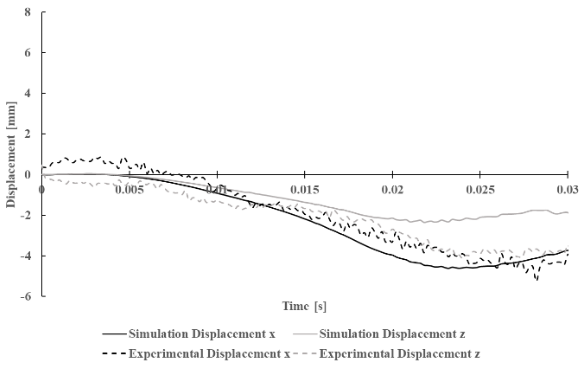

Point 11

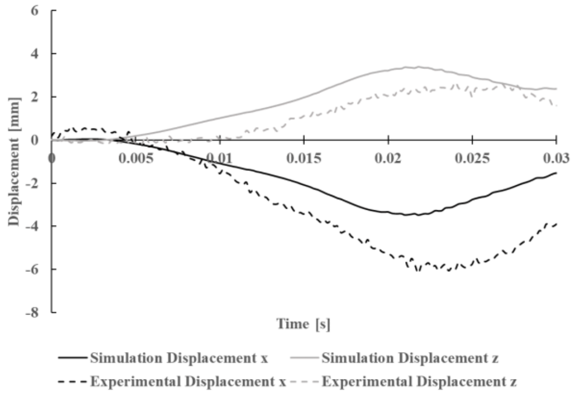

Point 12

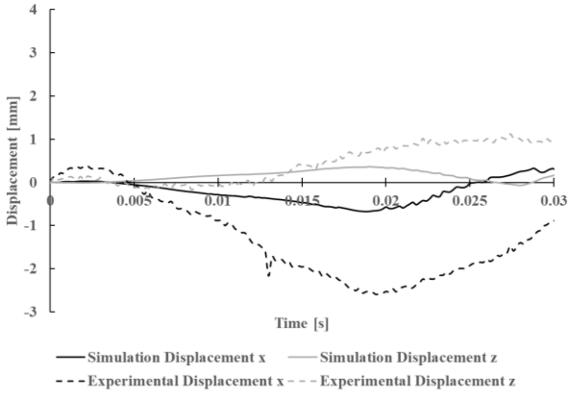

Point 13

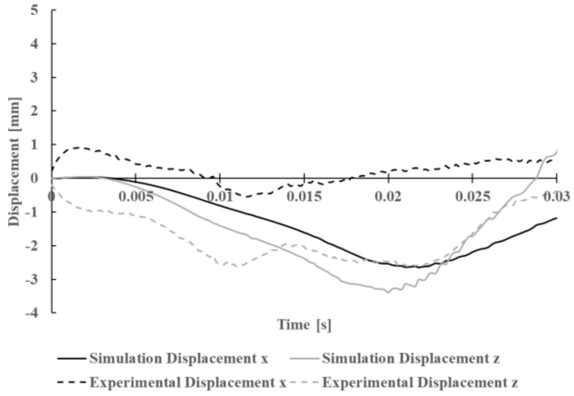

Point 14

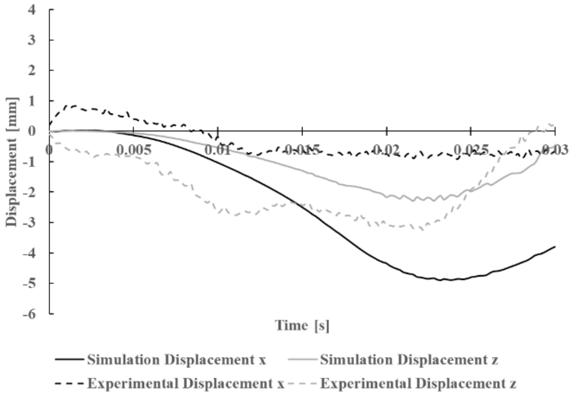

Point 15

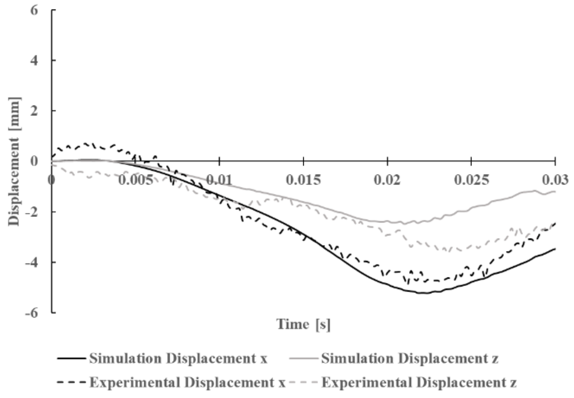

Point 16

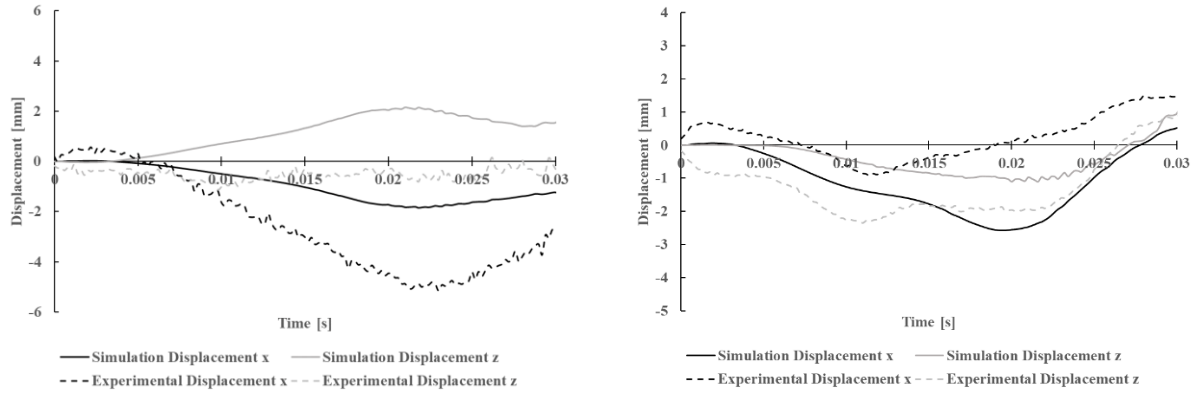

Point 17 Point 18

Figure A-4 Displacement time histories for Hit 2

Sensitivity Plots

Displacement Sensitivity Plots

The sensitivity plots for Hit 2 displacement test can be found in Figure A-5.

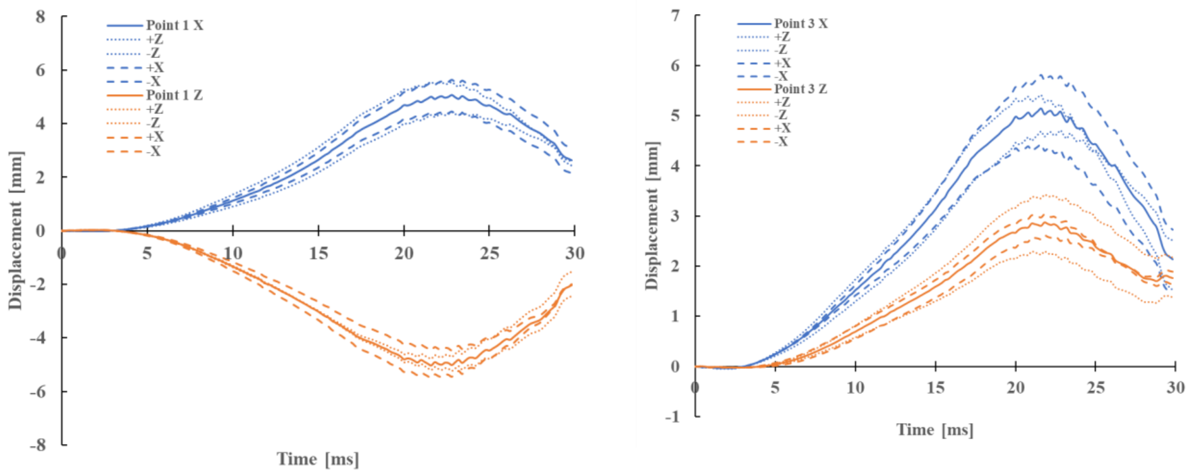

Point 1 Point 3

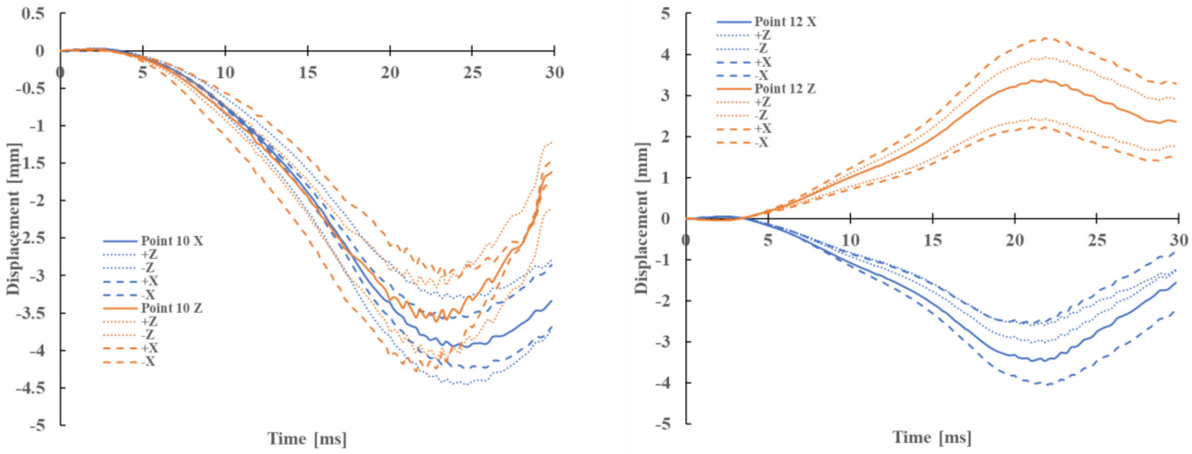

Point 10 Point 12

Figure A-5 Displacement Sensitivity for the Hit 2 impact

Pressure Sensitivity Plots

The sensitivities for the un-helmeted impacts can be seen in Figure A-6, the low speed helmeted impacts in Figure A-7, and the high speed helmeted impacts in Figure A-8.

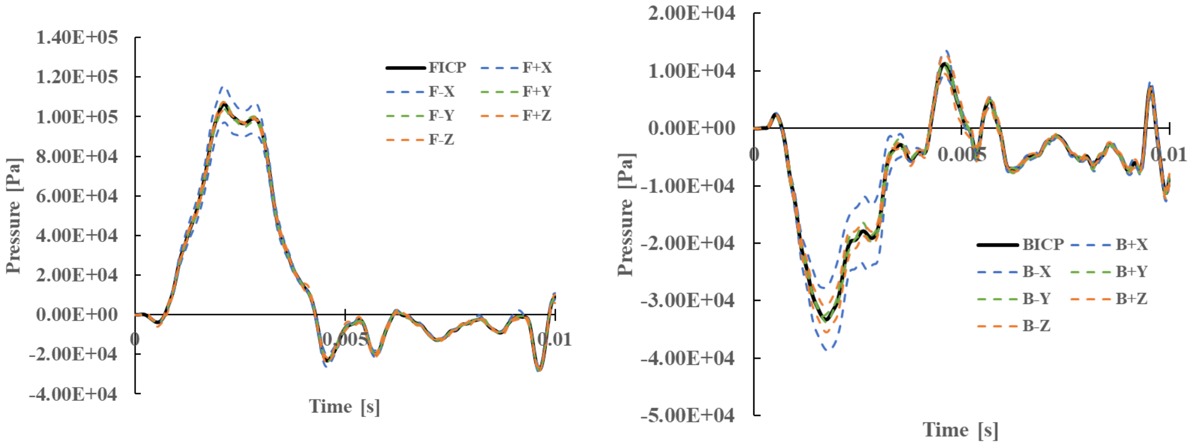

LowT0 FICP LowT0 BICP

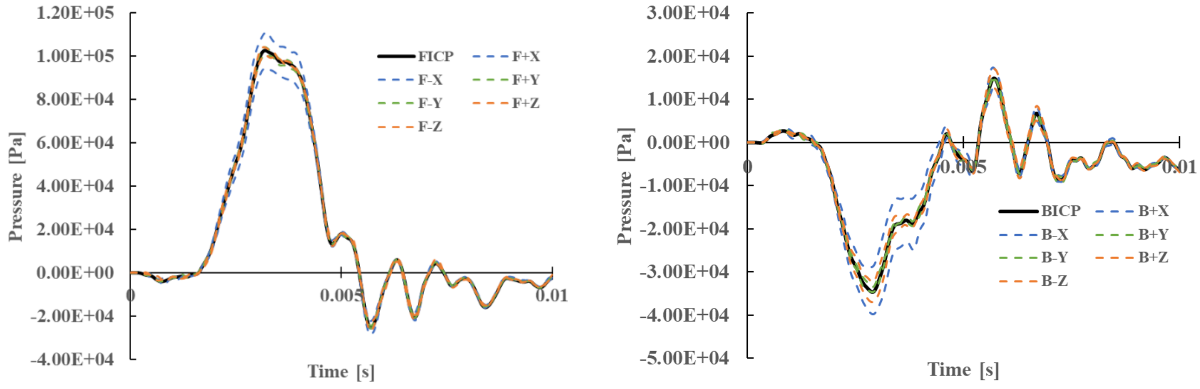

LowT1 FICP

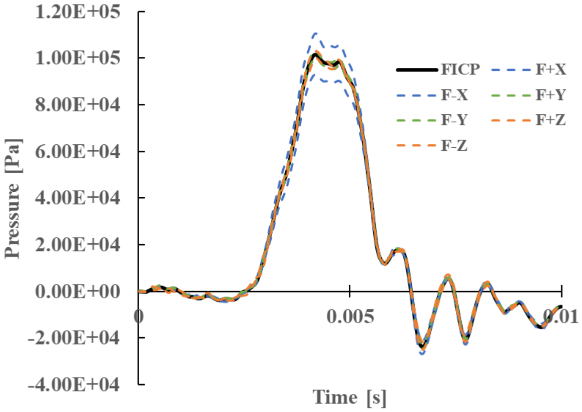

LowT1 BICP

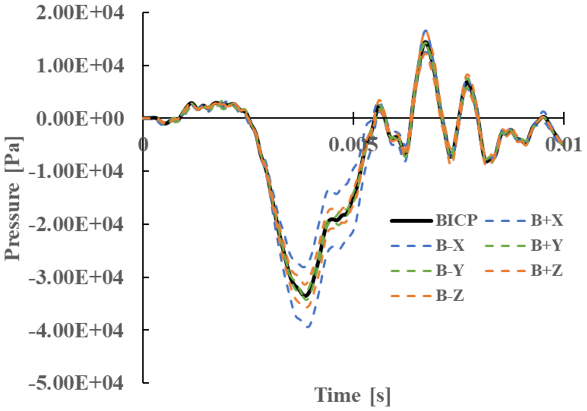

LowT2 FICP

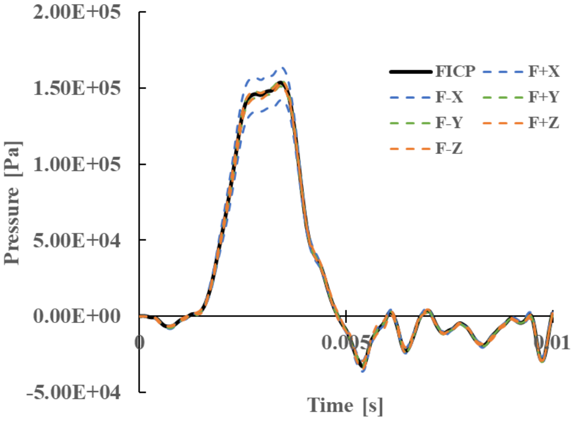

LowT2 BICP

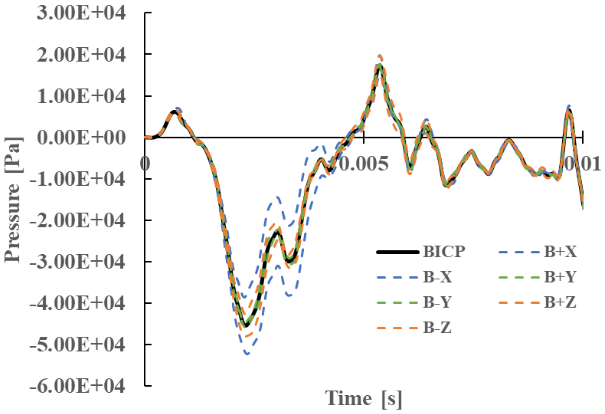

MedT1 FICP

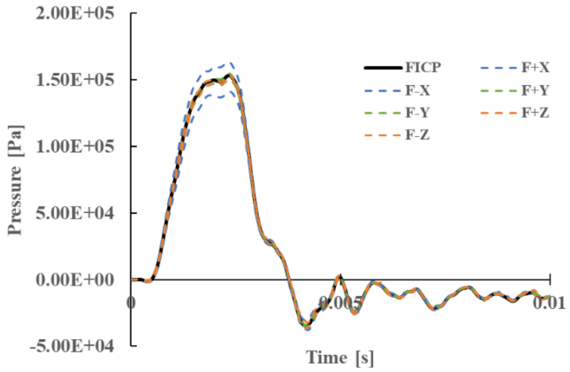

MedT1 BICP

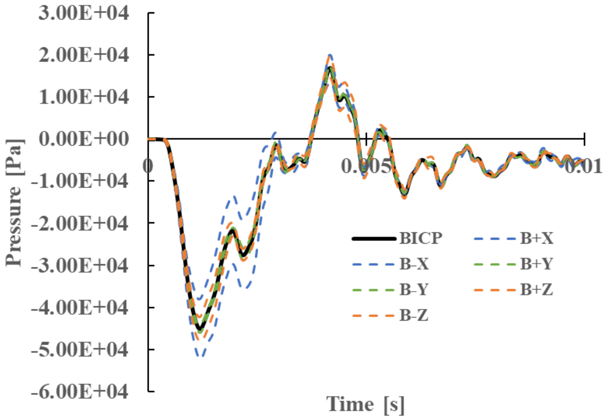

MedT2 FICP

MedT2 BICP

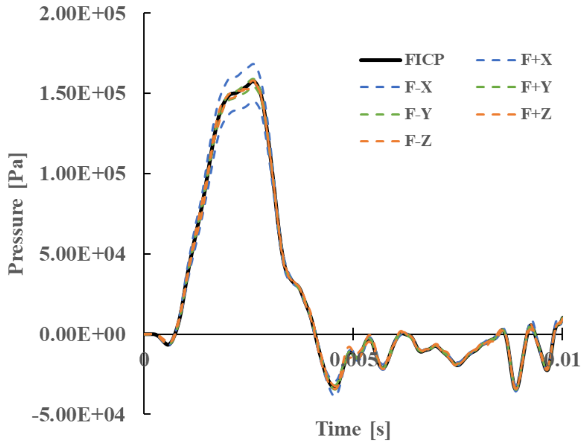

MedT3 FICP

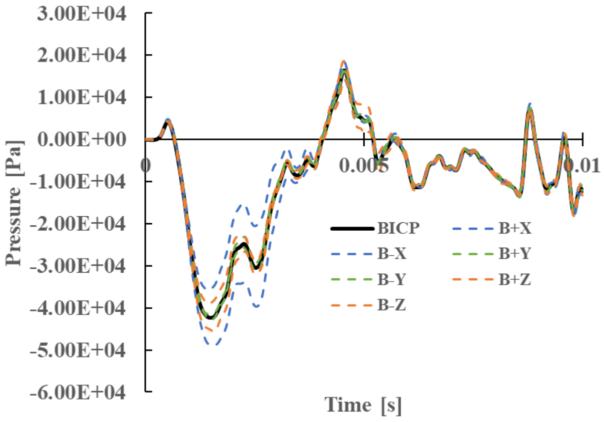

MedT3 BICP

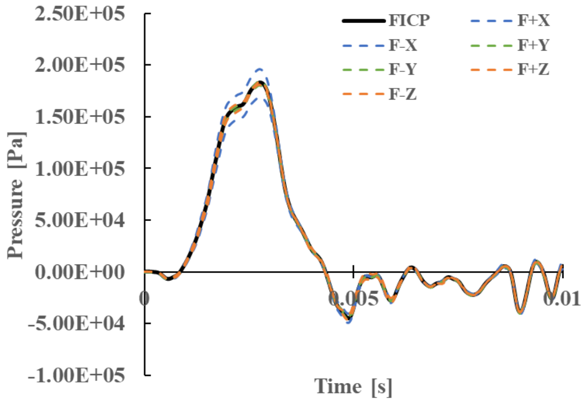

HighT0 FICP

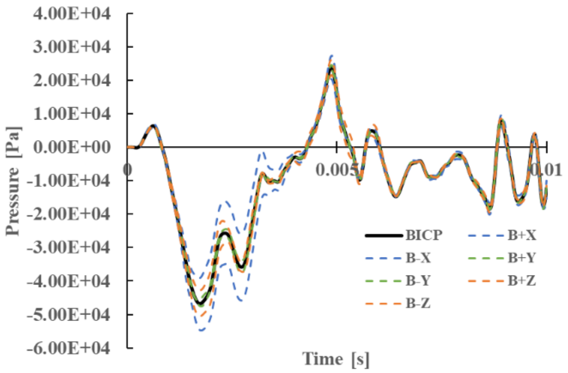

HighT0 BICP

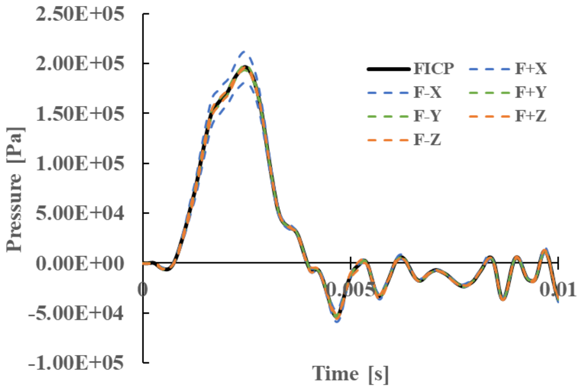

HighT1 FICP

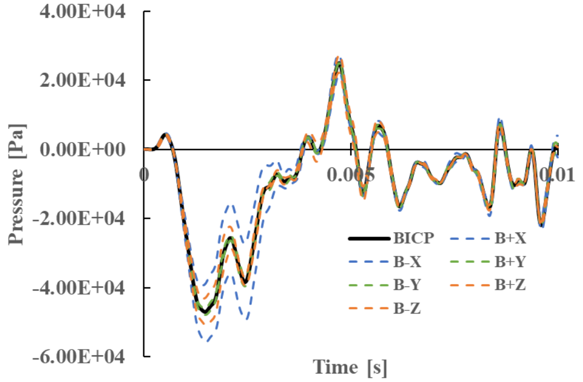

HighT1 BICP

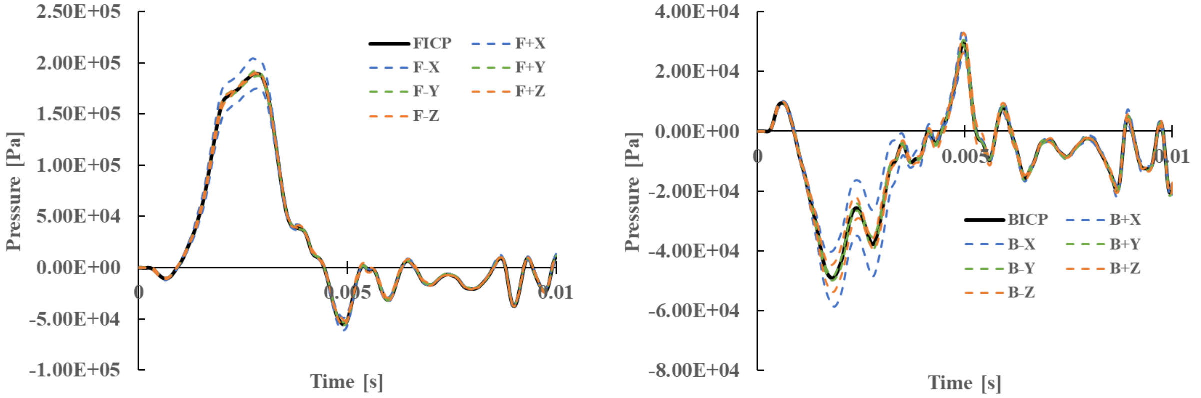

HighT3 FICP HighT3 BICP

Figure A-6 Sensitivity plots for unhelmeted impacts

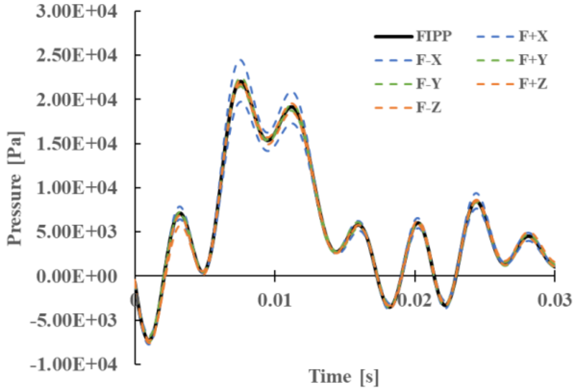

Front Front IPP

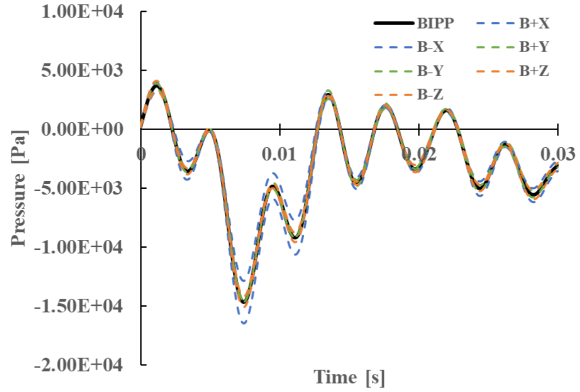

Front Rear IPP

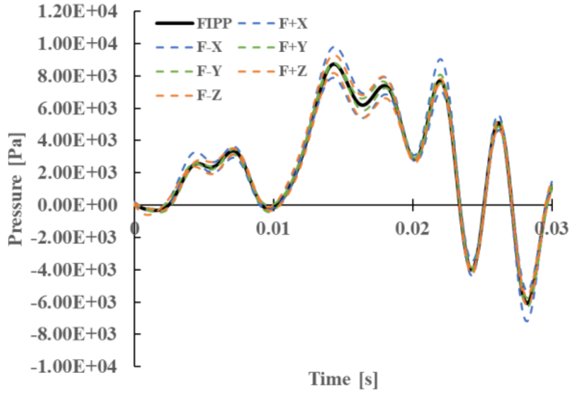

Crown Front IPP

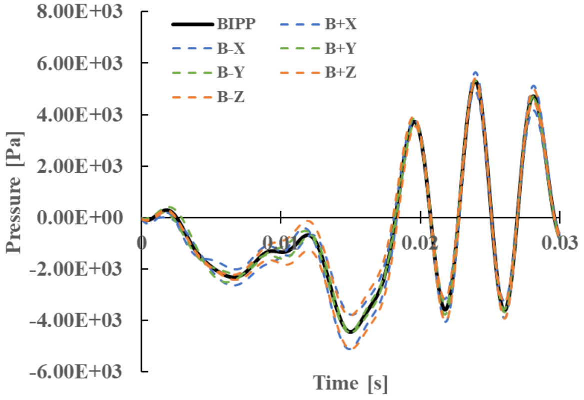

Crown Rear IPP

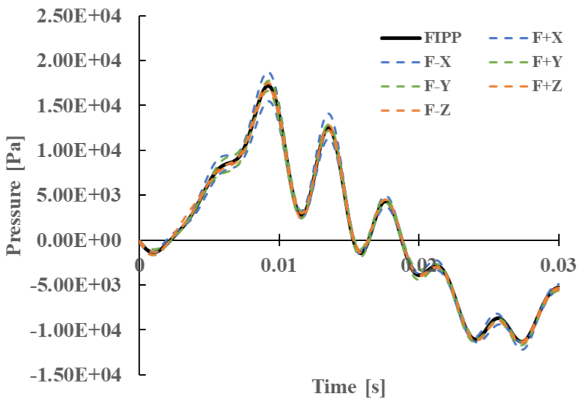

Front Boss Front IPP

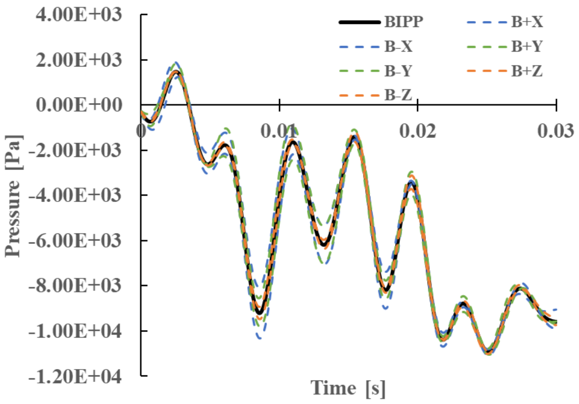

Front Boss Rear IPP

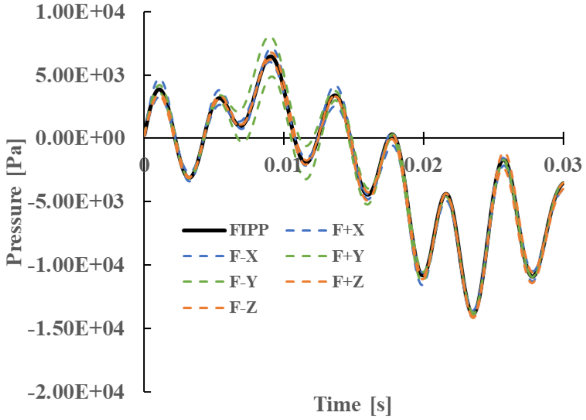

Side Front IPP

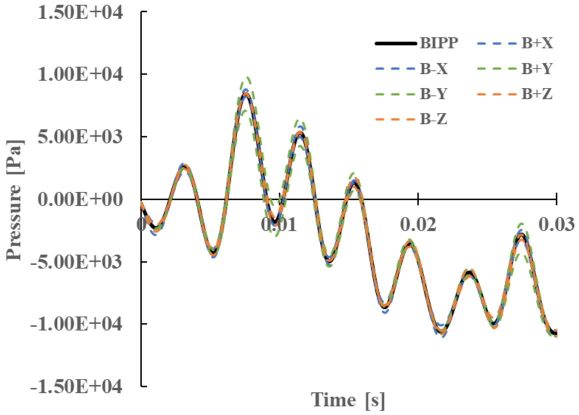

Side Rear IPP

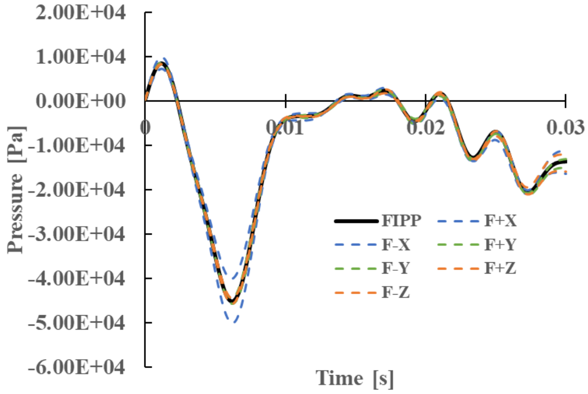

Rear Front IPP

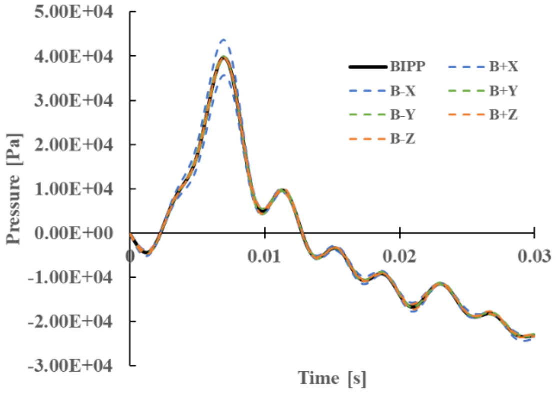

Rear Rear IPP

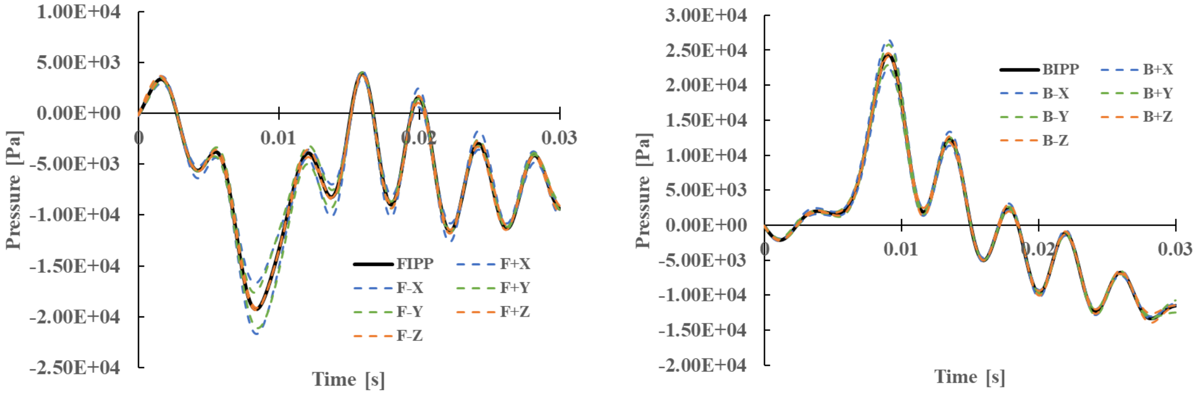

Rear Boss Front IPP

Rear Boss Rear IPP

Figure A-7 Sensitivity Plots for the low speed helmeted impacts

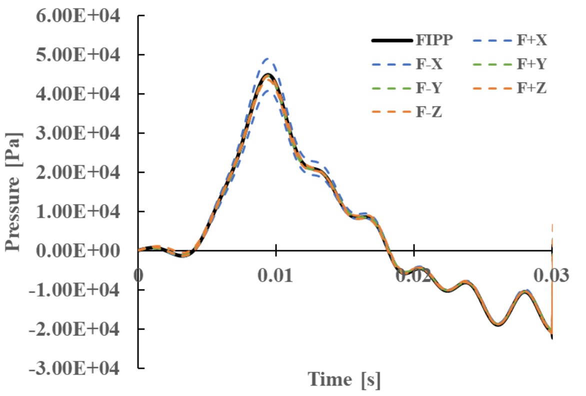

Front Front IPP

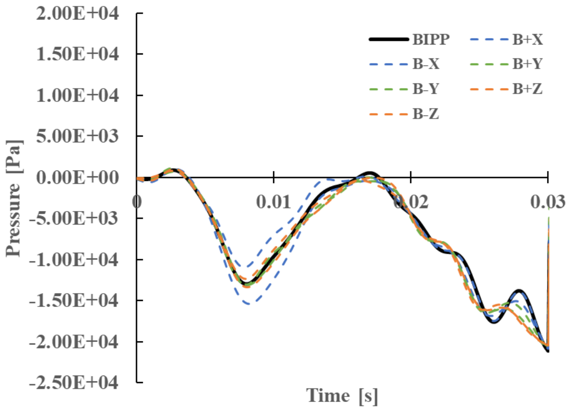

Front Rear IPP

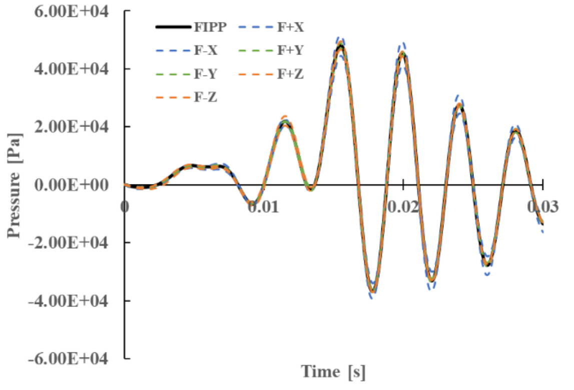

Crown Front IPP

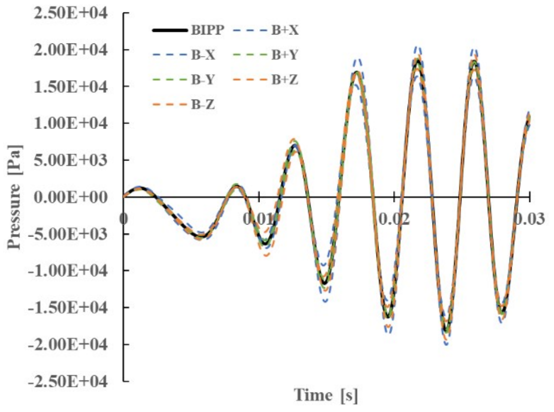

Crown Rear IPP

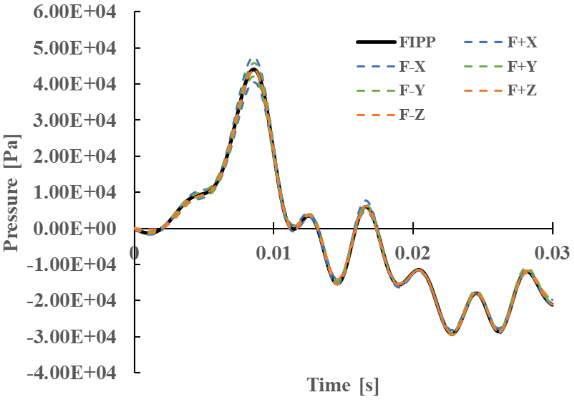

Front Boss Front IPP

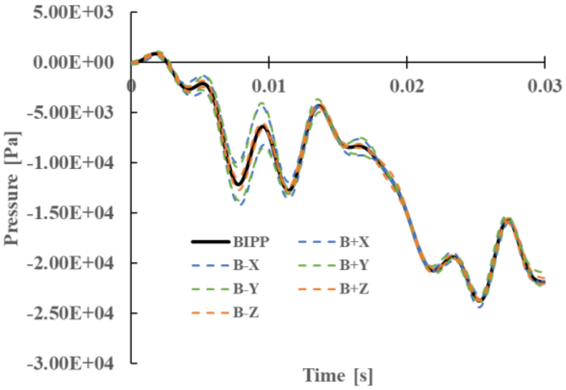

Front Boss Rear IPP

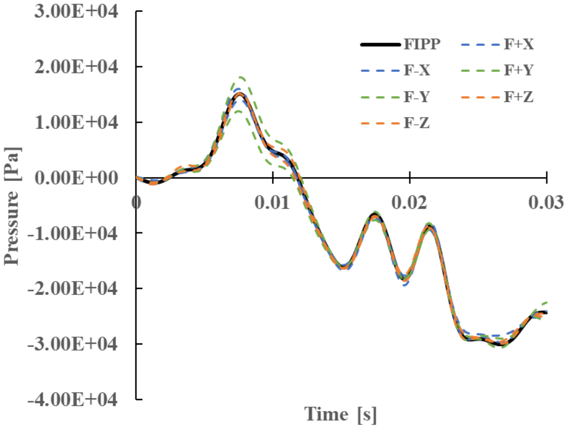

Side Front IPP

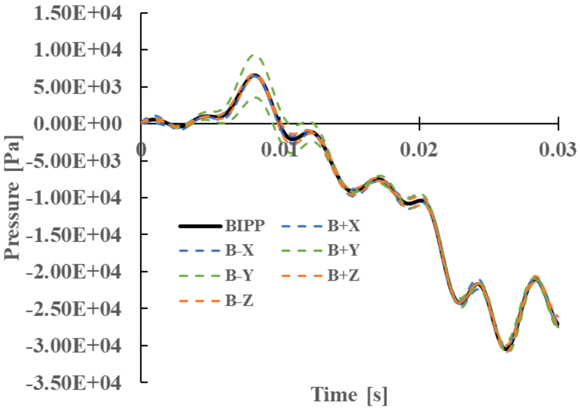

Side Rear IPP

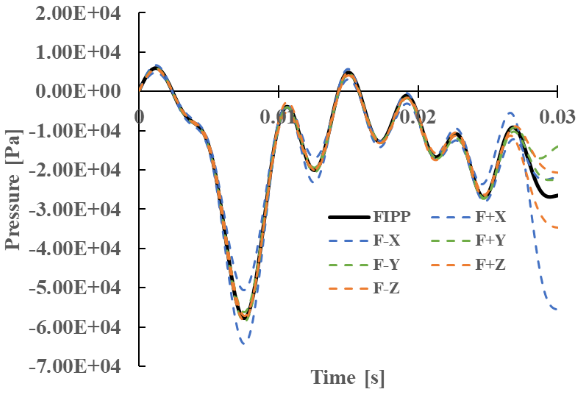

Rear Front IPP

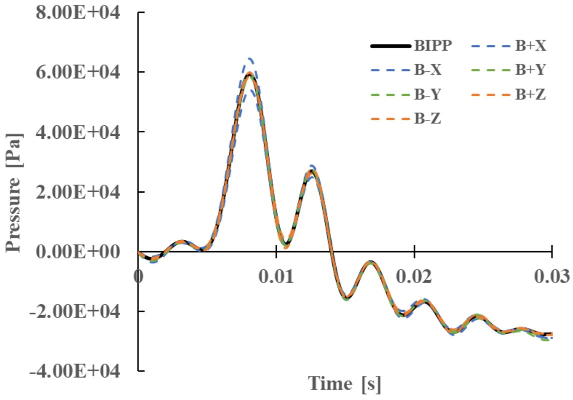

Rear Rear IPP

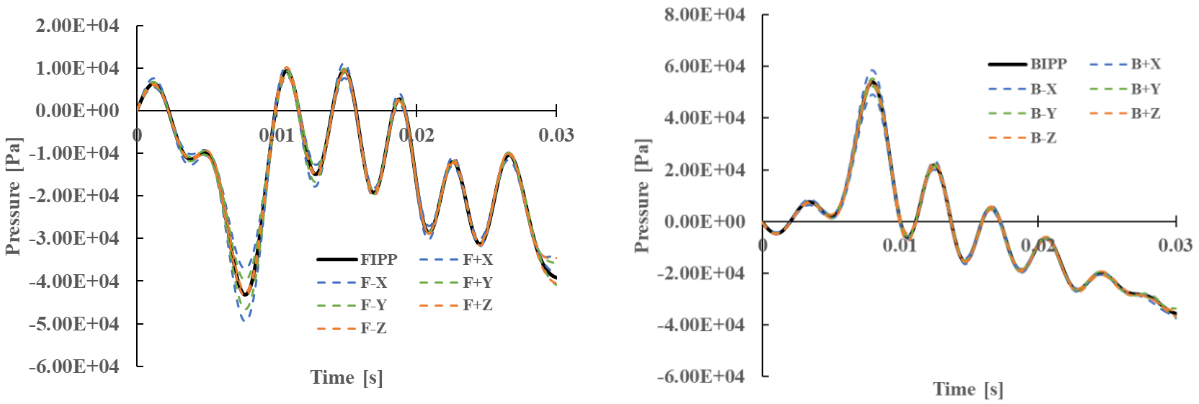

Rear Boss Front IPP

Rear Boss Rear IPP

Figure A-8 Sensitivity Plots for the high speed helmeted impacts